The Dissertation Committee for Shifeng Li
certifies that this is the approved version of the following dissertation:

Development of Microfluidic Systems for Biological Applications and Their Transport Issues

Committee:

Shaochen Chen, Supervisor

Ronald Panton

Dean Neikirk

Michael Bryant

Li Shi

Development of Microfluidic Systems for Biological Applications and Their Transport Issues

by

Shifeng Li, B.E.; M.E.

Dissertation

Presented to the Faculty of the Graduate School of
the University of Texas at Austin
in Partial Fulfillment
of the Requirements
for the Degree of

Doctor of Philosophy

The University of Texas at Austin

December, 2004

Dedication

To my parents and my family

Acknowledgement

First, I would like to express sincere gratitude to my supervisor, Professor Shaochen Chen for his guidance, encouragement, and caring financial support throughout my graduate study at UT-Austin. To me, he has been more than an advisor; his vision, inspiration, support and helps in many ways have made my research successful.

My appreciations also go to Dr. McDevitt in Chemistry and Biochemistry Department at UT-Austin for his kind helps, valuable discussions, and lab support. I am very thankful to Dr. Panton and Dr. Shi for their excellent courses and valuable comments on this work. I would like to thank Dr. Neikirk and Dr. Bryant for serving on my dissertation committee and providing advices on my research.

It has been a great pleasure to work with my fellow graduate students in Dr. Chen's group. My appreciation goes to Yi Lu, Senthil Theppakuttai, Dongbing Shao, David Fozard, Carlos Aguilar and Leo Han. In particular, I would like to thank David for his great help in preparing this dissertation. I would also like to thank Dr. Pierre Floriano, Dr. Nick Christodoulides, Mehnaaz Ali, Priya Dhashan and Mitra Mohanty in Prof. McDevitt's group for their helps and valuable inputs.

Financial support from US Navy through UT MD Anderson Cancer Research Center and funding from the Whitaker Foundation / UT Biomedical Engineering seed grant are greatly appreciated. I appreciate facility support from UT Microelectronics Research Center (MRC) and Professor M. Olson at Iowa State University.

Development of Microfluidic Systems for Biological Applications and Their Transport Issues

Publication No.____________________

Shifeng Li, Ph.D.
The University of Texas at Austin, 2004
Supervisor: Shaochen Chen

Microfluidic systems have been an exciting research area with a wide variety of promising biomedical applications. However, many challenging issues are still facing the research community with regard to mechanical as well as biological issues. The goal of this dissertation is to develop novel microfluidic systems targeting biomedical and life sciences applications with detailed investigation of thermal/fluid transport, materials and mechanics, and micromanufacturing processes.

For a valveless micropump used for fluid delivery, a theoretical model is derived to analyze a lead zirconate titanate (PZT) microactuator and a system level analytical analysis is carried out for the PZT-actuated micropump. The effects of several important parameters and nondimensional variable groups on the actuator performances are also investigated.

For rapid DNA analysis, a continuous-flow polymerase chain reaction (PCR) microchip with regional velocity control is developed. Finite element analysis is conducted to study the temperature uniformity of each reaction zone. A semi-analytical heat transfer model is developed to study heat transfer inside the PCR chip. Fluid velocity in the microchannel is measured using micro-particle image velocimetry (μ-PIV). The PCR chip is successfully amplified 90 base pair DNA sample.

To connect a microfluidic device with other devices, novel polydimethysiloxane (PDMS) based interconnects have been fabricated. Microfabrication processes for through-hole type and "┌" type PDMS interconnects of glass and plastic capillary tubing have been developed. Leakage pressure, leakage flow rate, and pull-out force are characterized for these PDMS interconnects bonded to a variety of substrates.

Two disposable analysis microchips in PDMS have been developed for protein/DNA detection. An established bead-based fluorescent assays for C-reactive protein (CRP) is used to characterize these chips. The detection limit of a single chamber chip is found to be as low as 0.1ng/ml. To increase detection capacity, a multiple-chamber PDMS chip has also been developed. Fluid flow through the multiple-chamber microchip is improved by a back pressure compensation method. This has significantly improved the performances of the microchip.

Table of Contents

List of Tables……………………………………………………………………..xii

List of Figures…………………………………………………………………....xiii

Chapter 1: Introduction………………………………………………………….....1

1.1. Microfluidics and Lab-on-a-chip………………………………………….....1

1.2. Motivation of Research and Overview of Dissertation……………….........3

1.3. References……………………………………………………………….…5

Chapter 2: Modeling and Simulation of Valveless PZT Micropump……………......8

2.1. Abstract…………………………………………………………………….8

2.2. Introduction………………………………………………………………..9

2.3. Modeling, Simulation and Optimization of PZT Microactuator…….……...11

2.3.1. Modeling of the Single Piezoelectric PZT Microactuator………...11

2.3.2. Comparison with Data from Experiments and Finite Element Simulation……………….…………………………………...18

2.3.3. Optimization of PZT Microactuator……………………………....24

2.3.3.1. PZT Disk Effects………………………………………….24

2.3.3.2. Bonding Material Effects…………………………………27

2.3.3.3. Passive Plate Effects…………………………………......30

2.4. System Level Modeling of Valveless PZT Micropump……………….........31

2.4.1. Flow Characteristics of Nozzle. …………………………………..31

2.4.2. Modeling of PZT Micropump…………………………………….35

2.5. Conclusions…………………………………………………………….....41

2.6. References……………………………………………………………...41
Chapter 3: Continuous-Flow Polymerase Chain Reaction Glass Microchip with Regional Velocity Control…………………………………………………………..45
3.1. Abstract……………………………………………………………...45
3.2. Introduction…………………………………………………………45
3.3. The Design of the PCR Microchip with Regional Velocity Control………..48
3.4. Modeling and Analysis of PCR Glass Microchip…………………….......52
3.4.1. Finite Element Analysis of Heat Transfer inside PCR Chip………52
3.4.2. Semi-Analytical Analysis of Heat Transfer inside PCR Chip…….55
3.4.3. Simulation of Fluid Flow inside PCR chip………………………..61
3.5. Fabrication and Instrumentation of PCR Glass Microchip………………….63
3.6. Experimental Results and Discussions……………………….……………..68
3.6.1. Temperature Measurement……………………...……………...68
3.6.2. Micro-PIV Velocity Measurement………………………………..70
3.6.3. PCR Amplification Experiment……………………………......75
3.7. Conclusions…………………………………………………………....77
3.8. References………………………………………………………………..78
Chapter 4: PDMS Interconnect for Microfluidics System Applications………………..80
4.1. Abstract…………………………………………………………………..80
4.2. Introduction……………………………………………………..……..80
4.3. Design and Fabrication Processes……………………………………..82
4.4. PDMS Interconnect Characterization ………………………………………91

4.4.1. Leakage Pressure Measurement…………………………….........91

4.4.2. Leakage Flow Rate Measurement…………………………………93

4.4.3. Pull-out Force Measurement………………………………………95

4.5. Conclusions……………………………………………………………....97

4.6. References…………………………………………………………...97

Chapter 5: Disposable PDMS/Silicon Hybrid Immunoassay Chip……………………...99

5.1. Abstract……………………………………………………………..99

5.2. Introduction…………………………………………………………..100

5.3. PDMS/Silicon Hybrid Chip Design and Fabrication……………………...101

5.3.1. Microchip Based Assays…………………………………………101

5.3.2. PDMS/Silicon Hybrid Chip Design ……………………………..102

5.3.3. PDMS/Silicon Hybrid Chip Microfabrication…………………...108

5.4. Experiments…………………………………………………………..114

5.4.1. Experiment Materials and Instrumentation………………………114

5.4.2. Optimization of CRP Assay Protocol……………………………117

5.4.3. Single Chamber PDMS Chip CRP Assay Characterization……..120

5.4.4. Four-Chamber PDMS Chip CRP Assay Characterization…..........123

5.5. Disposability of PDMS/ Silicon Hybrid Chips……………………………125

5.6. Conclusions…..126

5.7. References……………………………………………………………127

Chapter 6: Summary and Future Research……………………………………………..130

6.1. Current Research Summary…………………………………………130

6.2. Future Research…………………………………………………………...132
Appendix A Theoretical modeling of heat transfer inside a PCR device………………133
Appendix B Nomenclature…………………………………………………………..138
Bibliography…………………………………………………………………………144
Vita…………………………………………………………………………………..154

List of Tables

Table 2.1: Properties of the PZT, conductive epoxy and passive plate

Table 2.2: Dimensions for the piezoelectric microactuator simulation

Table 2.3: Summary of flow efficiency of different nozzle elements

Table 3.1: Material properties for thermal analysis

Table 4.1: Leakage pressure for different substrates and thin film materials (pressure unit: kPa)

List of Figures

Figure 2.1: (a) A schematic diagram of a single piezoelectric layer valveless micropump, and (b) a cross-section view of the micropump

Figure 2.2: Moment balance of the piezoelectric microactuator

Figure 2.3: Linear strain distribution and nonlinear stress distribution in the passive plate, the bonding layer, and the PZT disk

Figure 2.4: Comparison of the passive plate profiles from analytical calculation, experiment data, and FEM simulation. The working voltage $V_{0\text{-}p}$ = 50 V, the bonding layer thickness ratio $h_{b\text{-}p}$ = 0.04, the passive plate thickness h_p = 500 μm

Figure 2.5: Results from FEM and analytical calculation with (a) different bonding layer Young's modulus E_b', and (b) different passive plate Young's modulus E_p', normalized with the passive plate thickness h_p = 500 μm

Figure 2.6: The center passive plate deflections at different PZT disk thickness, (a) normalized with the passive plate thickness h_p = 500 μm, (b) normalized with the case that the bonding layer thickness ratio $h_{b\text{-}p}$ = 0

Figure 2.7: The passive plate center deflection at different radius ratios of PZT disk and the passive plate, (a) normalized with the passive plate thickness hp = 500μm, (b) normalized with the case that the bonding layer thickness ratio $h_{b\text{-}p}$ = 0

Figure 2.8: The passive plate center deflections at different E_bh^3/E_ph^3 ratios, normalized with the passive plate thickness h_p = 500 μm

Figure 2.9: The passive plate center deflections at different $E_{pzt}h^3/E_ph^3$ ratios under a constant electrical field, normalized with the passive plate thickness $h_p = 500$ μm

Figure 2.10: The passive plate central deflection at the different passive plate dimensions, normalized with the plate diameter a = 6mm

Figure 2.11: A cross-sectional view of a diffuser

Figure 2.12: A cross-sectional view of a nozzle

Figure 2.13: A control volume of a valveless micropump chamber

Figure 2.14: Results of (a) the inlet and outlet flow rates of the micropump, and (b) the working characteristics of the micropump

Figure 3.1: (a) Schematics of a 20-cycle, continuous-flow PCR microchip with regional velocity control (b) the concept of variable width channel (shown for one cycle)

Figure 3.2: Configuration of three copper heaters attached to glass surface

Figure 3.3: (a) Temperature distribution along the glass in the heater sequence of 90 ^{o}C – 75 ^{o}C – 60 ^{o}C, (b) heat flux at different heater spacing of 3 mm, 7 mm, and 12 mm

Figure 3.4: PCR device coordinates configuration

Figure 3.5: (a) Temperature files at the microchannel from the analytical equations and finite element analysis and 95 ^{o}C (b), 75 ^{o}C (c) and 60 ^{o}C (d) heaters heat flux from the analytical equations and finite element analysis.

Figure 3.6: Laminar flow within (a) a 7 ^{o} diffuser and (b) a 7 ^{o} nozzle at the target flow rate

Figure 3.7: (a) the finally assembled 20-cycle PCR glass microchip and (b) a close-up view of the microchannel on copper heaters

Figure 3.8: (a) The PCR experimental setup and (b) the configuration of the temperature control system

Figure 3.9: (a) IR picture for the temperature distribution on the PCR surface and (b) comparison of temperatures from the semi-analytical equation and experiment measurement

Figure 3.10: Micro-PIV experimental setup

Figure 3.11: PIV measurement positions within one thermal cycle

Figure 3.12: μ-PIV measurements taken at (a) position 1, (b) position 2, and (c) position 5 at the flow rates of 1 μl/min and 5 μl/min

Figure 3.13: μ-PIV measurements taken at (a) position 3, (b) position 8, and (c) position 13

Figure 3.14: A gel electrophoresis picture of the 20-cycle PCR product.

Figure 4.1: Schematic of PDMS interconnects: (a) through-hole type, (b) "┌" type, and (c) multiple-channel type.

Figure 4.2: (a) Optical picture for the non-circular hole punched with OD 0.84mm glass capillary. (b) Optical picture for circular hole punched with OD 0.84mm glass capillary.

Figure 4.3: The fabrication process of the "┌" type PDMS interconnect using a two-step curing method: (a) carbon thin film deposition, (b) first prepolymer injection, (c) metal pins positioning, (d) second prepolymer injection, extra prepolymer removal, (e) 1 hr curing, (f) metal pin removal and hole punching, (g) interconnect cutting

Figure 4.4: Through-hole type PDMS interconnect bonded to a glass substrate for glass capillary tube (a), for plastic capillary tubing (b), and "┌" type PDMS interconnect bonded to a PDMS substrate (c)

Figure 4.5: Schematic for (a) epoxy glued non-reusable PDMS interconnect and (b) reusable PDMS interconnect

Figure 4.6: Optical micrograph of the PDMS interconnects using a (a) glass capillary tube (O.D. 0.84 mm), and (b) plastic capillary tubing (O.D. 1.02 mm), indicating no epoxy blockage in the tube

Figure 4.7: The experimental setup for leakage pressure measurement

Figure 4.8: The experimental setup for leakage rate measurement

Figure 4.9: Results of leakage rate measurement for the PDMS interconnect bonded to a silicon substrate via O_2 RIE bonding and UV epoxy bonding

Figure 4.10: Results of pull-out force measurement for plastic tubing and glass capillary

Figure 5.1: Schematics of microchip based bead assays

Figure 5.2: Scan electron microscope picture of the silicon chip with beads (courtesy of Prof. McDevitt and Prof. Neikirk at UT Austin)

Figure 5.3: The "sandwich" format immunoassay

Figure 5.4: Schematics of the single chamber PDMS chip

Figure 5.5: Schematics of the four-chamber PDMS chip

Figure 5.5: The deformation of the PDMS chamber and channel at a chamber pressure of 34 KPa (5 psi) and a holding pressure of (a) 150 kPa, and (b) 350 kPa

Figure 5.6: The deformation of the PDMS chamber / channel at different holding pressures and chamber pressures

Figure 5.7: The fabrication process flow for the PDMS fluid network layer: (a) carbon thin film deposition on the silicon mold, (b) plastic ring position and the first PDMS prepolymer layer preparation, (c) pin positioning, (d) the second PDMS prepolymer layer injection, followed by removal of extra prepolymer, (e) 1 hr curing at 80°C, (f) PDMS layer removal and hole punching, (g) 50 µm thick PDMS layer spin coating, curing and bonding with the thick PDMS layer, (h) PDMS chamber opening, (i) 100 µm thick glass sheet bonding

Figure 5.8: An optical picture of a (a) single chamber PDMS chip (b) four-chamber PDMS chip

Figure 5.9: Coupling of antibody with glyoxal actuated agarose beads

Figure 5.0: A schematic diagram of fluorescent measurement setup

Figure 5.11: An optical picture of the experiment setup for PDMS chip characterization

Figure 5.12: The bubble problem of the PDMS chip: (a) bubble sticking to the beads, (b) bubble shielding the beads

Figure 5.13: CRP sandwich immunoassay: (a) antibody coating on the beads, (b) capture of the antigen, (c) injection of the detecting antibody, (d) signal generation

Figure 5.14: Optical micrograph of beads for CRP concentration of 1000 ng/mL

Figure 5.15: (a) Optical micrographs of anit-CRP coated beads at different CRP antigen concentrations (b) The measured intensity at the different CRP antigen concentrations

Figure 5.16: Dose response of four chambers at 1000ng/mL using the back pressure adjustment, (a) chamber #1, (b) chamber #2, (c) chamber #3, (d) chamber #4

Figure 5.17: Measured intensity of dose response for each chamber for the four-chamber chip at 1000ng/mL

Chapter 1: Introduction

1.1. Microfluidics and Lab-on-a-chip

Since the inception of micro-electro-mechanical systems (MEMS) in the early 1970s, microfluidic systems have been an exciting research area with a wide variety of important biomedical applications. The ultimate goal in the development of miniaturized bioanalysis systems is to create an integrated lab-on-a-chip or micro total analysis system (μ-TAS) constructed using well-established IC and microfabrication techniques [1]. The emerging field of microfluidics has prompted development of μ-TAS for processing, drug-delivery, manipulation, analysis, or construction of biological and chemical entities. More specifically, the application of microfluidics to diagnostics for DNA and protein [2, 3, 4], microarrays [5, 6, 7], tissue engineering [8, 9], surface modification [10], implantable BioMEMS [11], systems for drug delivery [12, 13] are of major interest. These systems offer several major advantages over conventional macroscopic analysis tools including: (1) smaller dimensions, (2) low manufacturing costs, (3) the ability to incorporate sensing, signal conditioning, and actuating functions in close proximity or on the same substrate, (4) superior functionality (resolution, sensitivity, etc.).

Microfluidic devices can be fabricated from three classes of materials categorized as: (1) materials like silicon and glass used for microelectronics and MEMS, (2) plastic and polymeric materials such as polydimethylsiloxane (PDMS) [14, 15 and 16], and (3) biological materials and entities such as proteins, cells, and tissues [17]. The first class of materials has traditionally been used in MEMS and ICs. These materials show superior mechanical properties making them suitable for a variety of transducing applications such as in accelerometers and gyroscopes. However, many biomedical devices require alternative soft or polymeric materials such as silicone rubber, polycarbonate, isobornyl acrylate, and polyamide. Polymers are inexpensive and can be used in disposable devices, relaxing stringent contamination issues. In addition, polymers reduce irritation and scarring of biological tissue and can exist as either a hard glassy material or a soft rubber, a variety not present in MEMS structures based on silicon or glass. The work encompassing the third class of materials is relatively unexplored, creating new and exciting possibilities for the development of microfluidic systems.

Basic fabrication methods currently used in MEMS are similar to those that have been employed by microchip manufacturers over the last four decades. These techniques are: (1) thin-film deposition, (2) lithography, (3) etching, and (4) substrate bonding. Thin films are deposited using various chemical or physical techniques and are used for masking, isolation, and structural purposes. After thin-film deposition, the lithography step is performed in order to transfer the designed pattern onto the substrate. This is basically identical to standard photography and printing techniques. The patterned substrate is etched using various chemicals in the liquid or gas phase. Finally, substrate bonding is used either to integrate multiple functionalities or for packaging purposes. These steps can be repeated numerous times depending on the complexity of the design and process. For polymeric materials, alternative fabrication techniques such as soft lithography and laser micromachining have been developed.

Despite heavy research efforts in microfluidics and on lab-on-a-chip systems, there are still technical barriers on packaging, materials, thermal/fluid transport [18, 19], interconnects, reliability, surface chemistry [20], and calibration issues. Other issues include: (a) biocompatibility of the substrate materials, (b) temperature control to prevent denaturation of biomolecules, (c) microfluidic interconnect for device-to-device and interfacing macro-components, (d) electrical connections while maintaining isolation between electronics and biofluids, and (e) disposability.

1.2. Motivation of Research and Overview of Dissertation

Motivated by technical challenges in developing advanced microfluidics and lab-on-a-chip systems, this research has focused on many mechanical issues including: thermal/fluid transport phenomena, materials, mechanics, and micromanufacturing of microfluidic and lab-on-chip systems. A theoretical model has been developed to analyze a PZT actuated valveless micropump, which is an important component in lab-on-a-chip systems for biological sample delivery. A continuous-flow, microscale polymerase chain reaction (PCR) device has also been developed for rapid DNA analysis. Moreover, microfluidic interconnecting was investigated. Finally, the design, fabrication and testing of disposable immunoassay devices for protein detection were also presented. It is expected this dissertation will provide the foundation for the realization of integrated lab-on-a-chip systems.

Chapter 2 presents an analytical model for a lead zirconate titanate (PZT) microactuator and a system level analytical model for a PZT-actuated valveless micropump. The analytical model for the PZT microactuator is derived from the assumption of a linear strain distribution along the PZT disk, the bonding layer, and the passive plate. The effects of several important parameters and nondimensional variable groups on the actuator performance were also investigated. This work has been published in *Sensors and Actuators, A* in 2003. Based on this PZT microactuator model, a system level analytical model for the PZT- actuated valveless micropump was also developed.

Chapter 3 demonstrates a continuous-flow polymerase chain reaction (PCR) microchip with regional velocity control. Finite element analysis and a semi-analytical heat transfer model were developed to investigate the thermal characteristics of the PCR microchip. Results from infrared temperature measurement are consistent with results from the semi-analytical model and finite element analysis. Micro-particle image velocimetry (μ-PIV) was used to visualize the flow fields inside the microchannel. These measurements confirm that there is no flow separation associated with the design of microchannel of variable width. The PCR microchip was tested using 90 base pair (bp) DNA fragment sample. Gel results show that PCR amplification was successful. Part of this work has been published in the *Journal of Manufacturing Processes in 2004* (part of work will be submitted to *Journal of Micromechanics and Microengineering*).

Chapter 4 presents novel polydimethylsiloxane (PDMS) based interconnects for microfluidic systems with a low dead volume. Through-hole type and “ ┌” type PDMS interconnects for glass and plastic capillary tubing have been designed, fabricated and tested. The leakage pressure, leakage flow rate, and pull-out force were characterized for PDMS interconnects bonded to a variety of substrates. This work was published in *IEEE Transactions on Advanced Packaging* in 2003.

Chapter 5 demonstrates two disposable analysis microchips fabricated out of PDMS and silicon for protein detection. An established bead-based fluorescent assay for C-reactive protein (CRP) was used to characterize these chips. The detection limit of the chip with the single chamber was found to be as low as 0.1ng/ml. To enhance detection capacity, I developed a four-chambered PDMS chip as well. Fluid flow through the multiple-chamber microchip was improved by employing the back pressure compensation method. This has significantly improved the performances of the microchip (This work will be submitted to *Biosensors and Bioelectronics*).

1.3. References

1. Manz A., Graber N. and Widmer H.M., 1990, *Sensors and Actuators B*, 1, 244-248
2. Ko J. S., et al, 2003, *Lab On a Chip*, 3, 106-113
3. Gau J., Lan E. H., Dunn R., Ho C. M., Woo J. C., *Biosensors and Bioelectronics*, 16, 745-755
4. Wang J., 2004, *Analytica Chimica Acta*, 506, 3-10
5. Yao G. and Tan W. H., 2004, *Analytical Biochemistry*, in press
6. Call D. R., Borucki M. K. and Loge F. J., 2003, *Journal of Microbiological Methods*, 53, 235-243

7. Wiese R., Belosludetsev Y., Powdrill T., Thompson P. and Hogan M., 2001, *Clinical Chemistry*, 47, 1451-1457
8. Tan W. and Desai T. A., 2003, *Biomedical Microdevices*, 5, 235-244
9. Leclerc E., Sakai T. and Fujii T., 2003, *Biomedical Microdevices*, 5, 109-114
10. Makamba H., Kim J. H., Lim K., Park N. and Hahn J. H., 2003, *Electrophoresis*, 24, 3607-3619.
11. Polla D. L., Erdman A. G., Robbins W. P., Markus D. T., Diaz J., Rizq R., Y., Nam H. Brickner T., 2000, *Annu. Rev. Biomed. Eng*, 551-576
12. Razzacki S. Z., Thwar P. K., Yang M., Ugaz V. M. and Burns M. A., 2004, *Advanced Drug Delivery Reviews*, 56, 185-198
13. Shawgo R. S., Grayson A. C. R., Li Y. W. and Cima M. J., 2002, *Current Opinion in Solid State and Materials Science,* 6, 329-334
14. Ng M. K., Gitlin I., Strook A. D. and Whitesides G. M., 2002, *Electrophoresis*, 23, 3461-3473
15. Sia S. K. and Whitesides G. M., *Electrophoresis*, 2003, 24, 3563-3576
16. Unger M. A., Chou H. P., Thorsen T., Scherer A. and Quake S. R., 2000, *Science*, 113-116.
17. Whitesides G.M., Ostuni E., Takayama S., Jiang X., and Ingber D., *Annu. Rev. Biomed. Eng*, 2001, 3, 335-73
18. Damean N., Regtien P. P. L. and Elwenspoek M., 2003, *Sensors and Actuators A*, 105, 137-149.
19. Erickson D., Li D.Q. and Krull U. J., 2003, *Analytical Biochemistry*, 317, 186-200

20. Xia Y. N. and Whitesides G. M., 1998, *Annu. Rev. Mater. Sci.* 28, 153-184

Chapter 2: Modeling and Simulation of a PZT Actuated Valveless Micropump

2.1. Abstract

Closed form analytical equations are important tools for predicting and optimizing the behavior of a piezoelectric microactuator for micropump applications. However, there is no reliable analytical solution to date to analyze the behaviors of a circular piezoelectric microactuator for a valveless micropump. In this chapter, a linear strain distribution is assumed across the thickness of the actuator given that the value of mechanical properties such as Young's Modulus and Poisson ratio of the Lead Zirconate Titanate (PZT) actuator and the passive plate are approximately same. The deformation of the passive plate from the analytical model agrees well with experimental data as well as the results from the finite element simulation. Based on this analytical model, the effects of several important parameters and nondimensional variable groups on the actuator performances have been investigated. These parameters and variables include the dimensions and mechanical properties of the PZT disk, the passive plate, and the bonding layer material. Finally, a system level analytical model for the PZT actuated valveless micropump is proposed based on this linear strain microactuator model. The output flow rate and back pressure are also investigated.

2.2. Introduction

Piezoelectric actuators have been widely used in mechanical actuation and sound generating or receiving devices [1]. To predict and optimize the behavior of the piezoelectric actuator, Crawley and Anderson developed an analytical model for a PZT actuator based on a uniform strain assumption [2]. This model is valid for a thin piezo-disk, where the disk thickness is less than half of the passive plate thickness. Kim and Jones used a linear strain assumption to predict an optimal rectangular actuator-to-plate thickness ratio at different Young's modulus ratios by optimizing the moment applied by a dual layer piezoelectric actuator [3]. The linear strain assumption provided a good approximation for the rectangular shape actuator when the bonding layer is thin. Ray et al. conducted three-dimensional analytical analysis for a rectangular, simply supported, multiple layer piezoelectric passive plate [4]. Chaudhry and Rogers presented a mathematical model for determining the optimum thickness ratio. They also predicted optimal length ratios for a rectangular actuator patch on a rectangular plate with fixed boundary [5]. For a circular bimorph, Yanagisawa and Nakagawa presented an analytical equation to optimize the radius of a resonant piezoelectric actuator with a limited number of thickness ratios [6]. Dobrucki and Pruchnicki studied an axisymmetric bimorph using finite element method. An analytical model was also presented for the deflection of the bimorph with the piezoelectric element covering the entire plate. A free boundary was assumed in their work [7]. Tzou [8] and Larson [9] conducted comprehensive investigation on composite piezoelectric shell models with various shapes and applications. A comprehensive review of analytical and numerical approaches to model and optimize PZT actuator behavior was recently given by Chee et al. [1].

In the micro-electro-mechanical systems (MEMS) area, a piezoelectric actuator has also been widely used in micropumps and other actuation devices [10, 11, 14]. Yoon and Washington proposed moment balance method to analyze beam type piezoelectric actuator [13]. DeVoe et al. derived an analytical model for a beam type of piezoelectric microactuators that included the bonding layer effects [11, 12]. Cao et al. presented a simplified analytical model for a thin passive plate type of piezoelectric microactuators in valveless micropump applications. In order to obtain a closed form analytical solution, major assumptions such as the entire passive plate to be covered by a PZT layer and no transverse shear have to be made [15]. Such assumptions may result in a significant discrepancy between the analytical results and experimental results [15, 16]. For this reason, finite element method has been the main approach to analyze and optimize the piezoelectric microactuator consisting of a PZT disk, bonding material, and a passive plate [7, 14].

In this chapter, a new analytical model is derived based on linear strain assumptions to analyze the passive plate deflection in a piezoelectric microactuator. Results from this model are compared with previously published experimental data and finite element simulation. Furthermore, the analytical model is used to investigate the effects of several critical design parameters and nondimensional variable groups on the performances of the actuator. Based on this microactuator analytical model, a system level model for the valveless micropump is proposed. The flow rate and back pressure of the valveless micropump is also studied.

2.3. Modeling, Simulation and Optimization of a PZT Microactuator

2.3.1. Modeling of a Single Piezoelectric Microactuator

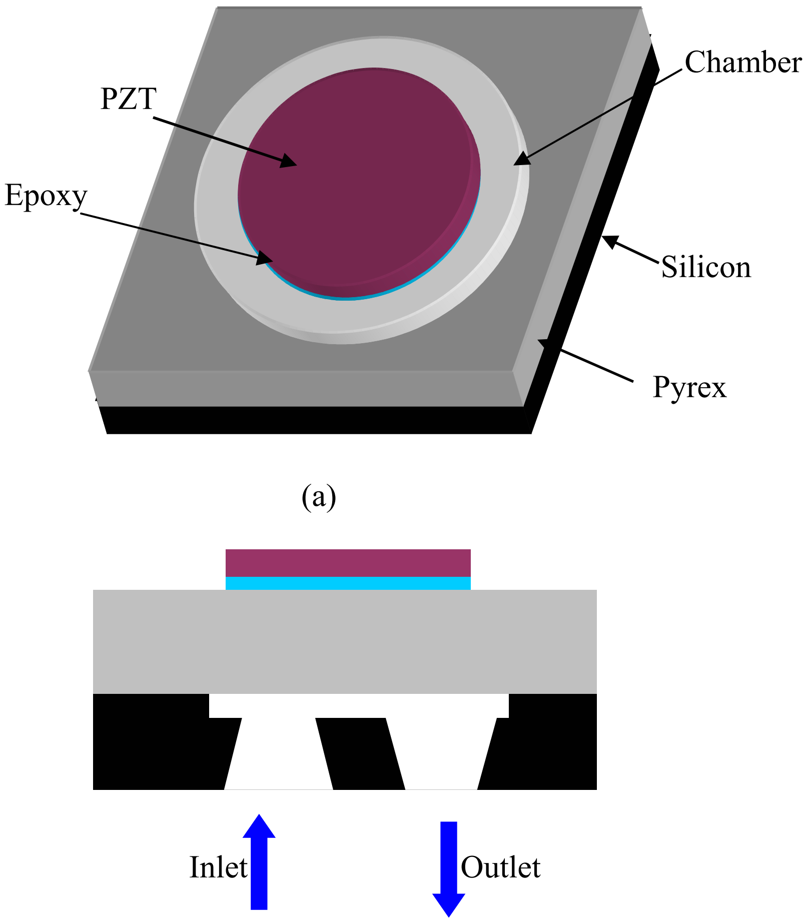

(a)

(b)

Figure 2.1: (a) A schematic diagram of a single piezoelectric layer valveless micropump, and (b) a cross-section view of the micropump

A typical PZT-actuated valveless micropump is shown in Figures 2.1a and 2.1b [10, 17, 18, 19]. The PZT disk is bonded to the passive plate using a thin layer of conducting epoxy. When an electric field is applied to the PZT disk, the strain produced in the PZT disk causes the passive plate to expand or contract, resulting in actuation for the micropump. Therefore, the liquid can be pumped in or out of the chamber. A net flow is formed from the inlet to the outlet due to the function of the diffuser or nozzle depending on the flow direction. For convenience of analysis, we divided this structure into two parts: one is the three-layer structure including the PZT disk, the bonding material, and the passive plate beneath the bonding layer, the other is the rest of the passive plate part. The moment balance for each part is shown in Figure 2.2.

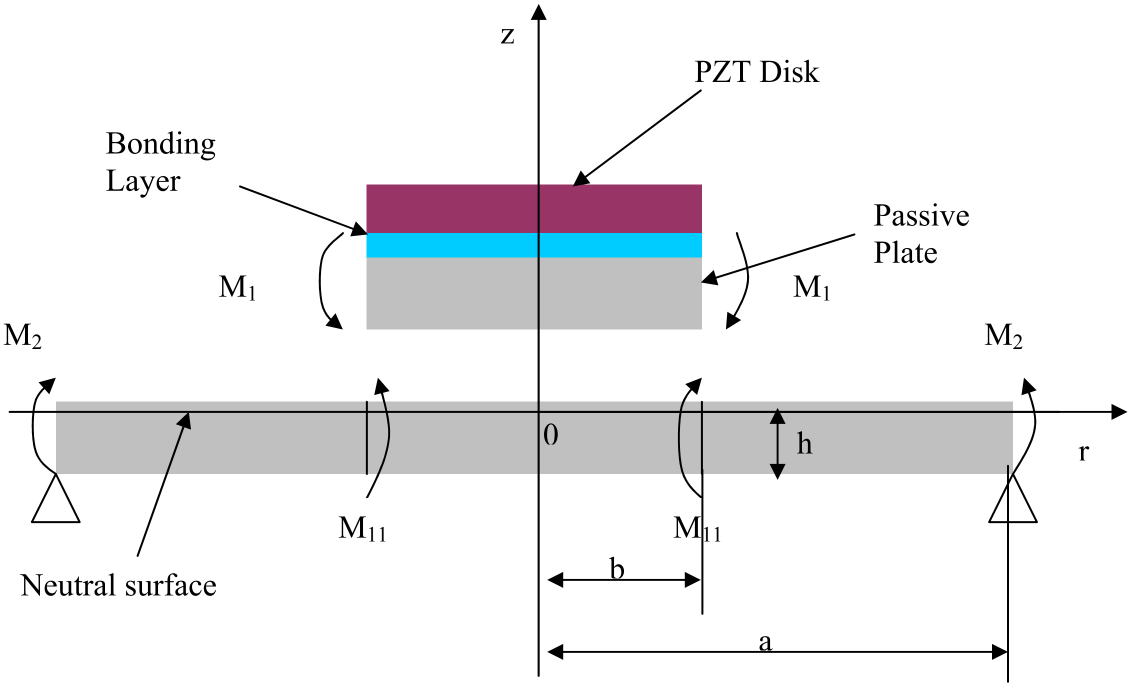

Figure 2.2: Moment balance of the piezoelectric microactuator.

As shown in Fig. 2.3, there exists a neutral surface that does not have either transverse strain or radial strain. The potential energy in the neutral surface reaches a minimum value [7]. The location of this neutral surface is found to be

$$h=\frac{1}{2}\frac{\dfrac{E_p h_p{}^2}{1-\gamma_p{}^2}+\dfrac{E_b[(h_b+h_p)^2-h_p{}^2)]}{1-\gamma_b{}^2}+\dfrac{E_{pzt}[(h_b+h_p+h_{pzt})^2-(h_p+h_b)^2]}{1-\gamma_{pzt}{}^2}}{\dfrac{E_p h_p}{1-\gamma_p{}^2}+\dfrac{E_b h_b}{1-\gamma_b{}^2}+\dfrac{E_{pzt}h_{pzt}}{1-\gamma_{pzt}{}^2}} \tag{2.1}$$

where *E* represents Young' Modulus, γ is Poisson ratio, and *h* is the thickness. The subscript *p*, *b*, and *pzt* represent the passive plate, the bonding layer, and the PZT disk respectively.

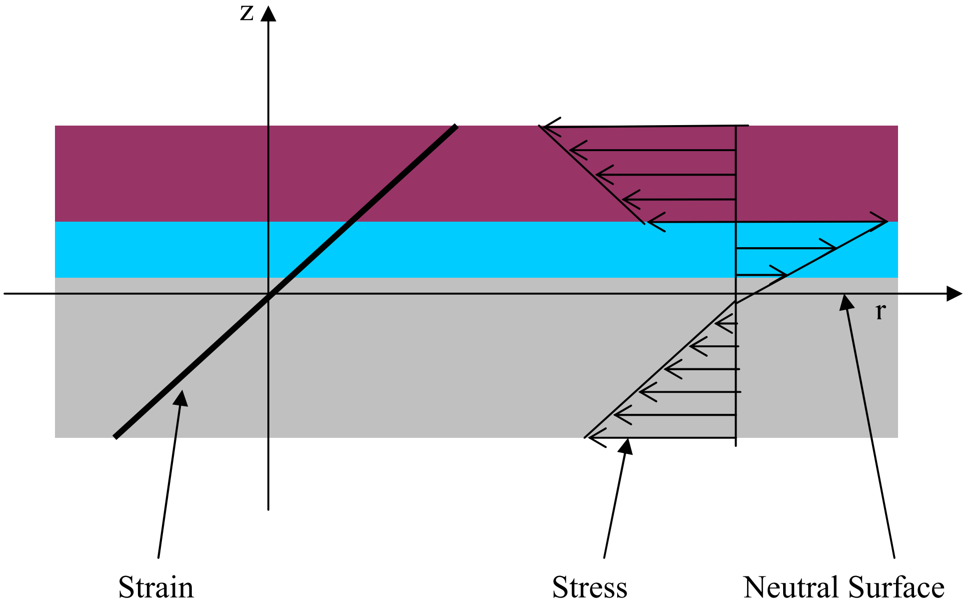

Figure 2.3: Linear strain distribution and nonlinear stress distribution in the passive plate, the bonding layer, and the PZT disk

For most valveless micropumps developed, a Pyrex 7740 glass wafer is used to bond with the silicon substrate to seal the pumping chamber [10, 17, 18, 19]. The Young's modulus and Poisson ratio of the Pyrex 7740 glass material are approximate to those of the PZT material. Given that the three-layer structure is thin compared to its radius of curvature, a linear strain distribution across the thickness direction can be assumed in this structure. Therefore, the strain at the interface will be continuous and the radius of curvature for each layer shares the same center.

For the bonding material, the stress follows

$$\sigma_b = \frac{E_b}{1-\gamma_b}\varepsilon_b \tag{2.2}$$

where ε_b is the strain of the bonding material. Since the strain distribution is assumed to be linear, we have

$$\varepsilon(z) = \varepsilon_p = \varepsilon_b = \varepsilon_{pzt} = z\kappa \tag{2.3}$$

$$\sigma_p = \frac{\sigma_i}{(h_p - h)} z \tag{2.4}$$

Where z is the displacement from the neutral surface, σ_i is the stress at the interface between the bonding layer and the passive plate, and h is the distance between the neutral surface and the bottom surface of the passive plate. The passive plate, the bonding layer, and the PZT disk have different deflection from the neutral surface. From Equation 2.4, the strain slope k is found as

$$\kappa = \frac{1-\gamma_p}{E_p}\frac{\sigma_i}{(h_p - h)} \tag{2.5}$$

The stress distribution in the bonding layer follows

$$\sigma_b = \frac{E_b}{1-\gamma_b}\kappa z = \frac{1-\gamma_p}{1-\gamma_b}\frac{E_b}{E_p}\frac{\sigma_i}{(h_p-h)}z \tag{2.6}$$

For an actuator with a single piezoelectric layer, the PZT disk has five independent elastic material constants and three independent piezoelectric constants. However, because the strains in the Z direction can not generate traction forces at the interface surfaces and the micropump working frequency is much lower than the resonant frequency of the PZT actuator that is typically over $1MHz$, the PZT material is assumed to be elastically isotropic. From the linear piezoelectric constitutive equations, the stress and strain relationship for the PZT-actuator can be expressed as

$$\sigma_{pzt} = \frac{E_{pzt}}{1-\gamma_{pzt}}\left(\kappa z - \frac{V}{h_{pzt}}d_{31}\right) = \frac{\sigma_i(1-\gamma_p)E_{pzt_i}}{(1-\gamma_{pzt})E_p(h_p-h)}z - \frac{E_{pzt}}{(1-\gamma_{pzt})}\frac{V}{h_{pzt}}d_{31} \tag{2.7}$$

where d_{31} is electrical-mechanical coupling coefficient in the z direction and V is the AC working voltage of 3000 Hz.

Balancing the moment in the three-layer structure gives

$$\int_{-h}^{h_p-h}\sigma_p z dz + \int_{h_p-h}^{h_p-h+h_b}\sigma_b z dz + \int_{h_p-h+h_b}^{h_p-h+h_b+h_{pzt}}\sigma_{pzt} z dz = 0 \tag{2.8}$$

Let $h'=h_p-h$, we have

$$\sigma_i = \frac{3\eta U d_{31}(2h'+2h_b+h_{pzt})h'}{2(h'^3+h^3+\alpha((h'+h_b)^3-h'^3)+\beta((h'+h_b+h_{pzt})^3-(h'+h_b)^3))} \tag{2.9}$$

Where $\alpha = \frac{1-\gamma_p}{1-\gamma_b}\frac{E_b}{E_p}$, $\beta = \frac{1-\gamma_p}{1-\gamma_{pzt}}\frac{E_{pzt}}{E_p}$, and $\eta = \frac{E_{pzt}}{1-\gamma_{pzt}}$

The moment M_1 is given by

$$M_1 = \int_{-h}^{h'} \sigma_p z dz = \frac{\eta U d_{31}(2h'+2h_b+h_{pzt})(h'^3+h^3)}{2(h'^3(1-\alpha)+h^3+(\alpha-\beta)(h'+h_b)^3+\beta(h'+h_b+h_{pzt})^3)} \qquad (2.10)$$

Following Christensen's analytical equations for mechanical properties of multiple layer structures [20], we derived the Young's Modulus and the Poisson ratio for the three-layer structure. For the PZT and the bonding layer

$$E' = C_1 E_{pzt} + C_2 E_b + \frac{C_1 C_2 E_{pzt} E_b (\gamma_{pzt} - \gamma_b)^2}{(C_1 E_{pzt}(1-\gamma_b{}^2) + C_2 E_b (1-\gamma_{pzt}{}^2))} \qquad (2.11)$$

$$\gamma' = \frac{C_1 \gamma_{pzt} E_{pzt} (1-\gamma_b{}^2) + C_2 \gamma_b E_b (1-\gamma_{pzt}{}^2)}{(C_1 E_{pzt}(1-\gamma_b{}^2) + C_2 E_b (1-\gamma_{pzt}{}^2))} \qquad (2.12)$$

where $C_1 = {}^{h_{pzt}}\!/_{h''}$, and $C_2 = {}^{h_b}\!/_{h''}$, $h''=h_{pzt}+h_b$,

Now let $h_{all} = h_{pzt}+h_b+h_p$, Young's modulus E_c and Poisson ratio γ_c for this three-layer structure are

$$E_c = C_1'E' + C_2'E_p + \frac{C_1'C_2'E'E_p(\gamma_p - \gamma')^2}{(C_1'E_p(1-\gamma'^2) + C_2'E'(1-\gamma_p{}^2))} \qquad (2.13)$$

$$\gamma_c = \frac{C_1'\gamma_p E_p (1-\gamma'^2) + C_2'\gamma' E'(1-\gamma_p{}^2)}{(C_1'E_p(1-\gamma'^2) + C_2'E'(1-\gamma_p{}^2))} \qquad (2.14)$$

where $C_1' = {}^{h_p}\!/_{h_{all}}$ and $C_2' = {}^{h''}\!/_{h_{all}}$.

The moment M_2 can be found from the fixed boundary condition (Timoshenko et al 1959)

$$M_2 = \frac{2b^2 M_{11}}{(1-\gamma_p)a^2 + (1+\gamma_p)b^2} \qquad (2.15)$$

where a is the diameter of the passive plate and b is the radius of the PZT disk

Set K as boundary effect parameter

$$M_2 = K \frac{2b^2 M_{11}}{(1-\gamma_p)a^2 + (1+\gamma_p)b^2} \tag{2.16}$$

where $K = 0$ for simple support, $K = 1$ for a fixing boundary, and $0 < K < 1$ for the boundary between simple support and fixing boundary.

For the passive plate, a general solution for its deflection W_1 in the z direction is given by

$$W_1(r) = \frac{b^2 M_{11}}{D_p(a^2 - b^2)((1-\gamma_p)a^2 + (1+\gamma_p)b^2)}[\frac{a^2(2k-1+\gamma_p) - b^2(1+\gamma_p)}{2(1+\gamma_p)}(a^2 - r^2) - \frac{a^2[(2k-1-\gamma_p)b^2 - a^2(1-\gamma_p)]}{1-\gamma_p}\log\frac{r}{a}]$$

(2.17)

where r is the radius of the passive plate and the flexural modulus for the passive plate D_p is given by

$$D_p = E_p h^3 / [12(1-\gamma_p{}^2)] \tag{2.18}$$

The deflection W_2 for the multiple-layer follows [21]

$$W_2(r) = W_1(r=b) + \frac{M_1}{2D_c(1+\gamma_c)}(b^2 - r^2) \tag{2.19}$$

where the flexural modulus for the multi-layer structure D_c is given by

$$D_c = E_c h^3 / [12(1-\gamma_c{}^2)]$$

From the continuity condition

$$\left.\frac{dW_1}{dr}\right|_{r=b} = \left.\frac{dW_2}{dr}\right|_{r=b} \tag{2.20}$$

The moment M_{11} can be found as the following

$$M_{11} = -\frac{M_1 D_p (a^2 - b^2)((1-\gamma_p)a^2 + (1+\gamma_p)b^2)}{D_c(1+\gamma_c)\left(\frac{b^2\left[a^2(2k-1+\gamma_p) - b^2(1+\gamma_p)\right]}{1+\gamma_p} + \frac{a^2\left[b^2(2k-1-\gamma_p) - a^2(1-\gamma_p)\right]}{1-\gamma_p}\right)}$$

(2.21)

When the boundary parameter *K* is set to 1, the solutions of the PZT actuator for the deflection W_1, W_2 and M_{11} are the same as those in [21]

$$W_1(r) = \frac{M_{11} b^2}{2D_p((1-\gamma_p)a^2 + (1+\gamma_p)b^2)}\left[-r^2 + 2a^2 \log\frac{r}{a} + a^2\right] \tag{2.22}$$

$$W_2(r) = \frac{M_{11} b^2}{2D_p((1-\gamma_p)a^2 + (1+\gamma_p)b^2)}\left[-b^2 + 2a^2 \log\frac{b}{a} + a^2\right] + \frac{M_1}{2D_c(1+\gamma_c)}(b^2 - r^2) \tag{2.23}$$

$$M_{11} = -\frac{M_1 D_p ((1-\gamma_p)a^2 + (1+\gamma_p)b^2)}{D_c(1+\gamma_c)(a^2 - b^2)}$$

(2.24)

From equation (2.17) and (2.19), it is easy to see that the dimensions of the PZT, the passive plate and the bonding layer and their Young's modulus have a significant influence on the magnitude of the microactuator deflection. Meanwhile, some nondimensional variables such as $(b/a)^2$, $(E_b h_b^3 / E_p h_p^3)$, and $(E_{pzt} h_{pzt}^3 / E_p h_p^3)$ are expected to have effects on the performance of the piezoelectric microactuator. Details will be discussed in the following section.

2.3.2. Comparison with Data from Experiments and Finite Element Simulation

The analytical model derived in previous section allows one to directly predict the performances of the bimorph system. However, such analytical solution needs to be verified first since the derivation process involves a major assumption of linear strain distribution among the PZT disk, the bonding material, and the passive plate. One effective way to verify this analytical solution is to compare it with the results from finite element analysis. Due to dimensional symmetry, only quarter of the piezoelectric actuator is considered in this chapter using a commercial FEM package, ANSYS 5.7 with fixing and symmetrical boundaries. The 10-node Solid-92 is chosen to model the passive plate and the bonding layer. The coupled field scalar Solid-98 is used to model the PZT layer. There are approximately 4000 elements in this model. Another way to verify this analytical equation is to compare its results with available experimental using the same dimensions and materials for the PZT disk, the bonding material, and the passive plate [14]. The properties for the PZT (PZT-5A), the conductive epoxy (EPO-TEK H31), and the passive plate are summarized in Table 2.1. The piezoelectric microactuator dimensions are listed in Table 2.2. The working voltage is 50V (zero-to-peak).

Table 2.1: Properties of the PZT, conductive epoxy and passive plate (Ref. 14)

	Property	Tensor (in order of x, y, z, xy, yz and xz)
PZT	Piezoelectricity **e** (Cm^{-2})	$\begin{bmatrix} 0 & 0 & -5.4 \\ 0 & 0 & -5.4 \\ 0 & 0 & 15.8 \\ 0 & 0 & 0 \\ 0 & 12.3 & 0 \\ 12.3 & 0 & 0 \end{bmatrix}$
	Permittivity ε' (Fm^{-1})	$\begin{bmatrix} 8.107 & 0 & 0 \\ 0 & 8.107 & 0 \\ 0 & 0 & 7.346 \end{bmatrix} \times 10^{-9}$
	Compliance **S'** ($m^2\ N^{-1}$)	$\begin{bmatrix} 16.4 & -5.75 & -8.45 & 0 & 0 & 0 \\ 0 & 16.4 & -8.45 & 0 & 0 & 0 \\ & & 18.8 & 0 & 0 & 0 \\ & & & 44.3 & 0 & 0 \\ & \mathit{symmetric} & & & 47.5 & 0 \\ & & & & & 47.5 \end{bmatrix} \times 10^{-12}$
Epoxy	Young's Modulus E_b (GPa)	5.17
	Poisson Ratio γ_b	0.3
Glass	Young's Modulus E_p (GPa)	62.75
	Poisson Ratio γ_p	0.2

Table 2.2: Dimensions for the piezoelectric microactuator simulation

The passive plate radius a (mm)	3.0
The passive plate thickness h_p (μm)	500
Piezoelectric disk radius b (mm)	2.0~2.5
Piezoelectric disk thickness h_{pzt} (μm)	200
Bonding layer thickness h_b (μm)	20

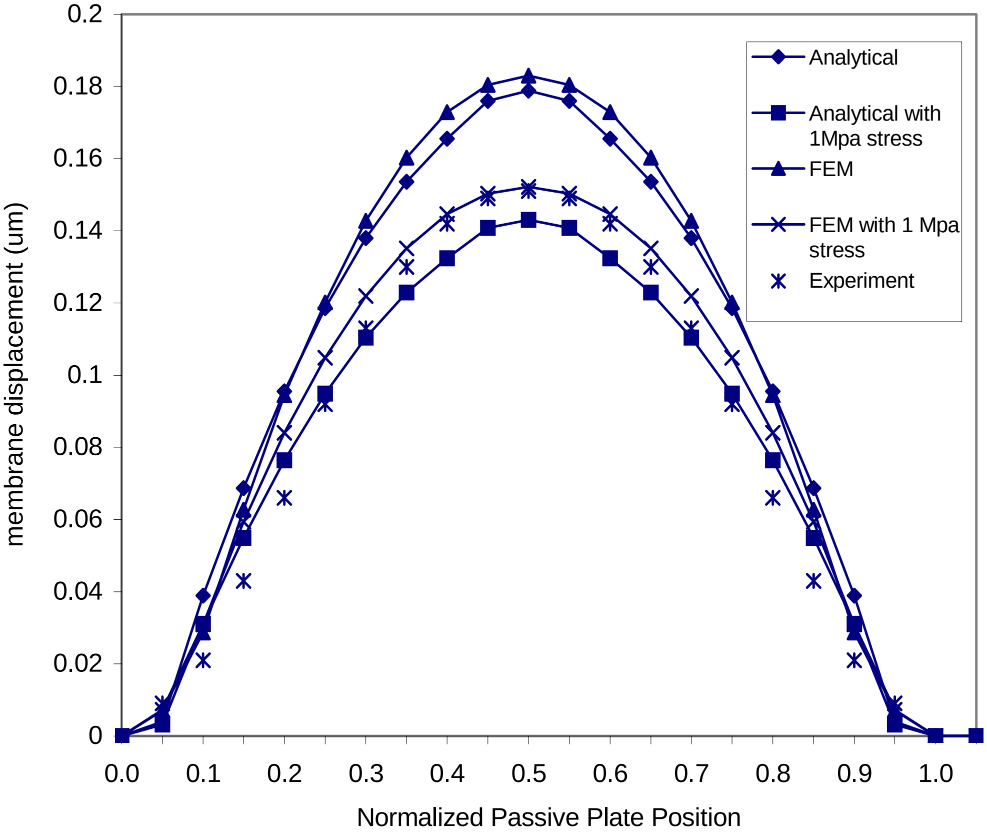

Figure 2.4: Comparison of the passive plate profiles from analytical calculation, experiment data, and FEM simulation. The working voltage $V_{0\text{-}p}$ = 50 V, the bonding layer thickness ratio $h_{b\text{-}p} = 0.04$, the passive plate thickness h_p = 500 μm and $K = 1$.

The passive plate deflection from the analytical solution, FEM simulation, and experimental results is shown in Fig.2.4. The maximum deflection at the center of the passive plate from the analytical equation is 0.1788 μm and the deflection from FEM simulation is 0.1829 μm, resulting in a discrepancy less than 3%. The bonding process often introduces some residual thermal stress. From the simulation, 1 Mpa residual tensile stress is found inside the passive plate. After including this stress, we found that the passive plate deflection from our analytical prediction agrees well with experiment study. This suggests that the analytical model developed in this work is valid.

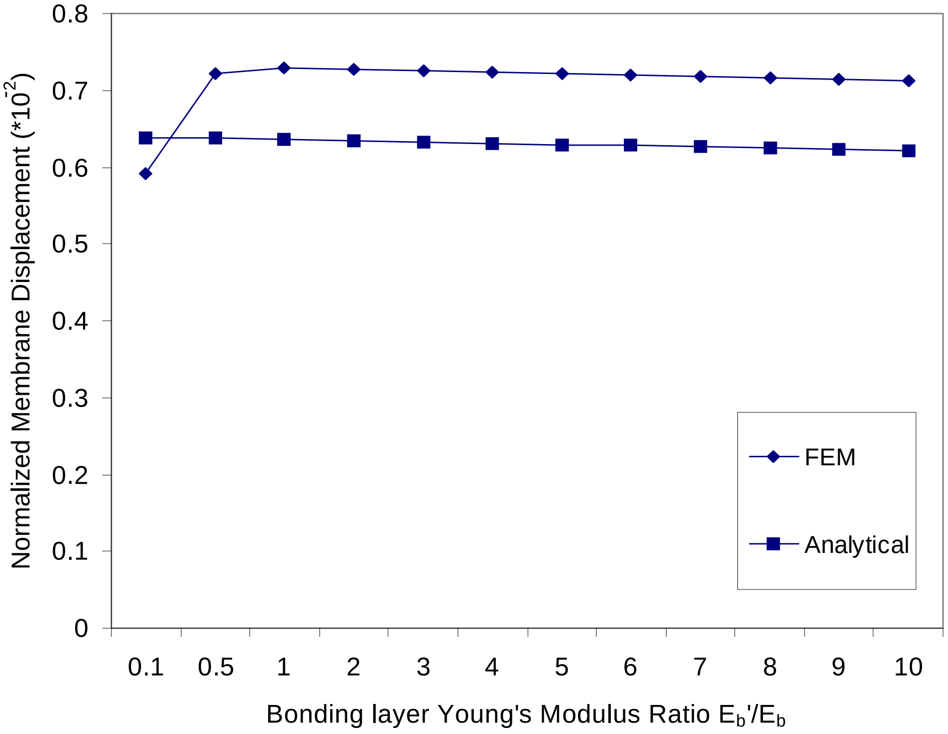

(a)

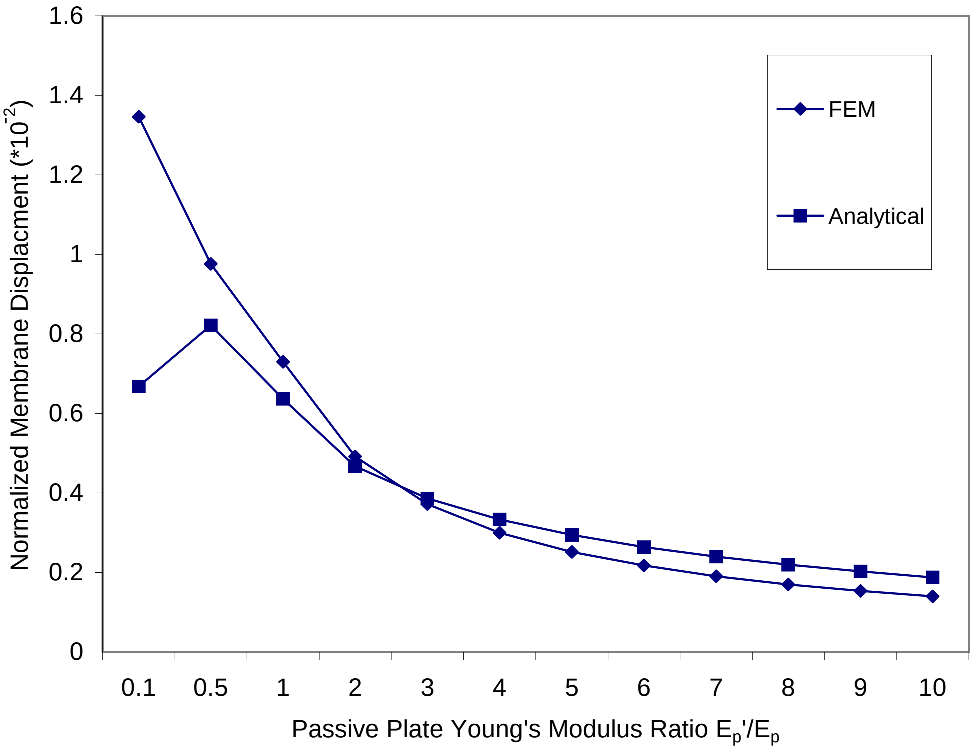

(b)

Figure 2.5: Results from FEM and analytical calculation with (a) different bonding layer Young's Modulus E_b', and (b) different passive plate Young's Modulus E_p', normalized with the case that the mechanical properties of material and dimensions are in Table 2.1 and 2.2.

We also extended the investigation to other bonding materials and passive plates by comparing the analytical results with those from the FEM simulation. Because the typical Poisson ratio of materials is from 0.2 to 0.3, the passive plate deflection change due to Poisson ratio variation is less than 3%. Therefore, only the Young's Modulus effect is investigated. We found that there is no significant error from this analytical solution if we change Young's Modulus of the bonding layer from 0.5 to 10 times that of the current one (Fig. 2.5a). However, when Young's Modulus ratio is below 0.2, the linear strain assumption in deriving the analytical solution is not valid any more. For the passive plates of various Young's Modulus from 30 GPa to 600 GPa, Figure 2.5b suggests this analytical equation is able to predict reliable passive plate deflections. But if this ratio is below 0.5, this analytical equation fails to predict accurate the passive plate deflection since the linear strain assumption is not valid. From the practical point of view, this range of Young's Modulus from 30 GPa to 600 GPa covers almost all available MEMS plate materials such as glass, silicon, silicon nitride, and most metals.

2.3.3. Optimization of a PZT Microactuator

2.3.3.1. PZT Disk Effects

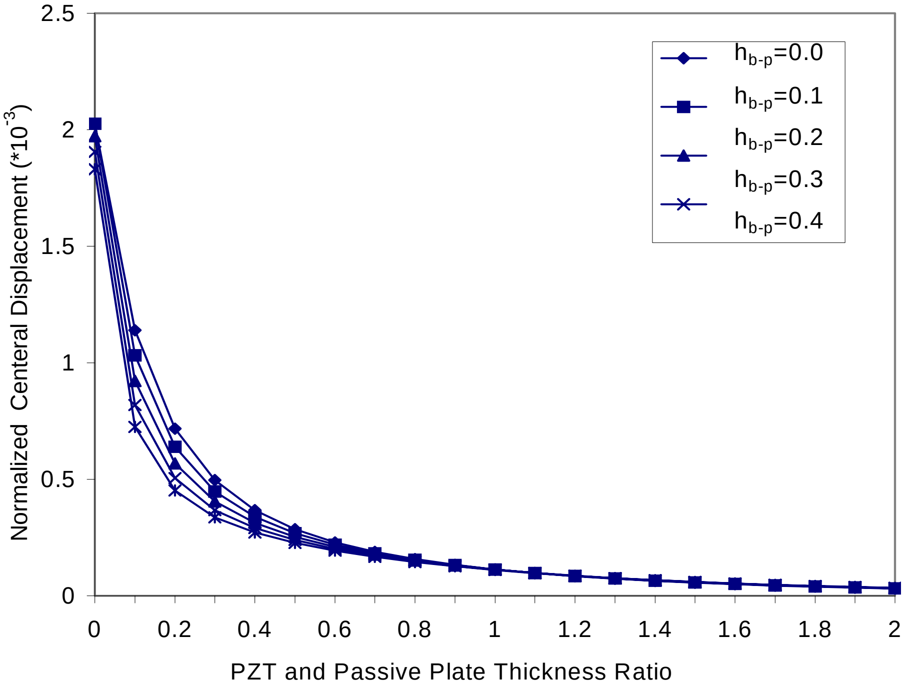

(a)

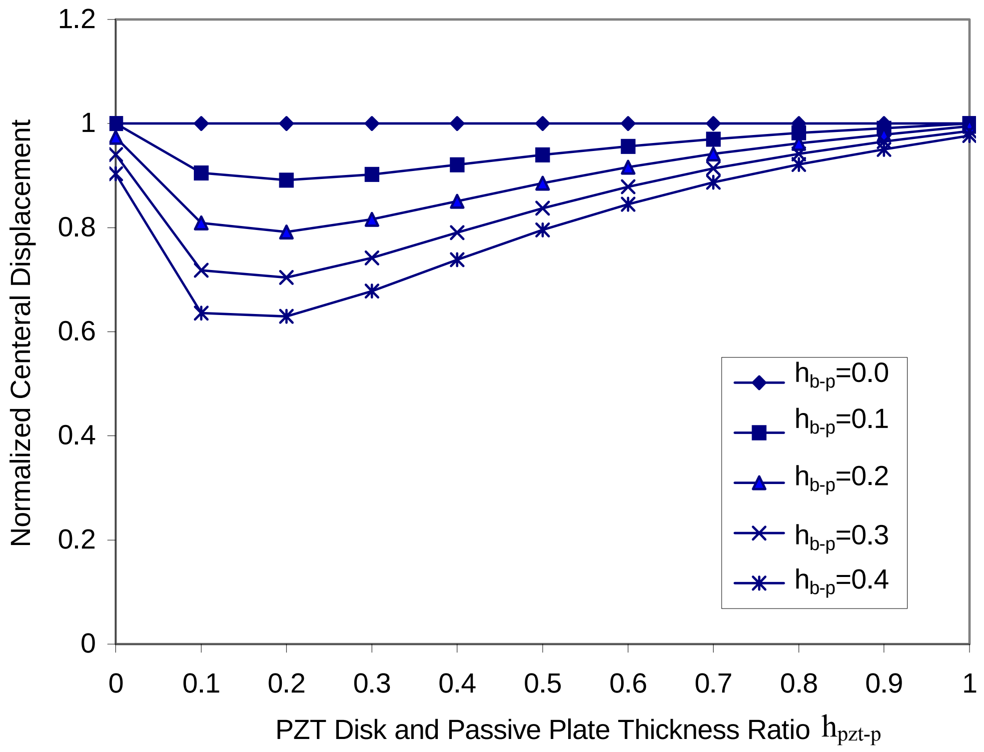

(b)

Figure 2.6: The central passive plate deflections at different PZT disk thickness, (a) normalized with the passive plate thickness h_p = 500 μm, (b) normalized with the case that the bonding layer thickness ratio $h_{b\text{-}p}$ = 0 (no bonding layer case).

The PZT disk is an important element for piezoelectric actuation in the bimorph system. The dimensions of the PZT disk play a significant role in the actuator design. Practically, the bonding layer is less than 100 μm (typically around 20μm), and rather thin compared to the passive plate. Therefore, we investigated the effect of PZT/passive plate thickness ratio $h_{pzt\text{-}p}$ on the passive plate deflection for bonding layer/plate thickness ratio, $h_{b\text{-}p}$ ranging from 0 to 0.4 as shown in Figure 2.6a. We found that the passive plate deflection decreases with increasing the bonding layer/passive plate thickness ratio $h_{b\text{-}p}$

and increasing the PZT/passive plate thickness ratio h_{pzt-p}. For the PZT/passive plate thickness ratio h_{pzt-p} less than 0.5, the bonding material thickness effect became important. In order to find the bonding layer effect in detail, the data is normalized with the passive plate deflection with no bonding layer. Figure 2.6b shows the bonding layer effect is the strongest when the PZT thickness ratio h_{pzt-p} is around 0.15. However, when this thickness ratio h_{pzt-p} is beyond 0.8, the bonding layer effect is limited. In Figure 2.7a, the passive plate deflection increases when the PZT/passive plate squared radius ratio increases, but decreases with the bonding material thickness ratio h_{b-p}. In Figure 2.7b, when the bonding layer thickness ratio is larger than 0.3, the passive plate deflection drops down to a value of 80% of the passive plate deflection without the bonding layer. This result implies the bonding layer reduces the passive plate deflection significantly when the bonding layer thickness ratio is above 0.3.

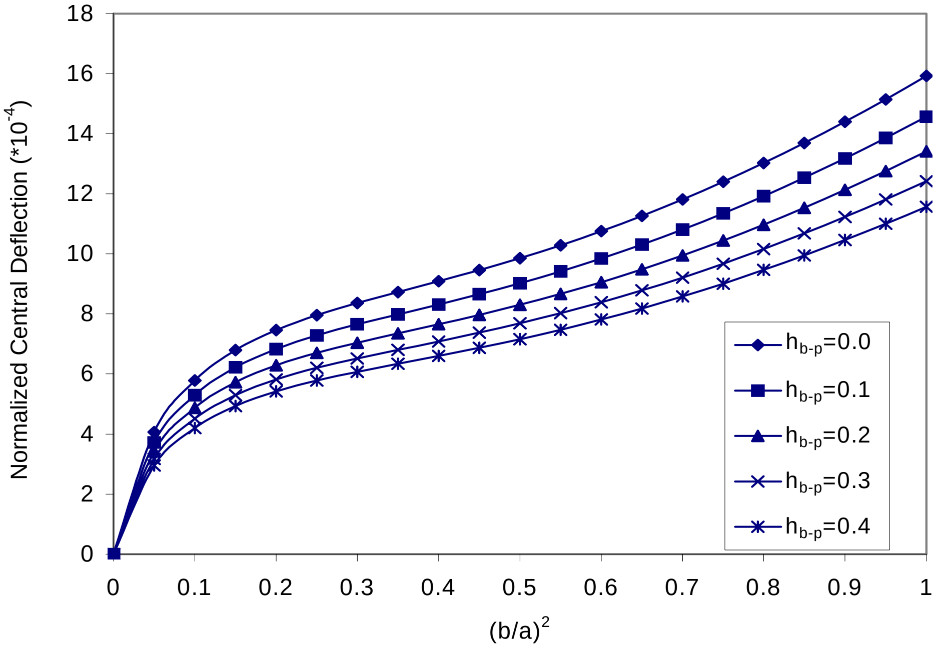

(a)

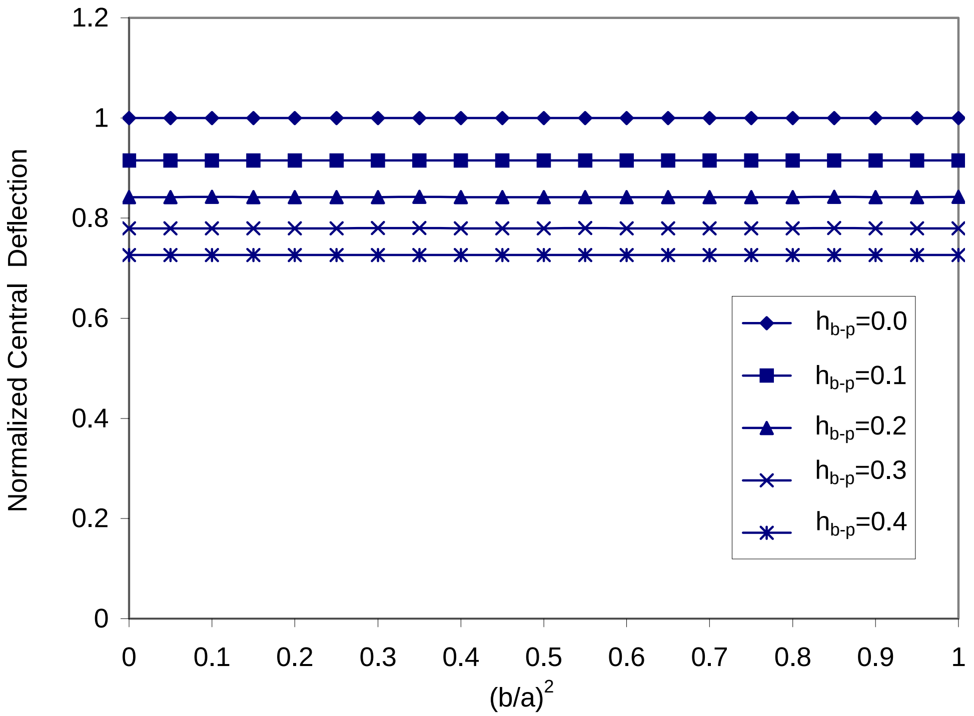

(b)

Figure 2.7: The passive plate central deflection at different radius ratios of PZT disk and the passive plate, (a) normalized with the passive plate thickness h_p = 500μm, (b) normalized with the case that the bonding layer thickness ratio $h_{b\text{-}p} = 0$ (no bonding layer case).

2.3.3.2. Bonding Material Effects

In previous studies of developing analytical solutions for the circular piezoelectric microactuators, the bonding layer effects on the actuator performance were usually neglected in order to simplify the model [15, 16]. The analytical solution derived in this chapter allows one to investigate the bonding layer material effect including its dimensions and Young's Modulus as shown in Figure 2.8. Increasing the bonding material thickness will reduce the passive plate deflection, but when the PZT/passive plate thickness ratio $h_{pzt\text{-}p}$ is above 0.4, the maximum passive plate deflection does not show a significant change with respect to $E_b h_b^3 / E_p h_p^3$. This implies the bonding material effect is limited and negligible for a thick PZT actuator. However, for a thin PZT disk (e.g., less than 200 µm thick), we found that the bonding material effect cannot be neglected. But this does not mean the thinner PZT gives a larger deflection. We performed this analysis under a constant voltage. In practice, a piezoelectric material has maximum allowable field strength. If this maximum allowable field strength is exceeded, the material will degrade and eventually lose its piezoelectric properties. If the electric field remains constant, there exists an optimal PZT thickness for the specific bonding layer thickness ratio as depicted in Figure 2.9. Moreover, there is a slight increase of this optimal PZT disk thickness when the bonding layer thickness increases.

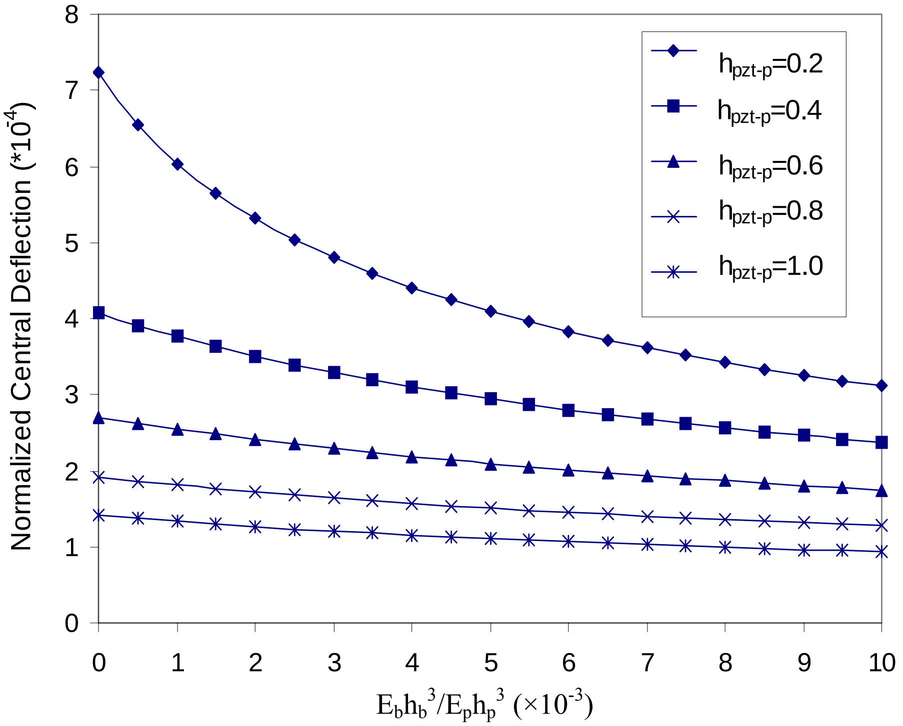

Figure 2.8: The passive plate center deflections at different $E_bh_b^3/E_ph_p^3$ ratios normalized with case that the passive plate thickness h_p is 500 µm.

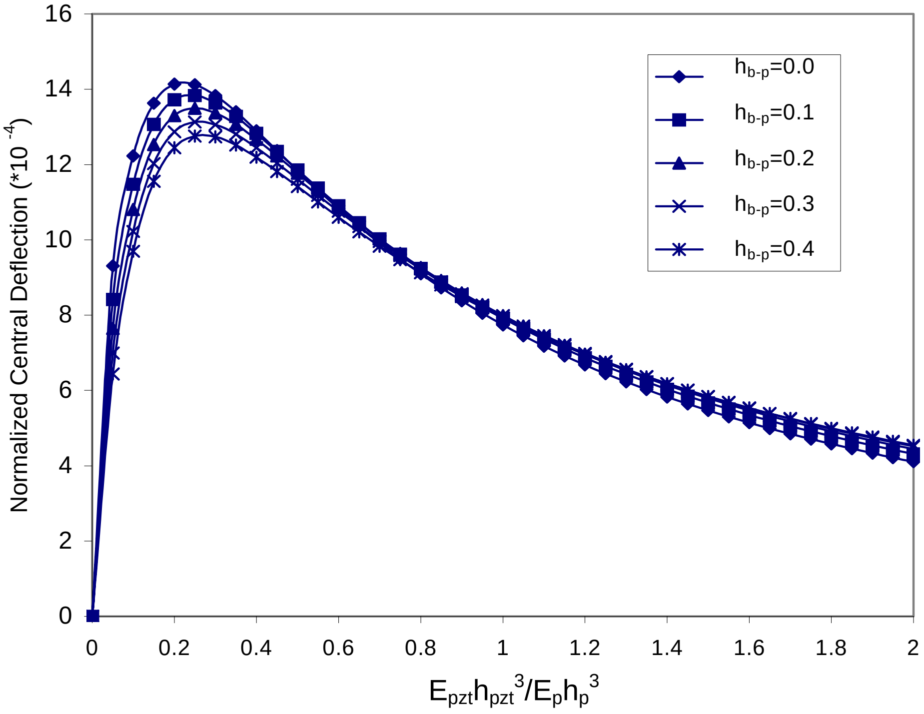

Figure 2.9: The passive plate center deflections at different $E_{pzt}h_{pzt}^3/E_ph_p^3$ ratios under a constant electrical field normalized with case that the passive plate thickness h_p is 500 μm.

2.3.3.3. Passive Plate Effects

The passive plate dimensions also have an important role on the actuator performances. Considering practical applications, we focus the study on passive plate thickness and diameter ratio from 0 to 0.5. Meanwhile, the PZT diameter effect is coupled in this investigation with the PZT and the passive plate diameter ratio R_{pzt-p} (D_{pzt}/D_p) ranging from 0.2 to 1.0. In Figure 2.10, the maximum achievable passive plate deflection reaches a peak when the passive plate thickness/diameter ratio is around 0.01 to 0.02. Although this ratio is not practically useful for actuator design, this analytical solution does suggest that in order to enhance the performance of the single layer piezoelectric actuator, the passive plate thickness/diameter ratio needs to be as close to 0.02 as possible. Also, a larger diameter PZT disk will yield bigger deflection.

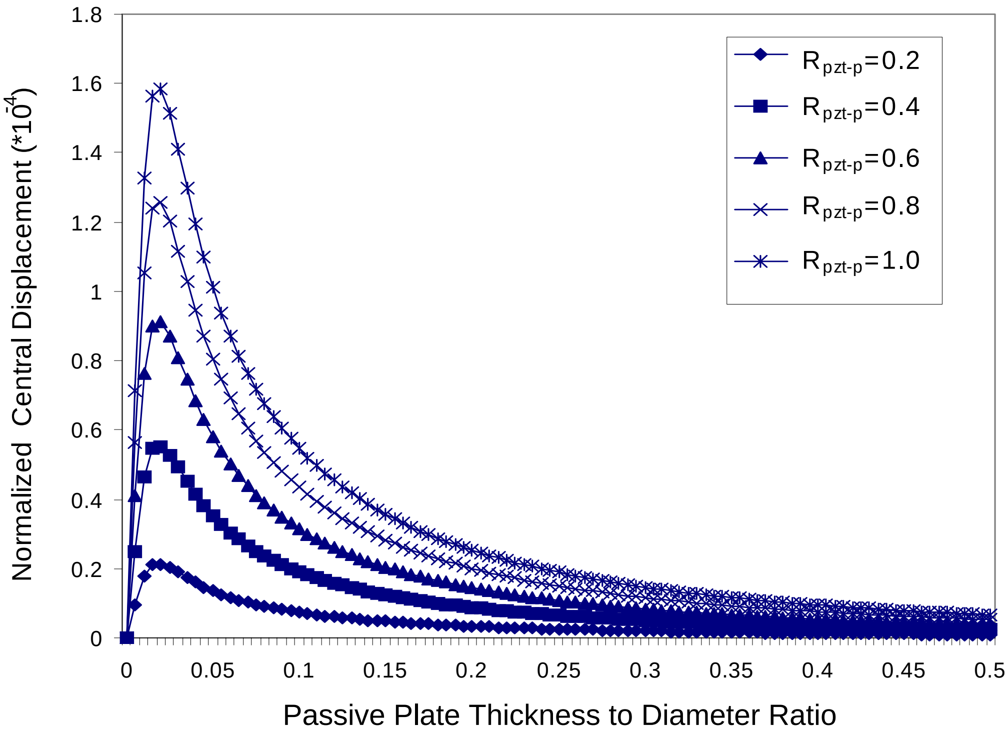

Figure 2.10: The passive plate central deflection at different passive plate dimensions, normalized with the plate diameter a = 6mm.

2.4. System Level Modeling of a Valveless PZT Micropump

2.4.1. Flow Characteristics of a Diffuser and a Nozzle

A diffuser is by definition a device for reducing the velocity and increasing the static pressure of a fluid passing through a system (Figure 2.11). It is often used in internal flow systems. The reduction of the velocity for an expanding cross section follows from the continuity equation. The static pressure is therefore increased according to Bernoulli's equation. The geometry of the diffuser is very simple, but the flow in it is very complex. Due to the negative pressure gradient, the flow may separate from the sidewall which causes large pressure loss Δp that deteriorates the function of the diffuser. For the micromachined diffusers, reported data is limited. It is important to give an explanation of the working principle of the diffuser element and estimate the diffuser element efficiency based on empirical results in the literature.

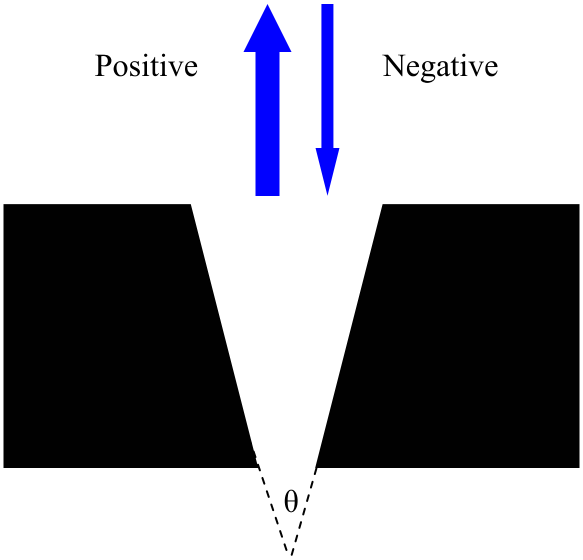

Figure 2.11: A cross-sectional view of a typical micromachined diffuser.

The pressure loss in internal flow systems is normally given by a loss coefficient K_1 that is related to the pressure drop Δp by

$$\Delta p = K_1 \rho u^2 / 2 \tag{2.24}$$

where ρ is the fluid density and u is the mean velocity in the upstream.

For a diffuser element, it is practical to relate the pressure loss to the narrowest cross section, the neck by

$$\Delta p = \zeta \rho u^2{}_{neck} / 2 \tag{2.25}$$

where ζ is the pressure loss coefficient and u_{neck} is the mean velocity in the neck. The relation between K_1 and ζ is a simple geometrical area relation given by

$$\zeta = K_1 A \left({A_{neck}}\big/{A_{upstream}} \right)^2 \tag{2.26}$$

where A is the cross-section area of the channel. If interactions between the different parts of the diffuser element are neglected, the total pressure loss can be calculated as the sum of the losses on the different parts.

In order to achieve the best pump performances, the losses in the positive direction should be minimized while maximizing the losses in the negative direction. At the outlet, the flow always forms a jet regardless of the shape and $K_1 = 1$. At the inlet, the losses should be small in the positive direction. This is achieved with a rounded inlet and $K_1 = 0.05$. In the negative direction the losses should be as high as possible and a sharp inlet is used with $K_1 = 1$.

Experimental data for diffusers are commonly presented as performance maps in literature [Japikse et al 1998]. From such a performance map, the maximum pressure recovery Cp for the diffuser can be estimated and the loss coefficient can be calculated as

$$K_{diffuser}=1-\left({}^{A_{in}}\!/\!_{A_{out}} \right)^2 - Cp \qquad (2.27)$$

where A_{in} is the inlet area and A_{out} is the outlet area. The losses are minimized when Cp is maximized. From the performance map [Japikse et al 1998], we find that $Cp = 0.77$. It is known that the performance is highly dependent on the boundary conditions at the inlet. In the opposite direction, the losses are always small with K_1 approximately 0.03.

The same type of analysis can be made for a nozzle element in the dynamic micropump, henceforth called valveless nozzle pump. A nozzle element is a flow channel with a large opening in the positive direction as illustrated in Figure 2.12.

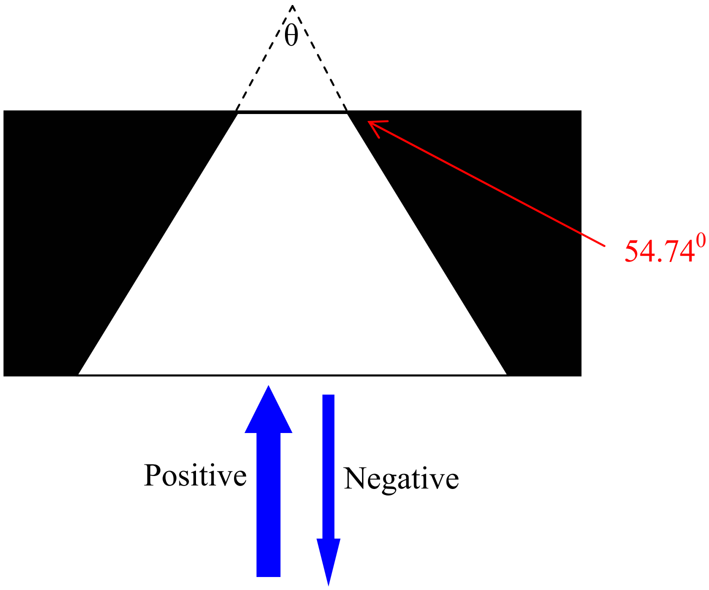

Figure 2.12: A cross-sectional view of a nozzle.

The nozzle elements depend on a different mechanism compared to the diffuser elements. The nozzle element depends on the inlet edge at the narrowest part and the "vena-contracta" effect. The diverging angle direction does not work as a diffuser since no pressure is recovered and the losses are higher than for sudden expansion. The converging wall direction is the positive direction. The resulting pressure loss coefficients ζ for diffuser and nozzle are summarized in Table 2.3.

Table 2.3. Summary of flow efficiency of different nozzle and diffuser elements

	$\theta = 70^\circ$	$\theta = 70^\circ$	$\theta = 5^\circ$	$\theta = 5^\circ$
	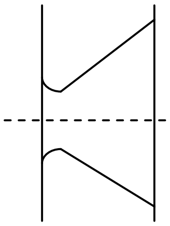	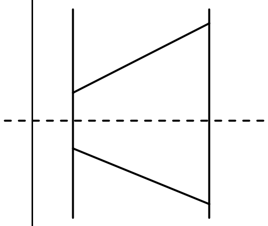	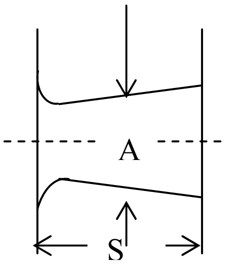	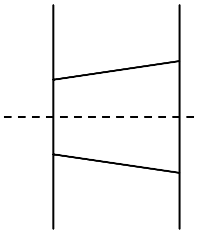
$\zeta+$	1.1	1.1	1	1
$\zeta-$	1.4-1.6	1.05-1.25	0.55-0.7	0.2-0.35

2.4.2. Modeling of Valveless PZT Micropump

The important parts of a micropump are identified and the structure is divided into different elements for which boundary conditions can be described. At the first, the control volume as shown in Figure 2.13 is used to derive the coupling equation between the fluid and the PZT actuator.

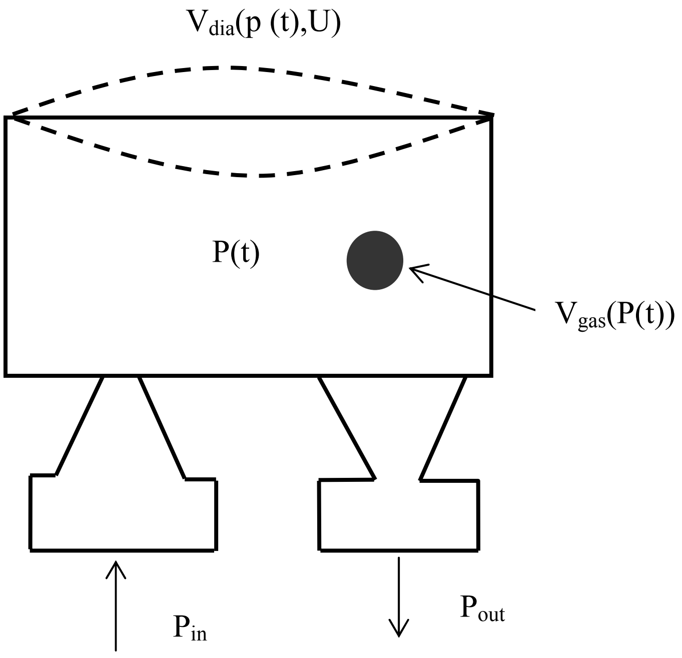

Figure 2.13: A control volume of a valveless micropump chamber.

The conservation of mass is given by

$$\frac{d}{dt}\Big(\iiint_{cv} \rho dv\Big) + \iint_{cs} \rho(u \bullet n)dA = 0 \qquad (2.35)$$

Where *CV* is the control volume, *CS* is the control surface, ρ is the density of fluid, *u* is the velocity vector and *n* is the normal vector with respect to the control surface. For the control volume in Figure 2.13, we have

$$\frac{d}{dt}[\rho_{liquid}(p)V_{liquid}(p) + \rho_{liquid}(p))V_{gas}(p)] - \rho_{liquid}(\Phi_{in} - \Phi_{out}) = 0$$

(2.36)

where V_{liquid} is the control volume of fluid, V_{gas} is the gas volume contained inside the pump chamber, Φ_{in} and Φ_{out} are flow rates that flow into and flow out of the chamber respectively and V_{liquid} is given by

$$V_{liquid}(p,t) = V_{chamber}(p) + V_{dia}(p,U,t) - V_{gas}(p) \tag{2.37}$$

where $V_{chamber}$ is the volume of the pump chamber, V_{dia} is the volume variation induced by membrane deflection. Assume the flow is incompressible and the chamber wall is stiff enough to avoid any deformation except the membrane, we have

$$\rho_{liquid}\left(\frac{dV_{dia}}{dp}\frac{dp}{dt}+\frac{dV_{dia}}{dU}\frac{dU}{dt}\right)-\rho_{liquid}\frac{dV_{gas}}{dp}\frac{dp}{dt}+\rho_{gas}(p)\frac{dV_{gas}(p)}{dt}+V_{gas}(p)\frac{d\rho_{gas}(p)}{dt}=\rho_{liquid}(\Phi_{in}-\Phi_{out}) \tag{2.38}$$

where ρ_{gas} is the density of gas contained in the chamber.

Assuming the gas in the chamber is conservative, we have

$$(\rho_{gas}(p) + d\rho)(V_{gas}(p) + dV) = \rho_{gas}(p)V_{gas}(p) \tag{2.39}$$

Therefore,

$$\frac{d\rho}{dp} = -\frac{\rho_{gas}(p)}{V_{gas}(p)}\frac{dV}{dp} \tag{2.40}$$

Assume ideal gas for the contained gas, we have

$$\frac{dV_{gas}}{dp} = -\frac{V_{gas,0}P_0}{(P+P_0)^2} \tag{2.41}$$

where P_0 and P are pressures outside and inside the chamber, respectively.

Equation (2.38) then becomes

$$\frac{dV_{dia}}{dp}\frac{dp}{dt}+\frac{dV_{dia}}{dU}\frac{dU}{dt}-\frac{dV_{gas}}{dp}\frac{dp}{dt}=\Phi_{in}-\Phi_{out} \tag{2.42}$$

and for the contained gas,

$$\frac{dV_{dia}}{dp}\frac{dp}{dt}+\frac{dV_{dia}}{dU}\frac{dU}{dt}+\frac{V_{gas,0}P_0}{(P+P_0)^2}\frac{dp}{dt}=\Phi_{in}-\Phi_{out} \tag{2.43}$$

For the flow in the nozzles, assuming incompressible and steady flow, the extended Bernoulli equation gives

$$gz_{in}+\frac{P_{in}}{\rho}+\frac{1}{2}\psi_{in}\overline{U_{in}}^{2}=gz_{out}+\frac{P_{out}}{\rho}+\frac{1}{2}\psi_{out}\overline{U_{out}}^{2}+\xi\frac{d\Phi}{dt}+\frac{\Delta P_{loss}}{\rho} \tag{2.44}$$

Where Z_{in} and Z_{out} are potentials of flow-in and flow-out, P_{in} and P_{out} are pressures of flow-in and flow-out, ΔP_{loss} is the pressure loss of the fluid, Φ is the flow rate, ξ is the flow resistance, ρ is the fluid density, g is acceleration of gravity and ψ is kinetic energy coefficient.

Since the change of kinetic energy is negligible compared to pressure drop, Eq.2.44 can be changed into the following

$$gz_{in}+\frac{P_{in}}{\rho}=gz_{out}+\frac{P_{out}}{\rho}+\xi\frac{d\Phi}{dt}+\frac{\Delta P_{loss}}{\rho} \tag{2.45}$$

For the inlet,

$$P_{in}=P(t)+\rho\xi\frac{d\Phi_{in}}{dt}+\Delta P_{loss}+\rho gH$$

(2.46)

For the outlet,

$$P_{out} = P(t) - \rho\xi \frac{d\Phi_{out}}{dt} - \Delta P_{loss} - \rho g H \tag{2.47}$$

From the above derivation, one dynamic model of PZT actuated valveless micropump is achieved. The following four differential equations describe micropump dynamic performance.

$$\frac{dV_{dia}}{dp}\frac{dp}{dt} + \frac{dV_{dia}}{dU}\frac{dU}{dt} + \frac{V_{gas,0}P_0}{(P+P_0)^2}\frac{dp}{dt} = \Phi_{in} - \Phi_{out} \tag{2.43}$$

$$P_{in} = P(t) + \rho\xi \frac{d\Phi_{in}}{dt} + \Delta P_{loss} + \rho g H \tag{3.46}$$

$$P_{out} = P(t) - \rho\xi \frac{d\Phi_{out}}{dt} - \Delta P_{loss} - \rho g H \tag{2.47}$$

Numerical simulation using *FORTRAN* was carried out to analyze the micropump performance. When the working voltage and the working frequency of are chosen as 50 V and 50 Hz, the membrane thickness and radius are 500 μm and 2.5 mm and the nozzle neck diameter and the nozzle length are 80 μm and 400 μm, the performances of the micropump are shown in Figure 2.14.

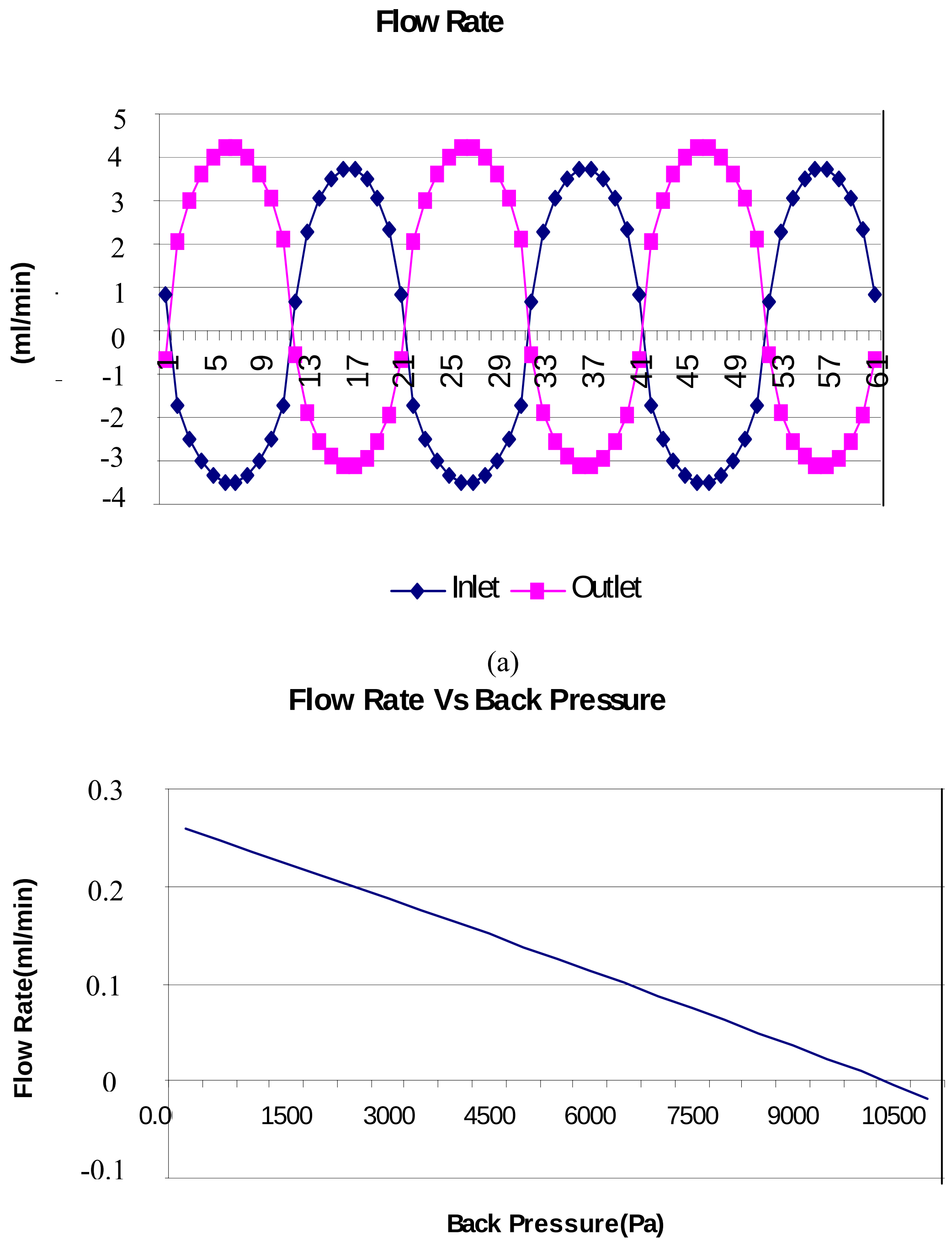

(a)

(b)

Figure 2.14: Results of (a) the inlet and outlet flow rates of the micropump, and (b) the working characteristics of the micropump.

2.5. Conclusions

An analytical model for the analysis of a PZT actuator was developed based on an assumption of linear strain distribution along the PZT disk, the bonding layer, and the passive plate. Results from both FEM simulation and experiment data verified that this analytical model is valid. One important aspect of this analytical model is that it can predict the performances of the PZT actuator system with different design parameters and operation conditions, and therefore allow one to optimize the design. The dimensions and properties of the PZT disk play a significant role in the actuator performance. The passive plate deflection decreases as the PZT thickness and bonding material thickness increase and increases as the PZT radius increases. The bonding layer effects become important for a thin PZT disk. The mechanical properties such as Young's Modulus also have certain effects on the passive plate deflection. When the electric field is kept constant, there exists an optimal PZT thickness. When the bonding layer thickness increases, this optimal PZT thickness also increases. Moreover, this analytical solution suggests that an optimal value for the passive plate thickness/diameter ratio is about 0.02 in order to get high performance actuator design. Finally, a system level analytical model for the PZT-actuated valveless micropump is proposed to study its performances.

2.6. References

1. Chee C.Y.K., Tong L., Steven G.P., 1998, *Journal of Intelligent Material Systems and Structure,* 9, 3-19.

2. Crawley E.F., Anderson E.H., 1990, *Journal of Intelligent Material Systems and Structure*, 1, 4-25.
3. Kim S. J., Jones J.D., 1991, *AIAA. J,* 29, 2047-53.
4. Ray M.C., Bhattacharya R., Samanta B., 1993, *AIAA J.*, 31, 1684-91.
5. Chaudhry Z., Rogers C. A., 1994, *AIAA J.,* 32, 1289-94.
6. Yanagisawa T., Nakagawa Y., 1993, *Trans. Inst. Electron. Informat. Commum. Eng. A,* 76, 1261-9.
7. Dobrucki A. B., Pruchnicki P., 1997, *Sensors and Actuators A,* 58, 203-12.
8. Tzou H.S., 1994, Kluwer Publishing Company.
9. Larson P.H., 1994, PhD Thesis, University of Delaware.
10. Stemme E., Stemme G., 1993, *Sensors and Actuators A,* 39, 159-167.
11. DeVoe D. L., Pisano A. P., 1997, *Journal of Microelectromehcanical Systems*,6, 266-270.
12. DeVoe D. L., Pisano A. P., 2001, *Journal of Microelectromehcanical Systems*, 10, 180-186.
13. Yoon H. S., Washington G., 1998, *Smart Materials and Structures*, 7, 537-542.
14. Morris C. J., Forster F. K., 2000, *Journal of Micromechanics & Microengineering,* 10, 459-465.
15. Cao L., Mantell S., Polla D., 2001, *Sensors and Actuators A*, 94, 1-9.
16. Li S. F., Liu Y., Chen S. C., 2001*, Proceedings of SPIE*, 4560, 67-74.
17. Gerlach T., Wurmus H., 1995, *Sensors and Actuators A*, 50, 135-140.

18. Olsson A., Stemme G., Stemme E., 1995*, Sensors and Actuators A,* 46-47, 549-556.
19. Forster E. K., Bardell R. L, Abramowitz M. A., Sharma N. R., Blanchard A., 1995, *Proceedings of IMECE*, ASME.
20. Christensen R. M., 1979, John Wiley & Sons, Inc.
21. Timoshenko S., Woinowsky-Krieger S., 1995, Second Edition McGraw-Hill.
22. Stemme E., Stemme G., 1993, *Sensors and Actuators A*, 39, 159-167
23. Zengerle R. and Richter M., 1994, *Journal of Micromechanics and Microengineering,* 4, 192-204.
24. Olsson A., Stemme G. and Stemme E., 1999, *Journal of Micromechanics and Microengineering,* 9, 34-44.
25. Gerlach T., 1997, *Transducer'97*, Chicago, 1035-1038.
26. Olsson A., Stemme G. and Stemme E., 2000, *Sensors and Actuators A,* 84, 65-175.
27. Gerlach T., Wurmus H., 1995, *Sensors and Actuators A,* 50, 135-140.
28. Olsson A., Stemme G. and Stemme E., 1997, *Transducer'97* Chicago, 1039-1042.
29. Nguyen N. T. and White R. M., 1999, *Sensors and Actuators A,* 77, 229-236.
30. Gong Q. L., Zhou Z.Y., Yang Y. H. and Wang X. H., 2000, *Sensors and Actuators A,* 83, 200-207
31. Pan L. S., Ng T. Y, Liu G. R., Lam K. Y. and Jiang T. Y., 2001, *Sensors and Actuators A,* 3052, 1-9

32. Morris C. J. and Forster F. K., 2000, *Journal of Micromechanics and Microengineering,* 10, 459-465
33. Bardell R. L., Sharma N. R., Forster F. K., Afroowitz M. A. and Penney R. J., 1997, *Proceedings of MEMS ASME*, 47-53
34. Olsson A., Enoksson P., Stemme G. and Stemme E., 1997, *Journal of Microelectromechanical systems,* 6 ,161-166

Chapter 3: A Continuous-Flow Polymerase Chain Reaction Microchip with Regional Velocity Control

3.1. Abstract

This chapter presents a continuous-flow polymerase chain reaction (PCR) microchip with a serpentine microchannel of varying widths for regional velocity control. By varying the channel width, it was possible to optimize the exposure time of the sample to each temperature while minimizing the transitional times between temperature zones. A semi-analytical heat transfer model and finite element analysis (FEA) were employed to investigate the thermal characteristics of the microchip. The results from the finite element simulation and the theoretical model were compared with measurement obtained from an infrared camera. The premeditated geometry of the microchannel was optimized by performing a fluid-flow analysis using finite element method. By optimizing channel geometry, we were able to prevent flow separation within the channel and to avoid bubble formation. The flow fields were also studied using micro particle image velocimetry (μ-PIV). Successful amplification of 90 bp DNA fragment was achieved.

3.2. Introduction

The polymerase chain reaction (PCR) is a tool used to amplify a specific gene or region of DNA between two known flanking sequences. Its applications range from diagnosis of infectious disease to analysis of specific gene mutations that occur in a variety of genetic disorders. Since its development in the 1980s, PCR has become one of the most useful and versatile methodologies applied to molecular biological applications [1]. PCR consists of the following three-phase cycle: denaturation, annealing and extension. In the denaturation phase, double stranded DNA templates (dsDNA) separate into single strand at temperatures from 90 to 95 °C. Denaturation is accomplished by rupturing the hydrogen bonds between the bases of each monolithic strand. After denaturation, the temperatures are reduced to 50 to 65 °C at which short oligonucleotide primers hybridize to the flanking sequences of each single stranded template molecule (ssDNA). The sequence of the primers exactly complements the sequence of the flanking region of the original DNA template. Primer hybridization to the wrong sequence on the template results in undesirable nonspecific amplification. Additionally, annealing of the primers together, coined primer-dimer formation is also a form of nonspecific amplification that should be avoided. Problems with nonspecific amplification and low product yield result from long transitional times between the optimal temperatures of each phase and by unnecessarily extended exposure times to the high denaturation temperature. During the final phase of PCR, the temperature is increased to 70-75 °C and Taq polymerase enzyme extends the primers by attaching deoxyribonucleoside triphosphates (dNTPs) from solution. In contrast to denaturation and hybridization which occur almost instantly, the length of the extension phase is restricted by the 100 nucleotide per second extension rate of Taq enzyme. Thus, from a chemical point of view, the time limiting factor for the reaction is the extension phase [2].

The way at which the three specific temperatures are implemented in PCR is very important for high product yields and specificity. For the bench-top PCR thermal cycler, the total cycling time usually takes several hours. Approximately 80% of this time accounts for transitional periods between the optimal temperatures of each phase. These extended transitional periods often result in reduced product yields and unspecific amplification. In combination with large heating blocks that have large thermal masses which significantly inhibit heating and cooling rates, the product yield and specificity are often poor and insufficient. Additionally, large initial sample volume requirements and cumbersome dimensions characteristic of most macroscopic thermal cyclers restrict PCR to use in the laboratory [3]. In the past decade, microfabrication technology has led to the development of a variety of high-throughout miniature PCR devices. PCR microdevices have two basic platforms. The most common platform involves etched microchambers that host immobilized (stationary) samples. Amplification is achieved by temperature cycling with heaters in contact with the substrate [4, 5, 6, 7]. The reaction chamber is most commonly fabricated in silicon by anisotropic wet etching. The thermal cycling is performed by an on-chip polysilicon microheater. The other platform is based on the continuous-flow format where the sample is spatially cycled through three well-defined temperature zones [8-14]. The temperature zones are created by extraneous heating blocks, integrated heaters deposited by well-established thin-film technologies [8-11], or by small external heaters bonded to the microchip by an adhesive [13, 14]. Since the optimum reaction temperatures and exposure times are key to successful DNA amplification, thermal/fluid control of the DNA sample in the chip is a critical issue for

PCR microchip design [15]. Typical problems associated with current flow-through microchip-based PCR devices include: (a) undesirable heat-transfer between temperature zones due to the limited spacing between heaters, (b) failure to maintain uniform temperatures in each temperature zone, and (c) unnecessary extended transitional times. Although efforts have been made to improve the thermal characteristics of continuous-flow microchips [9, 15], design for better thermal/fluid control has not yet been explored.

In this chapter, a continuous-flow PCR microchip with regional velocity control is presented. By varying the channel widths in the different temperature zones of the microchip, the flow velocities throughout the channel could be adjusted to limit the transitional times between reaction zones. A semi-analytical heat transfer model and finite element analysis (FEA) were employed to investigate the thermal characteristics of the PCR microchip. Results were compared with temperature measurements from an infrared camera. Micro particle image velocimetry (μ-PIV) was used to visualize the flow-fields within the microchannel. Successful amplification of 90 bp DNA fragment was achieved.

3.3. The Design of the PCR Microchip with Regional Velocity Control

To design a continuous-flow PCR microchip, the following aspects must be taken into consideration: the selection of materials, the number of cycles to be processed, the dimensions of the microchannel, the length ratios per cycle of the microchannel in each temperature zone, the geometry and position of the heaters, and the local position of the temperature sensors. Polymers have been extensively used for biomedical microdevices since they are cheap and biocompatible [5, 7, 12]. However, because most polymers are highly permeable to gases, they are usually insufficient for use in PCR microchips, in particular continuous-flow PCR microdevice. A high permeability to gases often causes the formation of bubbles within the microchannel leading to large temperature gradients within the DNA mixture [7]. Silicon and glass are the most popular materials for BioMEMS since well-established integrated circuit (IC) and microfabrication tools are readily available. However, the high thermal conductivity of silicon makes it difficult to maintain discrete temperature zones, and its opaque optical characteristics restrict real-time fluorescence detection. In the contrary, glass is an excellent choice for PCR microchips because it can be easily treated to reduce protein absorption and transparent to visible light for possible real-time fluorescence detection [16]. Additionally, the low thermoconductivity of glass makes it easy to maintain uniform temperature zones within relatively small area.

The geometry and arrangement of the serpentine microchannel with respect to the three temperature zones is very important. The velocity of the sample in a channel of constant cross-sectional area is constant in both the transitional zones and the temperature zones. This unnecessarily results in extended denaturation, hybridization, and transitional periods that degrades enzyme activity and produces non-specific amplification. To eliminate these extended periods, the width of the microchannel was made variable throughout the length of the channel by sets of transitional nozzles and diffusers. Smaller channel widths were established in the transitional zones so that the sample would flow at a higher velocity and transitional times would be reduced. To avoid flow separation and bubble formation, the dimensions were planned very carefully. In accordance to changes in the microchannel, the spacing between the heaters was optimized to limit thermal cross-talk.

Fabricating microchannels in glass substrates poses many difficulties. Over-etching with hydrofluoric acid (HF) is a very common problem since the over-etching ratio can be as high as 5:1. It was found that a large over-etching ratio is a result of poor adhesion between the etching mask and the glass substrate. To resolve the over-etching problem, a possible solution is to deposit an amorphous silicon thin-film on glass, which served as the etching mask, by low pressure chemical vapor deposition (LPCVD) method. Amorphous silicon offered excellent critical dimension control [17].

We have designed a novel continuous-flow PCR microchip, constructed from borosilicate glass, with a serpentine microchannel of variable width (coined variable channel). An illustration of the device is shown in Figure 3.1a and 3.1b. The chip is capable of performing 20 PCR cycles with flow rates from 0.5 to 5 μl/min. The depth of the channel is constant at 30 μm, so the cross-sectional area is controlled by the width. The time ratio of the temperature zones is 1:2:4 for denaturation, hybridization, and extension, respectively. The widths for denaturation, hybridization, and extension, are 100 μm, 273 μm, and 340 μm, respectively. The channel width in the transition zones is 10 μm. In addition to the normal reaction cycles, an initial extended denaturation cycle and an extended post-extension cycle were appended (not shown in Fig 3.1a). Copper bars and thin-film heaters were utilized to establish the three-temperature zones.

Temperature sensors were bonded to the copper bars using a thermally conductive epoxy for temperature feedback.

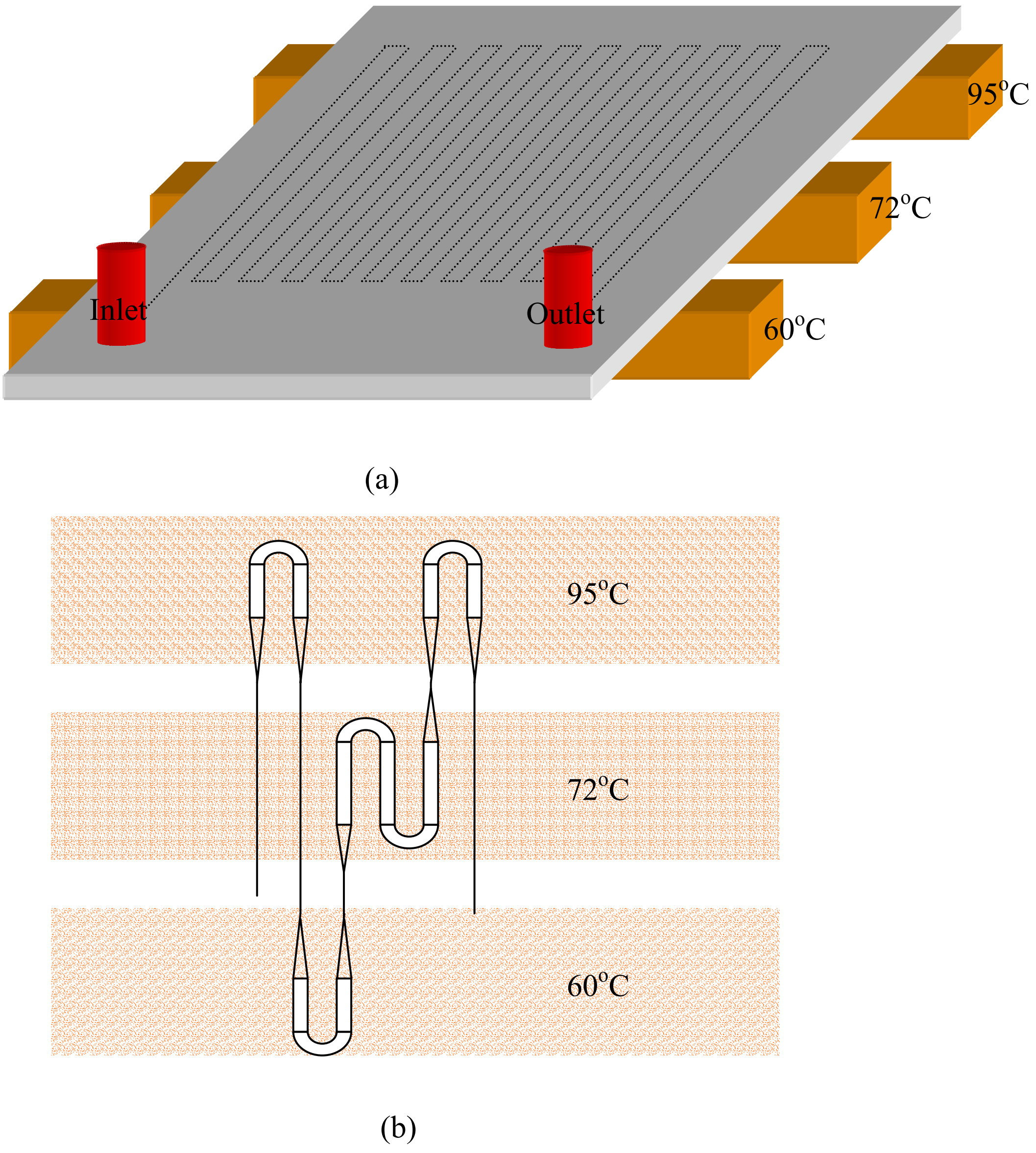

Figure 3.1: (a) Schematics of a 20-cycle, continuous-flow PCR microchip with regional velocity control, (b) the concept of variable width channel (shown for one cycle).

3.4. Modeling and Analysis of a PCR Glass Microchip

A heat transfer analysis of the microchip was carried out using a finite element method (FEM). In addition, a semi-analytical heat transfer model was developed to visualize the temperature distribution within the chip. The analytical and simulation results were compared with infrared temperature measurements.

3.4.1. Finite Element Analysis of Heat Transfer inside PCR Chip

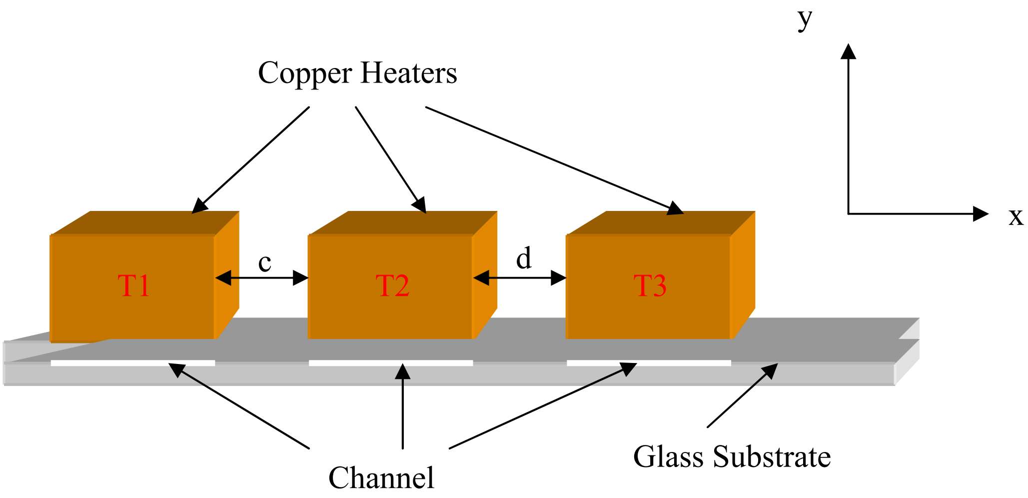

Figure 3.2: Configuration of three copper heaters attached to glass surface.

Table 3.1: Material properties for thermal analysis

Materials	Thermal conductivity (W/mK)	Convection heat transfer coefficient (W/m^2K)
Glass	1.13	7.5 (with air)

ANSYS 5.6 software was employed for the thermal analysis of microchip. Pertinent material properties incorporated into the simulation are listed in Table 3.1. The configuration of three copper heaters on the surface of glass substrate is in Figure 3.2. For a thin glass wafer (about 500 µm thick), the temperature of the heater is close to the temperature of the microchannel. Therefore, the temperature uniformity of the microchannels is mostly determined by that of the heaters, which was realized by the use of copper blocks of high thermal conductivity (thermal conductivity = ~ 400W/mK). According to Fourier's law of heat conduction, when the heat flux in the y direction is zero there is no temperature change normal to that direction, so after the points, there is no heat coming from the glass substrate underneath the heater to heat up the heater. Then, the temperature uniformity underneath the heater is determined by the temperature uniformity of the heater.

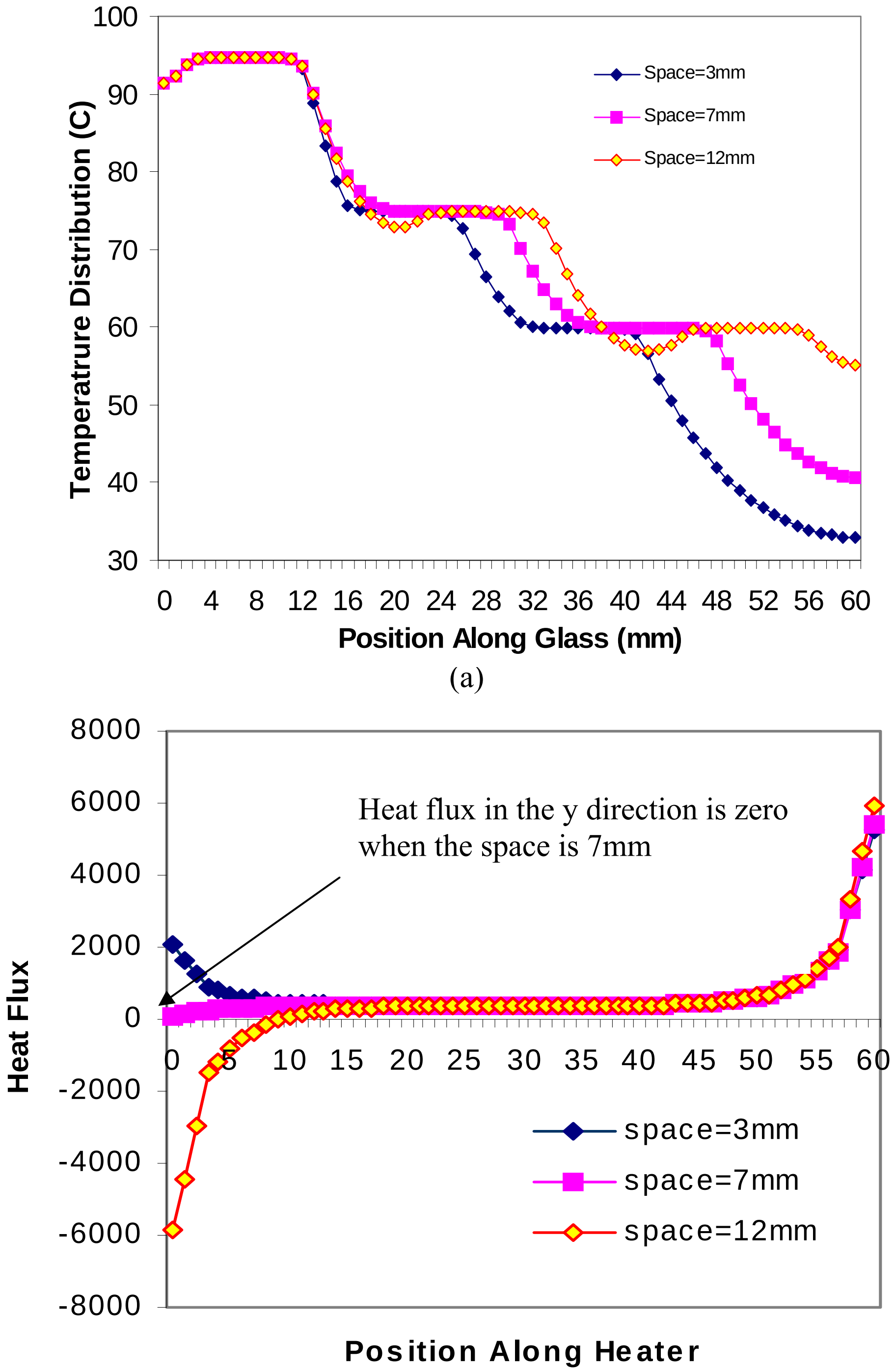

(a)

(b)

Figure 3.3: (a) Temperature distribution along the glass in the heater sequence of 90 °C – 75 °C – 60 °C, (b) heat flux at different heater spacing of 3 mm, 7 mm, and 12 mm.

To optimize the spacing between the heaters, we investigated heater spacing of 3, 7, and 12 mm. The temperature distribution along the centerline of the glass is shown in Figure 3.3a. The small 3 mm spacing resulted in unwanted heat conduction to the lower temperature. Additionally, it was difficult to maintain uniform temperature distribution underneath the heaters. Larger spaces improve temperature uniformity but simultaneously increase the absolute size of the microchip. Unnecessarily large heater spacing also increases transition times. Using the zero heat flux normal to the y-direction directly at the leading edge of the heater as our selection criteria, we found the optimum heater spacing c is 7.0mm and d is 7.2mm (Figure 3.3b).

3.4.2. Analytical Analysis of Heat Transfer inside a PCR Chip

Convective heat transfer from the sides of the PCR chip is neglected due to the small exposed surface area and temperature differences relative to the environment. The heat flux and temperature at infinity in x direction are assumed to be zero and room temperature, respectively. Based on these assumptions, a semi-analytical model was created to study heat transfer within the chip. The analytical model was first devised by dividing each heater into m equal components in order to study heat flux inside heaters. w_p b_q, h_q denote the width of the pth element heater, thickness of the qth layer, and interfacial positioning, respectively. The PCR structure is shown in Fig. 3.4.

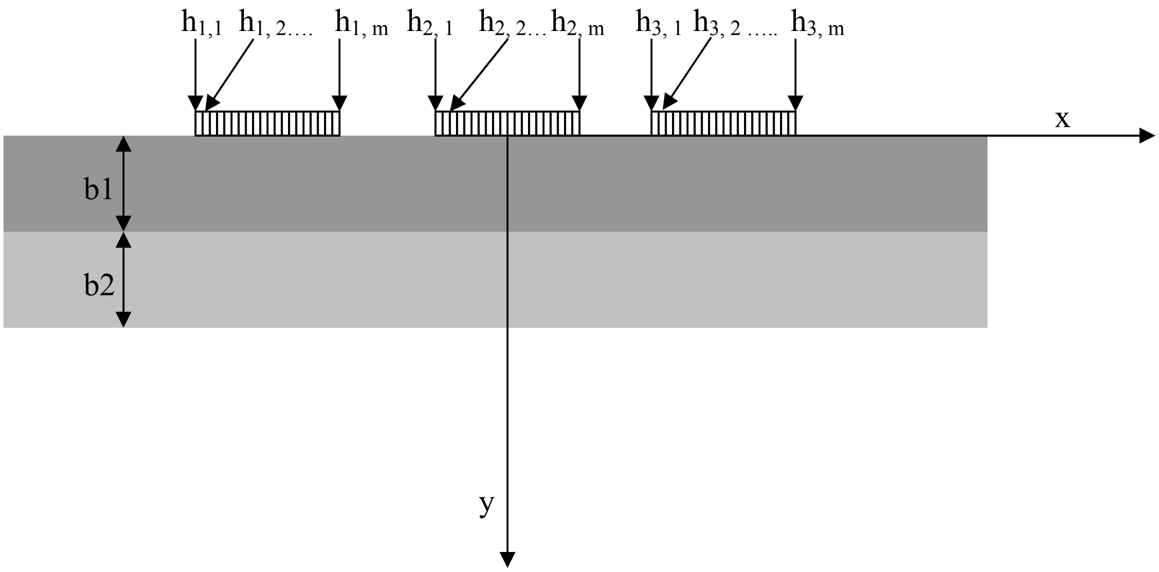

Figure 3.4: The coordinate system of the thermal model for PCR microchip.

The steady-state heat conduction equation for the top glass layer (T_1) and the bottom glass layer (T_2) is as follows:

$$\frac{\partial^2 T_q}{\partial x^2} + \frac{\partial^2 T_q}{\partial {y_q}^2} = 0 \tag{3.1}$$

where the subscript q represents the qth glass layer referenced from the top.

On the surface (y = 0), we have

$$-k_1 \frac{\partial T_1}{\partial y}\Big|_{y=0} = -h_t(T_1 - T_\infty) + \frac{Q_p}{w_p} \text{ for the } pth \text{ element heater and}$$

$$-k_1 \frac{\partial T_1}{\partial y}\Big|_{y=0} = -h_t(T_1 - T_\infty) \text{ for other regions} \tag{3.2}$$

If we define a heat flux function $f(x) = \begin{cases} \dfrac{\mathrm{Q_p}}{\mathrm{w_p}} & \text{(for the pth element heater)} \\ 0 & \text{(for other regions)} \end{cases}$, (3.2) can be rewritten as

$$-k_1 \frac{\partial T_1}{\partial y}\Big|_{y=0} = -h_t (T_1 - T_\infty) + f(x) \qquad (3.3)$$

where Q_p is the input power per unit length, w_p is width of the element heater; h_1 is the convective heat transfer coefficient (we ignore the variation of h_1 on the surface due to its small area).

The boundary condition at the interface is

$$k_1 \frac{\partial T_1}{\partial y}\Big|_{y=h_1} = k_2 \frac{\partial T_2}{\partial y}\Big|_{y=h_1} = h_{eff}\,\Big|_{y=h_1} (T_2 - T_1)\Big|_{y=h_1} \qquad (3.4)$$

where h_{eff} is the equivalent heat transfer coefficient between two layers. Without any contact thermal resistance, h_{eff} approaches infinity and the temperature at the interface is continuous. If this is the case, Eq. (3.4) becomes

$$k_1 \frac{\partial T_1}{\partial y}\Big|_{y=h_1} = k_2 \frac{\partial T_2}{\partial y}\Big|_{y=h_1}, T_1\Big|_{y=h_1} = T_2\Big|_{y=h_1} \qquad (3.5)$$

At the bottom of the PCR chip, we have

$$-k_2 \frac{\partial T_2}{\partial y}\Big|_{y=h_2} = h_t'(T_2 - T_\infty) \qquad (3.6)$$

We finally find the temperature T_1 in the first layer as

$$T_1(x, y_1) - T_\infty = \frac{1}{2\pi} \int_{-\infty}^{+\infty} \frac{F(\lambda)}{h_t \zeta_1 - k_1 \lambda} [\sinh(\lambda y_1) + \zeta_1 \cosh(\lambda y_1)] e^{i\lambda x} d\lambda \qquad (3.7)$$

Noticing that the term $\frac{\sinh(\lambda y_1)+\zeta_1\cosh(\lambda y_1)}{h_t\zeta_1 - k_1\lambda}$ is an even function of λ since the parameter ratio ζ_1 is odd function of λ [see Appendix A], we can simplify Eq. (3.7) to

$$T_1(x,y_1)-T_\infty = \frac{1}{\pi}\int_0^{+\infty}\frac{\sinh(\lambda y_1)+\zeta_1\cosh(\lambda y_1)}{h_t\zeta_1 - k_1\lambda}\mathrm{Re}[F(\lambda)e^{i\lambda x}]d\lambda \tag{3.8}$$

where $F(\lambda)=\sum_{p=1}^{m}\frac{Q_p}{w_p}\frac{\exp(-i\lambda x_{p,2})-\exp(-i\lambda x_{p,1})}{-i\lambda}$ for heaters with a constant heat flux and $\lim_{\lambda\to 0}F(\lambda)=\sum_{p=1}^{m}Q_p$

The temperature on the top surface of the second layer can then be obtained as

$$\begin{aligned} &T_2(x,y_2=0)-T_\infty \\ &=\frac{1}{2\pi}\int_{-\infty}^{+\infty}\frac{F(\lambda)}{h_t\zeta_1-k_1\lambda}[\sinh(\lambda b_1)+\zeta_1\cosh(\lambda b_1)]e^{i\lambda x}d\lambda \\ &=\frac{1}{\pi}\int_0^{+\infty}\frac{1}{h_t\zeta_1-k_1\lambda}[\sinh(\lambda b_1)+\zeta_1\cosh(\lambda b_1)]\mathrm{Re}[F(\lambda)e^{i\lambda x}]d\lambda \end{aligned} \tag{3.9}$$

A more detailed derivation is shown in [18]. This semi-analytical model conveniently gives temperature data and heat flux information at every position. Following the same criteria using in finite element analysis, the heat fluxes at the leading edges are zero as Equation 3.10 and 3.11

$$\frac{\partial Q_{2,1}}{\partial t}=0 \tag{3.10}$$

$$\frac{\partial Q_{3,1}}{\partial t}=0 \tag{3.11}$$

The optimal spaces c and d are found as 7.0 mm and 7.2 mm respectively, which is the same as the value that we found from the finite element analysis. Also, the temperature profile in the microchannel is in excellent agreement with those from the finite element analysis (Figure 3.5a). The discrepancy at the edge is due to infinite boundary assumption. The vertical heat flux (y-dir.) is also in agreement with the results from finite element analysis (Figure 3.5b, c, and d).

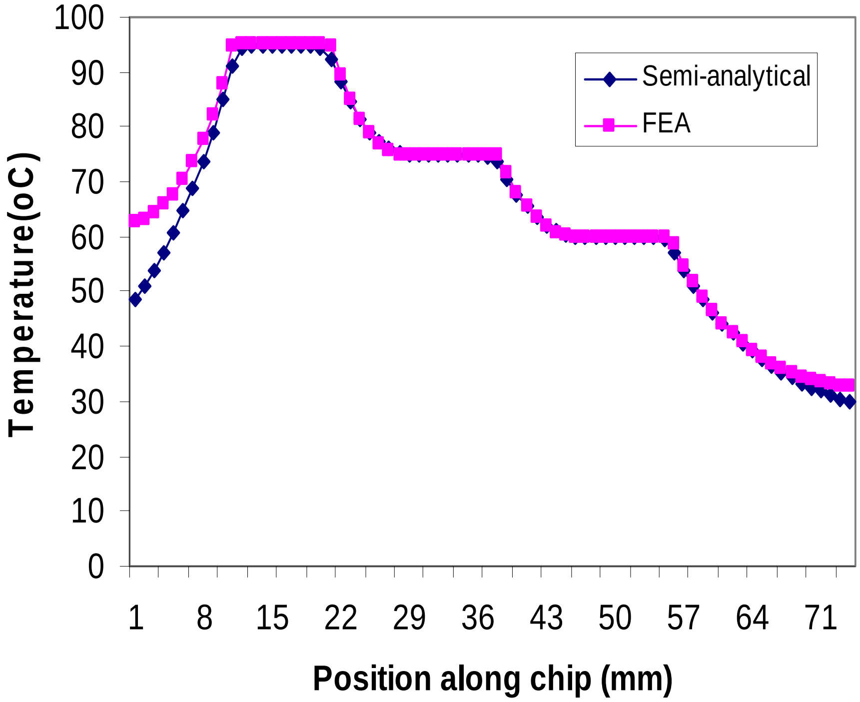

(a)

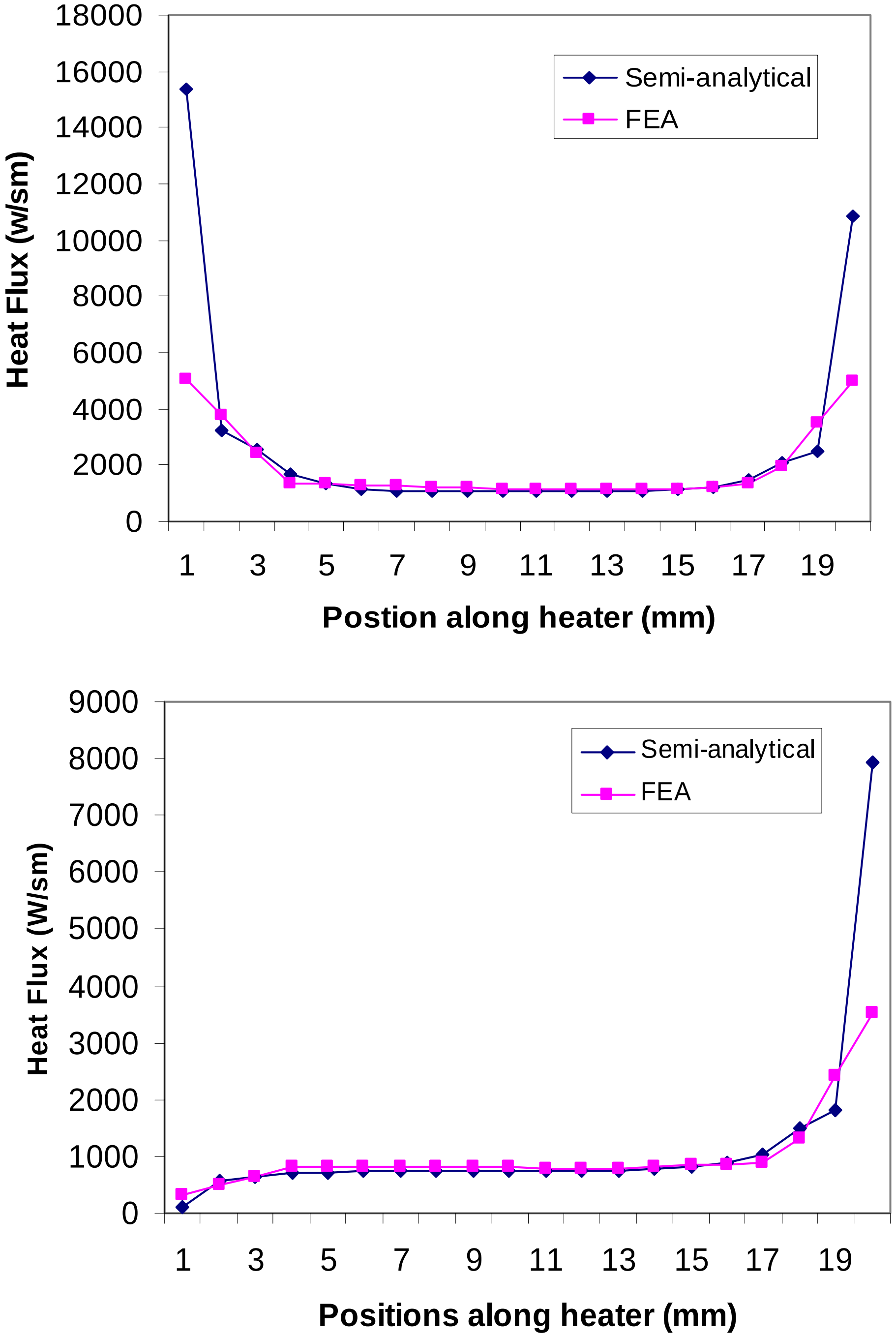
18000
16000
14000
12000
10000
8000
6000
4000
2000
0
Heat Flux (w/sm)
1
3
5
7
9
11
13
15
17
19
Postion along heater (mm)
Semi-analytical
FEA
9000
8000
7000
6000
5000
4000
3000
2000
1000
0
Heat Flux (W/sm)
1
3
5
7
9
11
13
15
17
19
Positions along heater (mm)
Semi-analytical
FEA

(c)

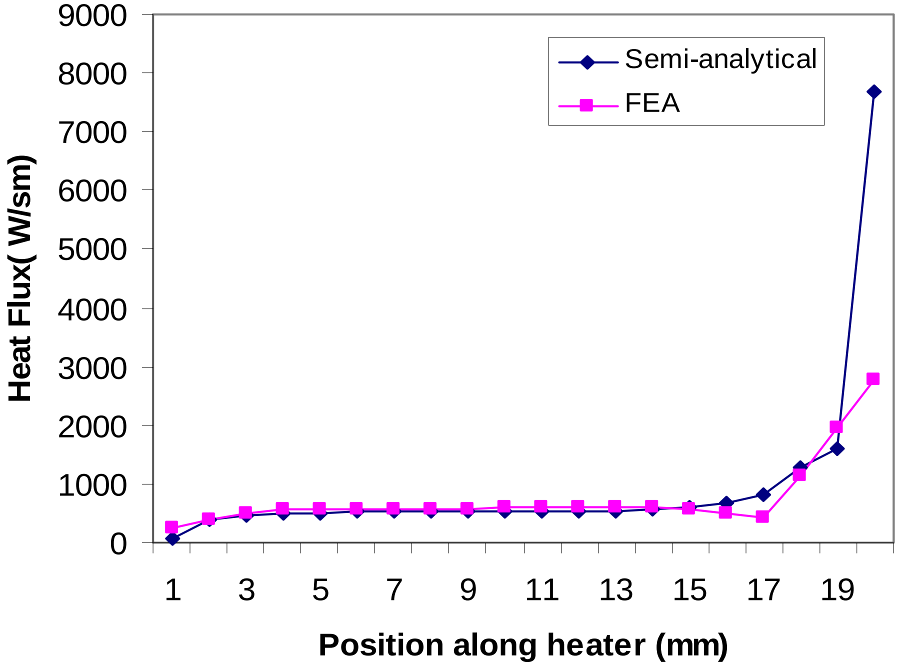

(d)

Figure 3.5 (a) Temperature profiles at the microchannel from the analytical equations and finite element analysis and 95 ^{o}C (b), 75 ^{o}C (c) and 60 ^{o}C (d) heaters heat flux from the analytical equations and finite element analysis

3.4.3. Simulation of Fluid Flow inside a PCR Chip

It was hypothesized that having a variable channel would potentially cause bubble problems within the microchannel [9]. Bubbles, caused by flow separation, induce temperature gradients within the sample significantly reducing amplification efficiency. Additionally, flow separation causes mixing of the buffer solution and PCR sample.

Therefore, flow separation should be avoided. From a fluid mechanics point of view, flow separation results from the angles of the transitional nozzle and diffuser-like channel retractions and expansions. When the angles are small, flow separation is limited. The finite element analysis (ANSYS) was used to find the angle of the nozzle and the diffuser to limit flow separation at the targeted flow rates. The flow inside the microchannel was laminar when the angle was 7 degrees. Figure 3.6 is the laminar flow inside a 7 ^{o} diffuser (a) and a 7 ^{o} nozzle (b).

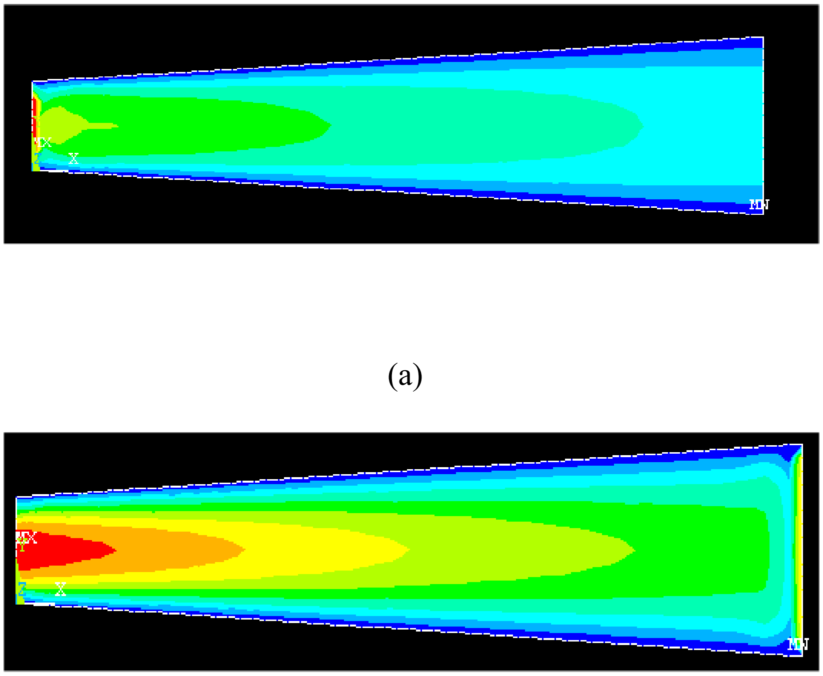

(a)

(b)

Figure 3.6: Laminar flow within (a) a 7 ^{o} diffuser and (b) a 7 ^{o} nozzle at the target flow rate

3.5. Fabrication and Instrumentation of PCR Chip

The PCR chip fabrication process started with depositing a thin layer of amorphous silicon (100 nm) on a 4” polished borosilicate glass wafer. Hydrofluoric acid (HF) was used to etch the microchannels in the glass substrate to a depth of 30 μm using the amorphous silicon layer as a mask. The amorphous silicon was subsequently stripped by etching with CH_4 RIE. On another glass wafer, three holes of 1.0 mm diameter were drilled by powder blasting. These holes were used as the inlet and outlet for the DNA sample and buffer solution. The wafer with the holes was fusion bonded to the wafer with the serpentine microchannel. After thermal fusion bonding, the wafer was diced into single glass chips. Nanoport assemblies (UpChurch, WA, USA) were bonded to the glass chips to provide access to the channel. Prior to bonding, the nanoport assemblies were cleaned using isopropyl alcohol (IPA). The chip was cleaned in Piranha solution for 10 minutes. After cleaning, a biocompatible epoxy ring was used to attach the nanoports. Alignment with the holes on the chip was achieved using a glass capillary of 0.8 mm diameter. Adhesion was enhanced by a clamp used to hold down the nanoport during curing. After baking for 20 min at 170^{o}C, the epoxy was completely dry and the nanoport was tightly bonded to the chip (Figure 4.7a and b).

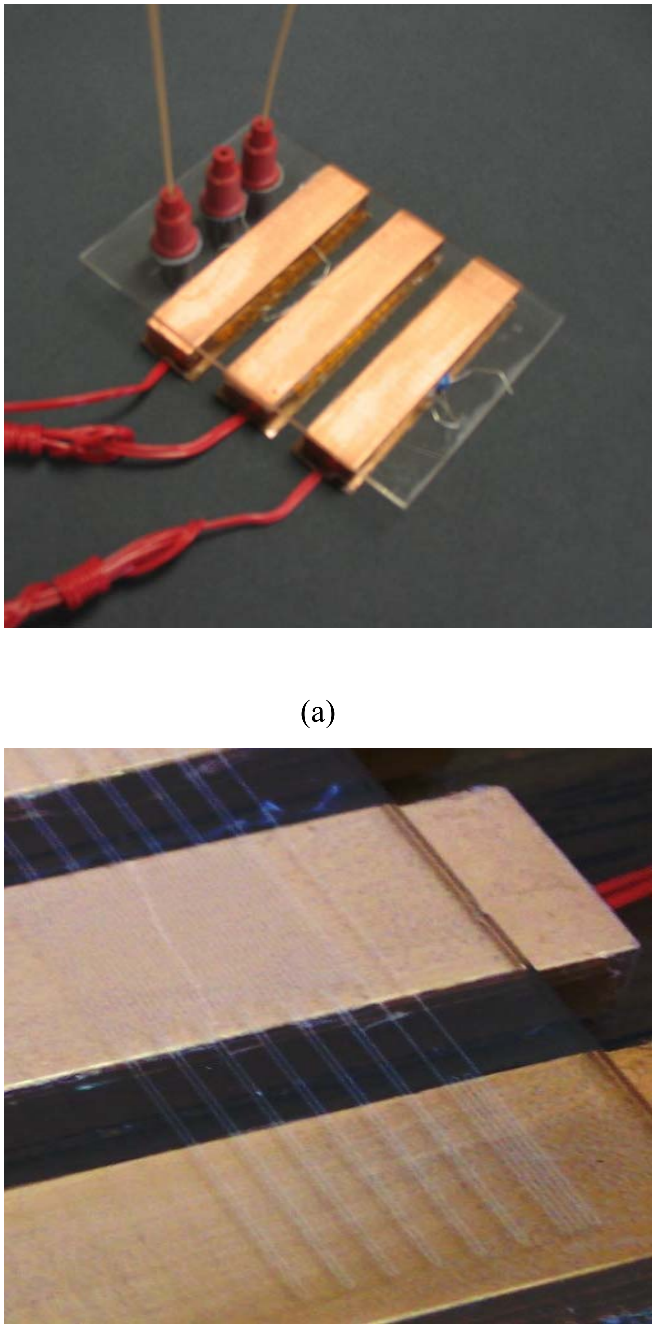

(a)

(b)

Figure 3.7: (a) the finally assembled 20-cycle PCR glass microchip and (b) a close-up view of the microchannel on copper heaters.

From previous experiments, a temperature variation of approximate 6 ^{o}C was found on the integrated Cr/Au (20 nm / 200 nm) metal thin-film heaters of 4 mm width. Therefore, we used copper blocks to provide a uniform stable temperature inside the microchannel since the copper blocks have a large thermal capacity and a high thermal conductivity. Three copper blocks, measuring 10 × 40 × 6 mm each, and thin-film heaters (HK5160R157L12, Minco, MN) were bonded to specific positions on the glass using thermal epoxy (PSA # 10, Minco, MN). Additionally, three temperature sensors (S245PD12245, Minco, MN) were attached to the copper blocks for temperature feedback. Three digital PID (proportional, integral, and derivative) temperature controllers (CA16A2010-9502, Minco, MN) and a homemade conditioning circuit were connected to the heaters and sensors to control the temperatures of the three copper blocks individually. A DC power supply (EH382213, Davis Infotek Instruments, MD) was used to provide power to the heaters and the PID controllers. The temperature tolerance was about 0.1 ^{o}C. Figure 3.8a is PCR experiment setup and Figure 3.8b shows the configuration of the temperature control system.

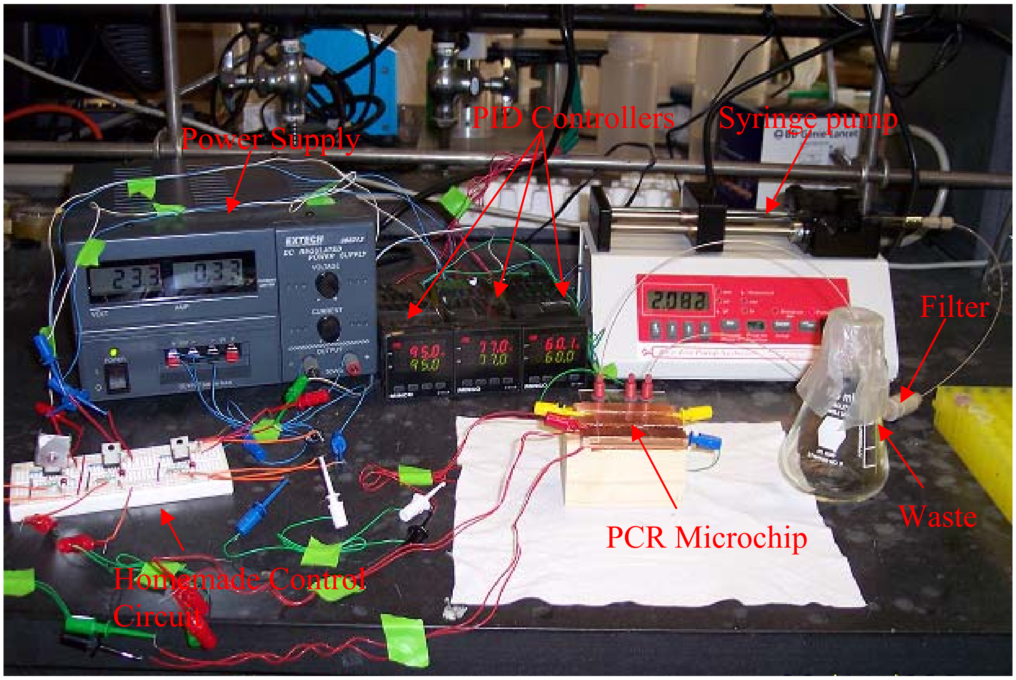
Power Supply
PID Controllers
Syringe pump
Filter
Waste
PCR Microchip
Homemade Control Circuit

(a)

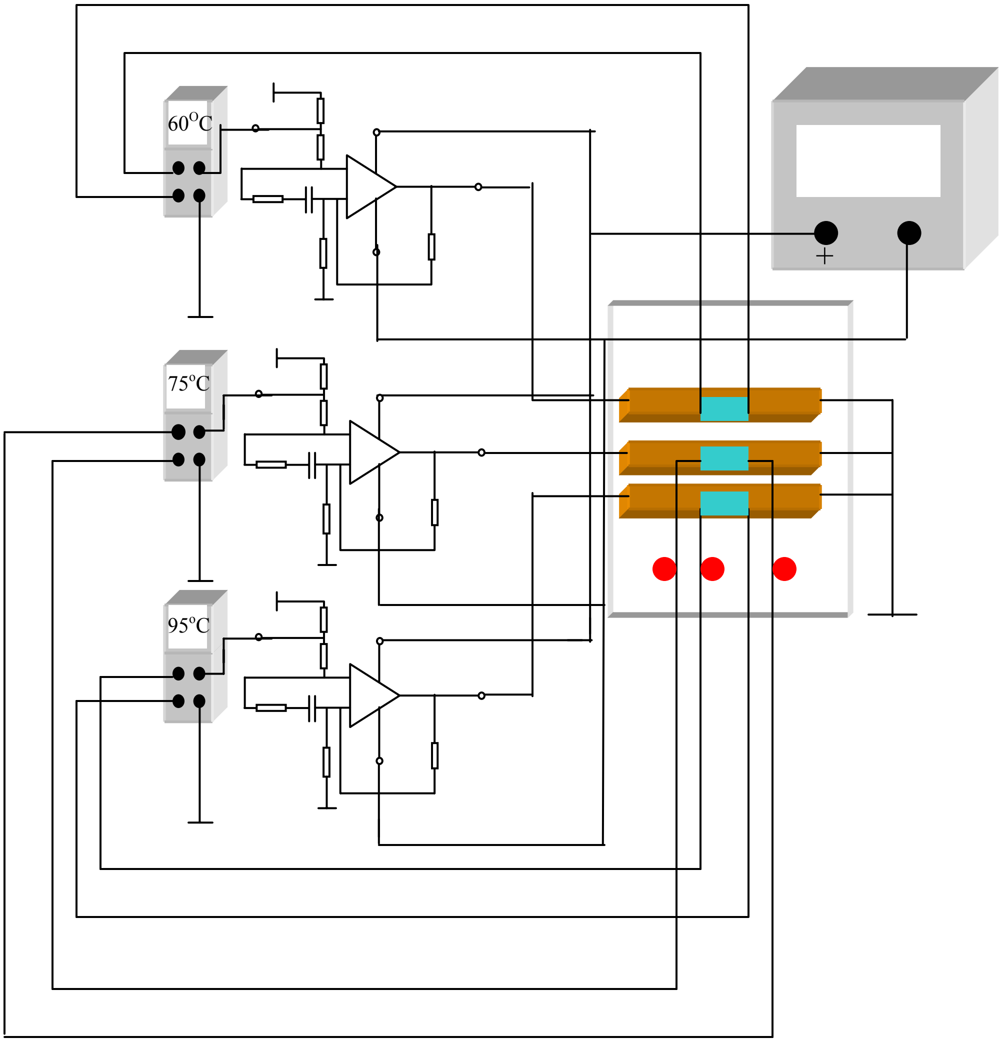

(b)

Figure 3.8: (a) The PCR experimental setup and (b) the configuration of the temperature control system

3.6. Experimental Results and Discussion

3.6.1. Temperature Measurement

The temperature distribution within the microchannel is very important to the reaction. Unfortunately, it is difficult to measure temperatures inside the channel using the conventional thermocouples. Therefore, the surface temperature was measured and used as a reference. Since the temperature difference between the channel and the surface was determined to be less than 1 ^{o}C, the temperature in the microchannel could be calculated. The small temperature difference resulted from the thin (500 μm) glass substrate.

An infrared (IR) camera was used to measure the surface temperature distribution. The IR camera was calibrated to compensate the effects of the environment before any measurements were taken. After the temperature readings stabilized, the surface emissivity was measured using a supermeter (OMEGA, USA) for temperature data. The surface temperature distribution was plotted in Figure 3.9a. The experimentally measured temperature distribution was compared with the temperature from the semi-analytical equation and finite element simulation (Figure 3.9b). The differences between the IR measurements and the results from the semi-analytical equation were most prominent at the sides of the glass chip. We believe this discrepancy is a result of the infinite boundary condition assumed in the semi-analytical equation. Nevertheless, for other regions which are more important for the PCR chip, the semi-analytical equation provides an excellent estimation of the chip temperature.

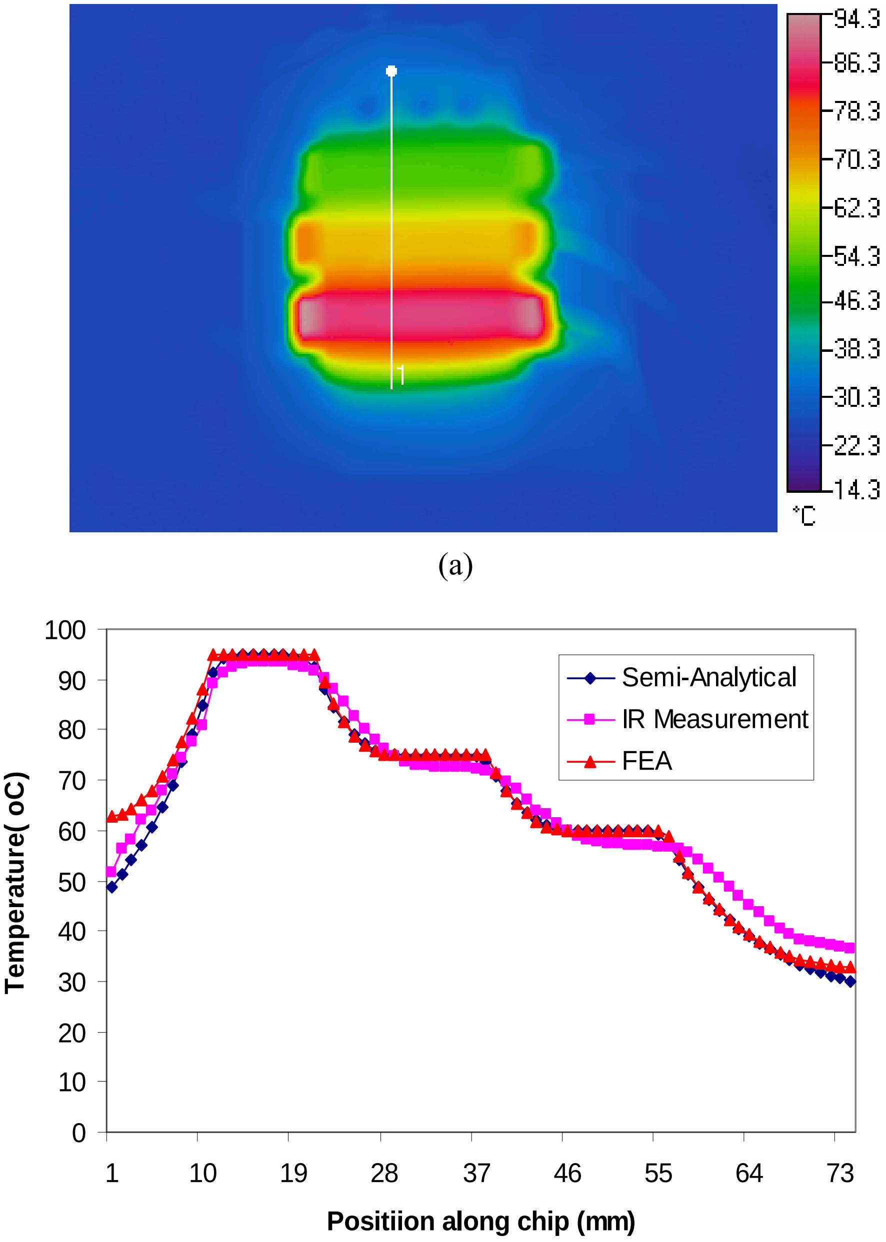

(a)

(b)

Figure 3.9: (a) IR picture for the temperature distribution on the PCR surface and (b) comparison of temperatures from the semi-analytical equation, finite element simulation and experiment measurement.

3.6.2. μ-PIV Velocity Measurement

The flow separation caused air bubbles that disrupted the continuity of the flow and instilled temperature gradients inside the microchannel reducing amplification efficiency. In order to limit flow separation, the dimensions of the expansions and contractions of the microchannel walls were optimally designed using finite element analysis tools. Micro particle image velocimetry (μ-PIV) was employed to measure the velocity field inside the microchannel [19, 20].

To conduct μ-PIV, the microchip was initially positioned on the stage of an optical microscope. Fluorescent beads of 0.9 μm diameter were suspended in DI water and flushed through the microchannel by a syringe pump. A 532 nm Nd: YAG laser was passed through a mirror, band filter to remove futile wavelengths, and a beam expander to increase the beam diameter. The expanded laser beam was sent through another mirror and objective lens which was focused on the middle plane of the microchannel. A Charged Couple Device (CCD) camera captured the reflected fluorescence image. The image was then processed by PIV software. Figure 3.10 shows the μ-PIV experimental setup in Prof. M. Olson's group at Iowa State University where the μ-PIV measurement was carried out.

To reduce the amount of uncertainty associated with the experiment, 100 images were obtained, summarized, and averaged to return a velocity profile inside the microchannel. Flow rates of 1 μl/min and 5 μl/min were used for the μ-PIV experiments. Velocity measurements were retrieved at 16 locations along a single cycle. The measurements taken for the individual cycle were representative of the flow field in the entire microchannel. The locations of the images are shown in Figure 3.11.

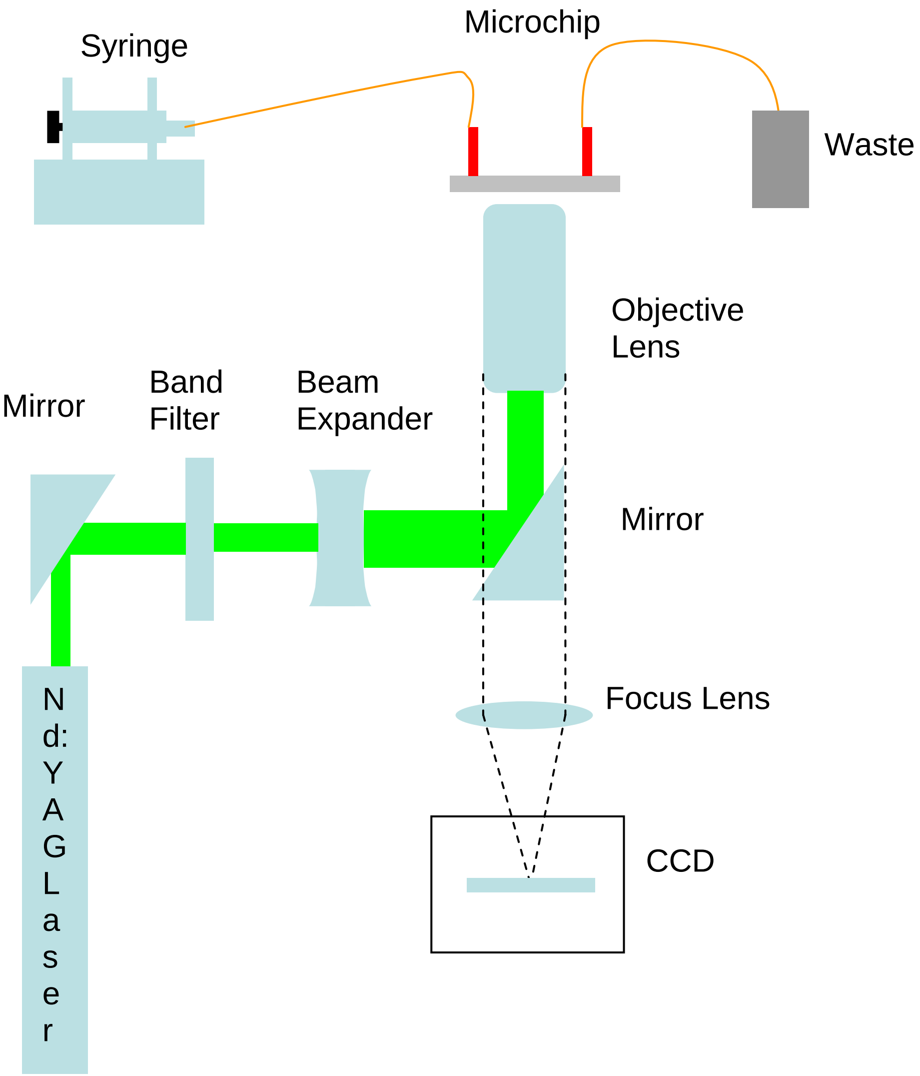

Figure 3.10: Micro-PIV experimental setup.

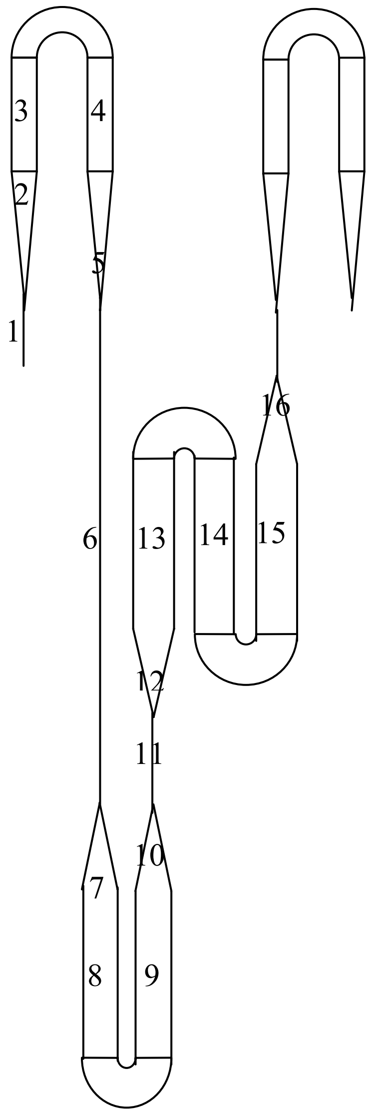

Figure 3.11: PIV measurement positions within one thermal cycle.

From the fluid mechanic point of view, flow separation is frequently visualized at positions where the velocity is the fastest or from the outlets of the nozzle-contractions and diffuser-expansions [21]. The remaining text in the chapter discusses the μ-PIV measurements imaged at the positions where flow separation may occurr. Figure 3.12a shows the μ-PIV image taken at position 1 where the velocity of the fluid was the fastest. Figure 3.12 (b) and (c) are images taken at the outlet locations after the channel contractions and expansions. Figure 3.13 shows that the velocities in the three temperature zones and the exposure time ratios of three temperature zones is, indeed, 1:2:4 as was planned.

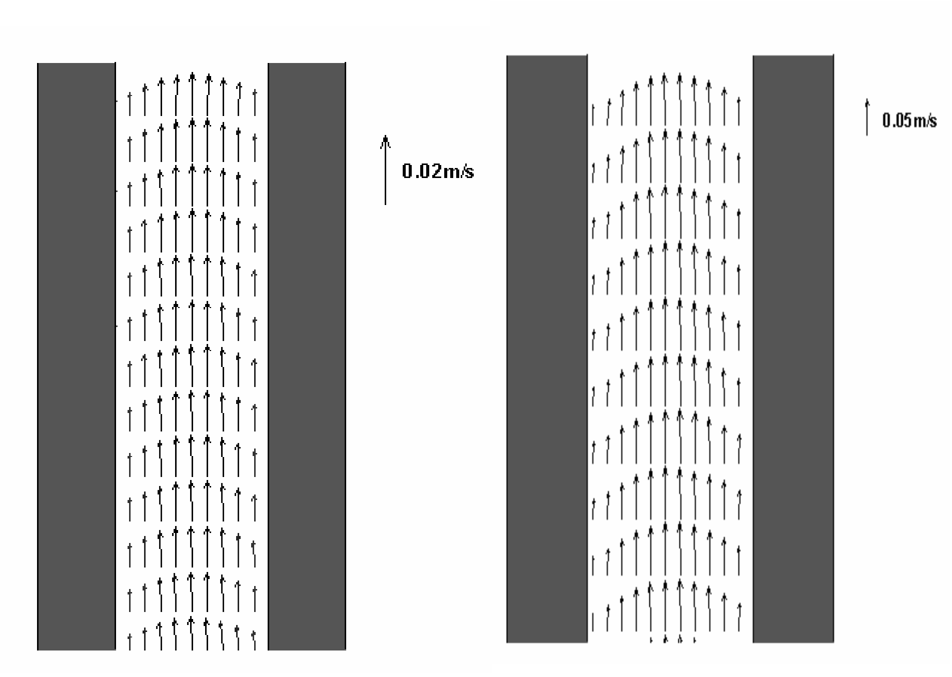

(a)

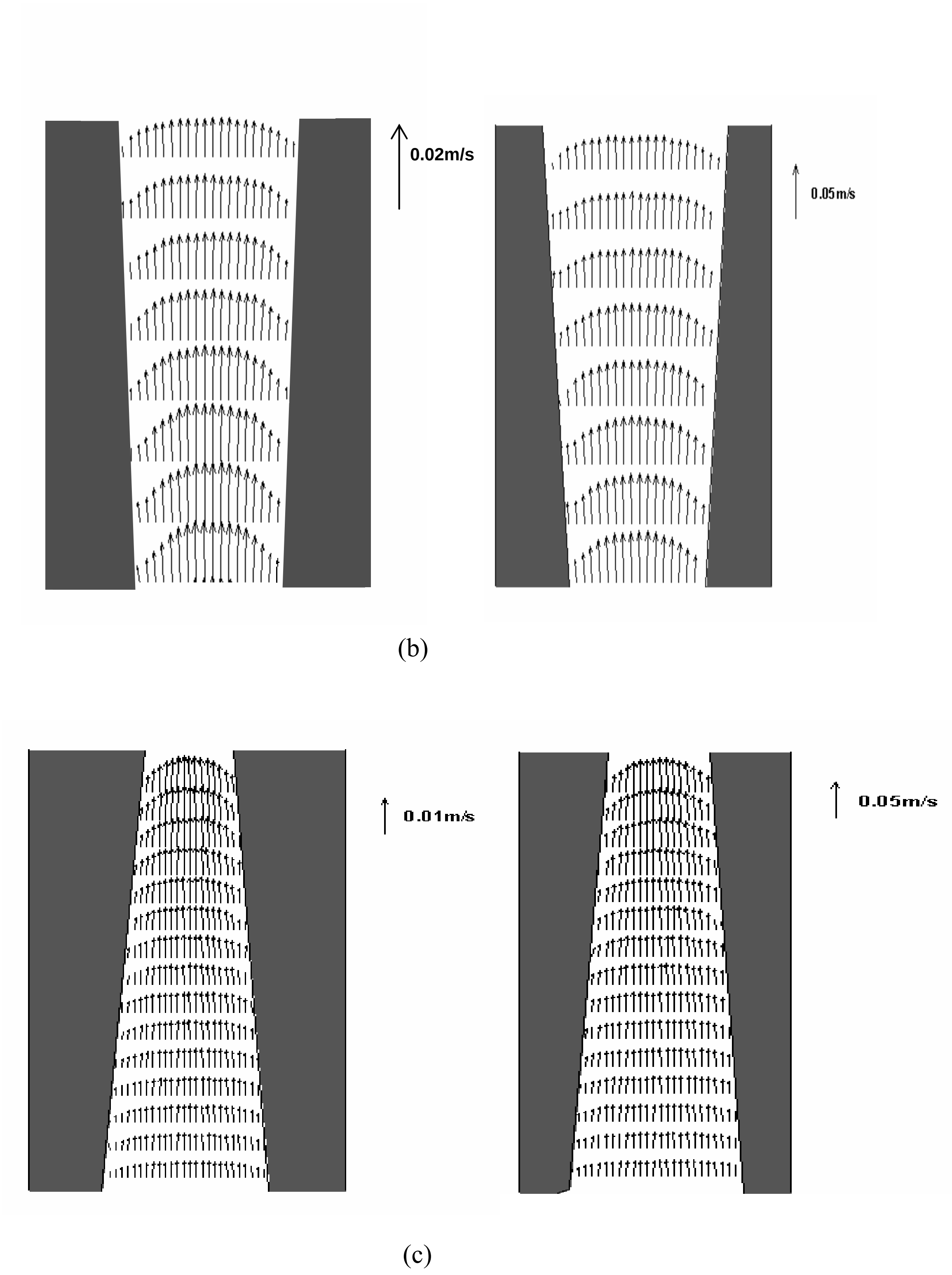

Figure 3.12: μ-PIV measurements taken at (a) position 1, (b) position 2, and (c) position 5 at the flow rates of 1 μl/min and 5 μl/min.

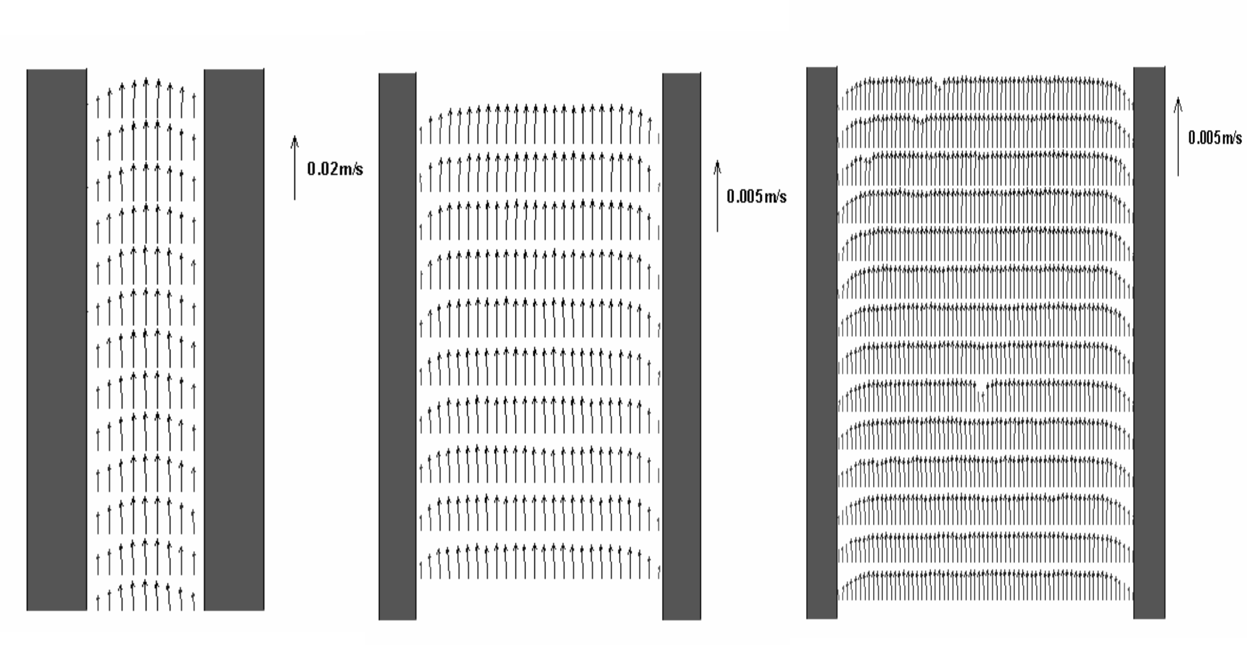

(a) (b) (c)

Figure 3.13: μ-PIV measurement taken at (a) position 3, (b) position 8, and (c) position 13.

3.6.3. PCR Amplification Experiment

A 100 μl gastight syringe (Hamilton Company, UK) was connected to a programmable syringe pump (Ne-1000, New Era Pump System, NY). The syringe pump was connected to the PCR chip using PEEK tubing (UpChurch, WA). In order to avoid channel blockage, an in-line 0.5 μm microfilter (UpChurch, WA) was connected before the glass chip to remove particulate residuals inside the solution. The 90bp *bacillus anthracis* sequence (from Sterne) strain was used to test the PCR chip. The upstream DNA primer was 5’AATCTTCCGCAATGGACG3’ and the downstream primer was 5’TTCTTCCCTAACAACAGAG3’. SigmaCote (Sigma, USA), a silane agent, was used to silanize the inner wall of the microchannel. The silanization prevented the absorption of Taq enzyme into the contacting channel walls. Initially, deionized (DI) water and ethanol were flushed through the microchannel at a flow rate of 10 μL/min for 2-3 times. Then, the SigmaCote was pumped through the microchannel at a flow rate of 1 μL/min. After the glass surfaces were silanized to prevent the DNA inhibition by absorption, ethanol was pumped through to push excess saline out of the microchannel and then DI water washes the channel for 2-3 times at a flow rate of 10 μL/min. Following the initial surface-treatment and subsequent wash with ethanol and DI water, the temperature control system was turned on and allowed to stabilize. After temperature stabilization, a buffer solution was pumped through the chip at a flow rate of 1 μL/min to prime the channel. Finally, the PCR mixture was pumped through the microchannel at a flow rate of 1 μL/min and the amplified product was collected from the outlet in aliquots and placed in small vials for further analysis using slab-gel electrophoresis. A negative control was run without enzyme to make sure that the amplified product was specific. Figure 3.14 shows the results from the gel.

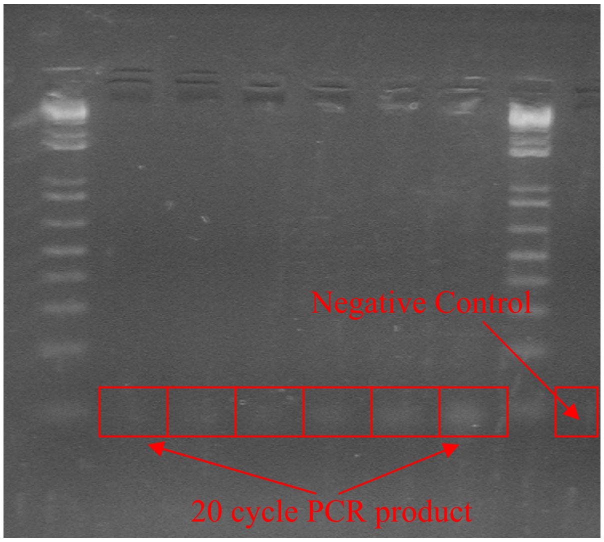

Figure 3. 14: A gel electrophoresis picture of the 20-cycle PCR product.

3.7. Conclusions

We have developed a continuous-flow polymerase chain reaction (PCR) microchip from borosilicate glass wafers with a variable channel for DNA amplification. Varying channel widths adjusted the local velocities at different positions. The dimensions were optimized to limit the transitional times between temperature zones and provide optimal exposure of the sample to the various temperatures. A semi-analytical heat transfer model and FEA was developed to visualize the temperature distribution inside the microchip and to optimize channel dimensions and the spacing between the heaters. Infrared temperature measurements showed good temperature uniformity at each temperature zone and agreed with results from the semi-analytical equation and the FEA.

μ-PIV was utilized to visualize the velocity field inside the microchannel at different locations. Measurements were taken for flow rates of 1-5 μl/min. Successful amplification of 90 bp DNA fragment was achieved with high heating and cooling rates.

3.8. References

1. Mullis K. B., Ferre F., Gibbs R. A., 1994, *The Polymerase Chain Reaction*, Birkauser, Boston
2. Wittwer C. T., Ririe K. M., Andrew R. V., David D. A., Gundry R. A., and Balis U. J., 1997, *Biotechniques*, 22, 176-181
3. http://www.idahotec.com/
4. Lin Y. C., Huang M. Y., Young K. C., Chang T. T., and Wu C.Y., 2000, *Sensors and Actuators B*, 71, 2-8
5. Hong J. W., Fujii T., Seki M., Yamamoto T., and Endo I., 2001, *Electrophoresis*, 22, 328-333
6. Lagally E. T., Emrich C. A., and Mathies R. A., 2001, *Lab on a chip*, 1, 102-107
7. Shin Y. S., Cho K. C., Lim S. H., Chung S., Park S. J., Chung C., Han D. C., and Chang J. K., 2003, *Journal of Micromechanics and Microengineering*, 13, 768-774
8. Sun K., Yamaguchi A., Ishida Y., Matsuo S. and Misawa H., 2002, *Sensors and Actuators B,* 1-7
9. Schneegab I., and Kohler J. M., 2001, *Reviews in Molecular Biotechnology*, 82, 101-121

10. Schneegab I., Brautigam R., and Kohler J. M., 2001, *Lab on a chip*, 1, 42-49

11. Chou C. F., Changrani R., Roberts P., Sadler D., Burdon J., Zenhausern F., Lin S., Mulholland A., Swami N., and Terbrueggen R., *Microelectronic Engineering*, 2002, 61-62, 921-925

12. Liu J., Enzelberger M., and Quake S., 2002, *Electrophoresis*, 1531-1536

13. Kopp M. U., Mello A. J. de, and Manz A.,, 1998, *Science*, 280, 1046-1048

14. Obeid P. J., Chirstopoulos T. K., Cratree H. J., and Backhouse C. J., 2003, *Analytical Chemistry*, 75, 288-295

15. Yong D. S., Lee Y. S., Cho H. J., Sung S. W., Oh K. W., Cha J. H., and Lim G. B., 2002, *Journal of Micromechanics and Microengineering*, 12, 813-823

16. Obeid P. J., Chirstopoulos T. K., 2003, *Analytica Chimica Acta,* 494,1-9

17. Simpson P.C., Wooley A. T., Mathies R. A., 1998, *Biomedical Microdevices*, 1, 7-26

18. Hao Q., 2004, *Journal of Micromechanics and Microengineering,* 14, 914-926

19. Li H., et al, 2004, *Journal of Microelectromechanical Systems*, in press

20. Meihart, C. D. Wereley S. T., and Santiago J. G., 1999, *Experiments in Fluids*, 27, 414-419

21. Panton R., 2003, *Incompressible Flow*, John Willey & Sons, Inc

Chapter 4: Polydimethylsiloxane Interconnects for Microfluidic System Applications

4.1. Abstract

This chapter presents novel Polydimethylsiloxane (PDMS) based interconnects for microfluidics systems with a low dead volume. Through-hole type and "┌" type PDMS interconnects have been designed, fabricated and tested for glass and plastic capillary tubing. Oxygen reactive ion etching (RIE) and epoxy bonding methods are employed to bond PDMS interconnects to various substrate materials including silicon, glass, polymer and other thin film materials. Leakage pressure, leakage rate and pull-out force are characterized for these interconnects. For reusable PDMS interconnects, the maximum leakage pressure reaches 510 kPa (75 psi) and the maximum pull-out force is about 800 mN. For non-reusable PDMS interconnects, the maximum leakage pressure is found to be 683 kPa (100 psi) and the maximum pull-out force is 2 N. For both types of PDMS interconnects, the leakage rate test demonstrates that the leakage is not detectable at a working pressure of 137 kPa (20 psi).

4.2. Introduction

Due to the difficulties in fabricating monolithic microfluidic systems, interconnects are becoming more and more important in integrated microfluidic systems that may involve micropumps, microvalves, micromixers, or microchannels. Interconnects are also imperative to bridge a microfluidic component to its macro-environment. Gonzalez et al. fabricated a modular type coupler that used deep reactive ion etching [1]. Yao et al. developed a reusable silicone rubber coupler for microfluidic interconnection. After several times of use, the silicone coupler still has a similar performance [2]. Wijngaart et al. directly melted polyethylene capillary tubes on the silicon substrate and then applied epoxy to reinforce the tubing [3]. Armani et al. developed polydimethylsioxane (PDMS) based pressure-fit-type interconnects with molding [4]. Puntambekar and Ahn fabricated a self-aligning fluidic interconnect. Due to its self-aligning nature, this interconnect has a significant reduction of dead volume and pressure drop [5]. Gray et al. developed several novel interconnects for micro-fluidic systems. These interconnects can be easily assembled [6]. Tsai and Lin presented a method to insert Mylar into a micro-to-macro interconnection discretely and integrally [7]. Recently, Pattekar and Kothare melted plastic tubing and applied epoxy to achieve high performance interconnects [8].

PDMS is receiving increasing interest in the field of micro-electro-mechanical systems (MEMS) [9-11]. Many PDMS-related micro and nano-fabrication techniques have been developed [9]. Unlike traditional materials such as silicon and glass used in MEMS, PDMS is a low cost material. Moreover, microfabrication processes for PDMS are simple and rapid compared to traditional etching and bonding approaches in MEMS. The primary advantages of PDMS material for microfluidic applications include ease of bonding, optical transparency (from 230 nm to 700 nm wavelength) for precise alignment, softness for molding, and biocompatibility in a biological environment. Moreover, one can bond PDMS to different materials reversibly and irreversibly. These materials include conventional microfludic substrates such as silicon and glass, thin films like SiO_2 and Si_xN_y, and polymer substrates such as polystyrene and PDMS.

This chapter reports new PDMS-based interconnects for microfluidic system applications. Through-hole type and "┌" type PDMS interconnects for glass and plastic capillary tubing are designed, fabricated, and tested. We investigate bonding PDMS interconnect to different substrate materials such as glass, silicon, and polymer, as well as thin films including SiO_2 and Si_xN_y using oxygen reactive ion etching (RIE) bonding and epoxy bonding. The maximum leakage pressure, leakage rate, and pull-out force are measured for PDMS interconnects.

4.3. Design and Fabrication Processes

Two types of PDMS interconnects were designed as shown in Figure 4.1: through-hole and "┌" type, used for both plastic tubing and glass tubing.

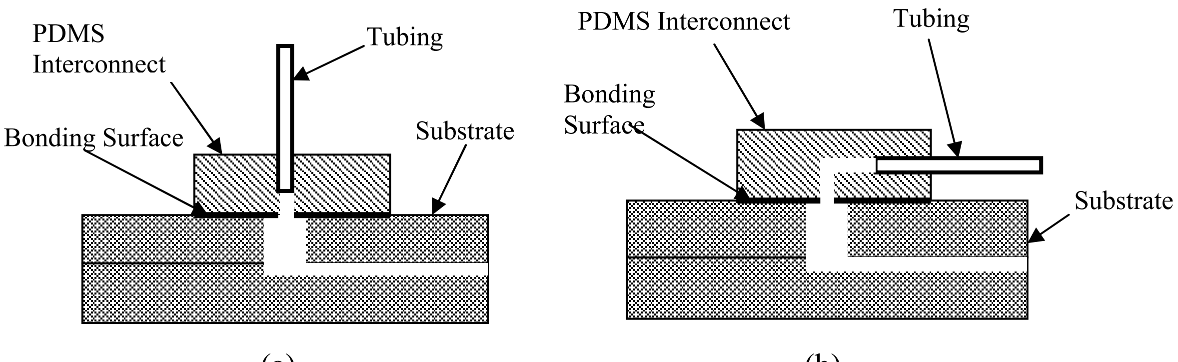

(a)

(b)

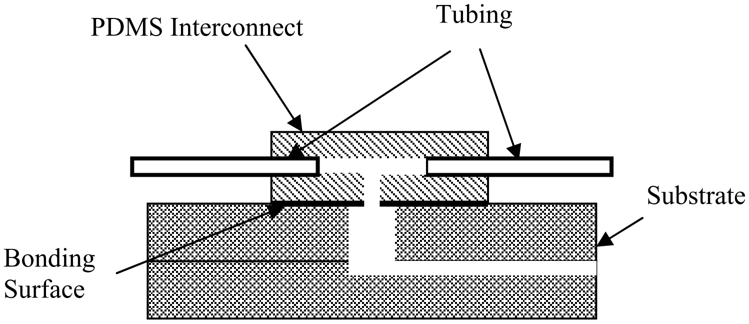

(c)

Figure 4.1: Schematic of PDMS interconnects: (a) through-hole type, (b) " ┌" type, and (c) multiple-channel type.

To fabricate these interconnects, a curing agent and PDMS prepolymer (SYLGARD 184 Silicone Elastomer Kit, Dow Corning, Midland, MI) in a 1:10 weight ratio were thoroughly mixed. Then the prepolymer mixture was degassed in a 20-25 mmHg vacuum chamber for one hour to remove air bubbles in the mixture and to ensure complete mixing between the two components. A thin carbon film was deposited on a 4" polished silicon wafer using reactive ion etching (RIE). The parameters for RIE deposition are 100 W, 100 sccn CHF_3 and 1.5 minutes. After placing a plastic ring (diameter =100 mm, thickness = 3 mm) on the silicon wafer, the prepolymer mixture of 10 ml was poured onto the silicon wafer and covered with a transparency film to prevent any bubble formation at the interface. While the plastic ring holding the prepolymer, the extra prepolymer was removed using a plastic blade. The entire stack was then cured for 1 hour at 145 ^{o}C on a hot plate. After curing, the PDMS layer was peeled off from the silicon substrate. The thickness of the PDMS layer is approximately 3 mm.

The PDMS layer was then cut into squares of 4 mm x 4 mm with a blade. A glass capillary (O.D. 0.84 mm and I.D. 0.60 mm, Vitrocom. Inc, NY) was used to punch connecting holes in the PDMS squares. We found punching the hole is critical for PDMS interconnects as PDMS is a soft material with Young's Modulus of 700-800 kPa, which is much less than that of silicon or glass. If punched improperly, the holes will not be circular as shown in Figure 4.2a. A non-circular interconnecting hole can not hold the capillary at a high pressure. In order to get circular holes, one has to punch the PDMS square slightly at first using the capillary tube and then slowly rotate the tube until the glass tube is punched through the PDMS square (Figure 4.2b)

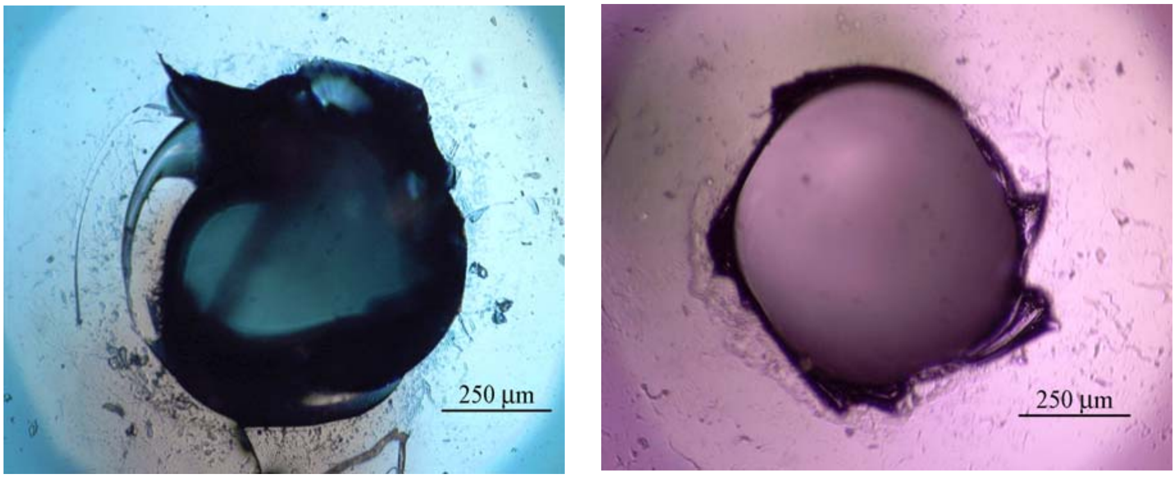

Figure 4.2: (a) Optical picture for the non-circular hole punched with OD 0.84mm glass capillary. (b) Optical picture for circular hole punched with OD 0.84mm glass capillary.

For the "┌" type PDMS interconnect, we have developed a two-step curing method (Figure 4.3). The prepolymer mixture was prepared following the aforementioned method. A thin carbon layer was deposited on the silicon mold using reactive ion etching (RIE) to allow easier removal of PDMS the layer after curing. In order to make a PDMS layer with a certain thickness, we used a plastic ring of known thickness to assist the fabrication process. In this work, a plastic ring (diameter = 100 mm and thickness = 5 mm) was placed on the silicon wafer to hold the PDMS prepolymer. The prepolymer mixture of 10 ml was poured into this plastic ring, forming a uniform prepolymer layer of about 1.5 mm thick due to surface tension. After 5 minutes curing at 100 ^{o}C on a hot plate, the metal pins (diameter = 800 μm) were positioned on the PDMS layer and then another 10-20 ml prepolymer mixture was poured to fill the whole ring. Extra prepolymer was scraped from the plastic ring using a plastic blade. The PDMS was then cured for 1 hour at 100 ^{o}C on the hot plate. The final thickness of the PDMS layer is approximately 5 mm. After removing the metal pins, the PDMS layer were cut into pieces of 4 mm by 4 mm. Holes of 1.5 mm in diameter were punched in the PDMS using a 1.5 mm glass capillary to connect the channels inside the PDMS layer.

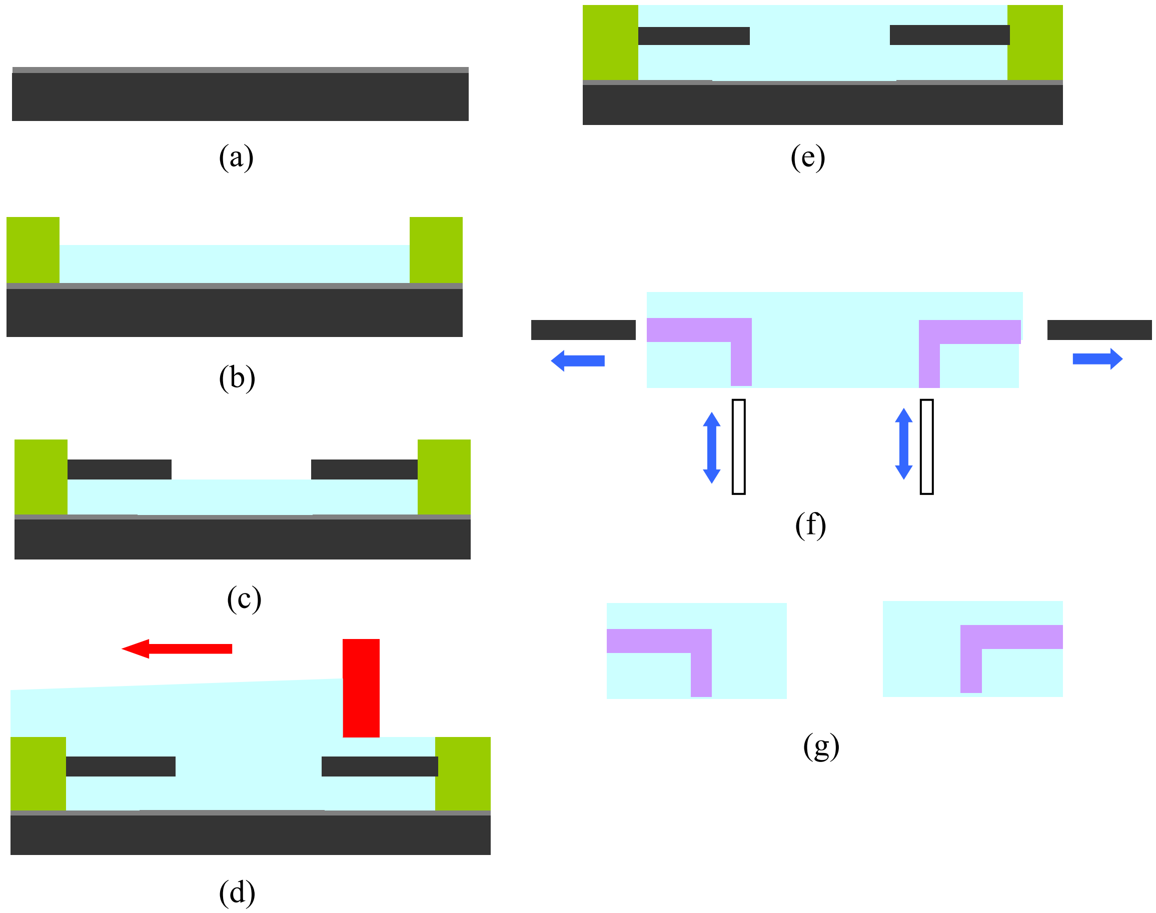

Figure 4.3: The fabrication processes of the “┌” type PDMS interconnect using a two-step curing method: (a) carbon thin film deposition, (b) first prepolymer injection, (c) metal pins positioning, (d) second prepolymer injection, extra prepolymer removal, (e) 1 hr curing, (f) metal pin removal and hole punching, (g) interconnect cutting.

After punching the hole, the substrate and PDMS interconnect were put into a petri dish for ultrasonic cleaning using de-ionized (DI) water and isopropyl alcohol for 5 minutes. This is to ensure a clean surface for follow-up bonding. The petri dish was then put into a baking oven for 30 minutes at 90 °C to remove the residual water molecules, followed by oxygen plasma surface activation in a Plasma Thermo RIE system. The working parameters of the RIE were set as 70 W at 75 mtorr with an oxygen flow rate of 20 sccm and 15 seconds etching time. After activation, PDMS interconnects were bonded onto the substrate immediately and put on a hot plate for 30 minutes at 145 °C in order to enhance bonding strength. If precise alignment is necessary, isopropyl alcohol could be used to avoid immediate bonding. The alignment can be controlled with a reasonable accuracy (less than 50 μm) since PDMS is transparent in the UV and visible ranges [10]. In Figure 4.4, through-hole type PDMS interconnects were successfully bonded onto a glass substrate (Fig 4.4a and 4.4b) and “┌” type PDMS interconnects were bonded onto a PDMS substrate (Fig 4.4c).

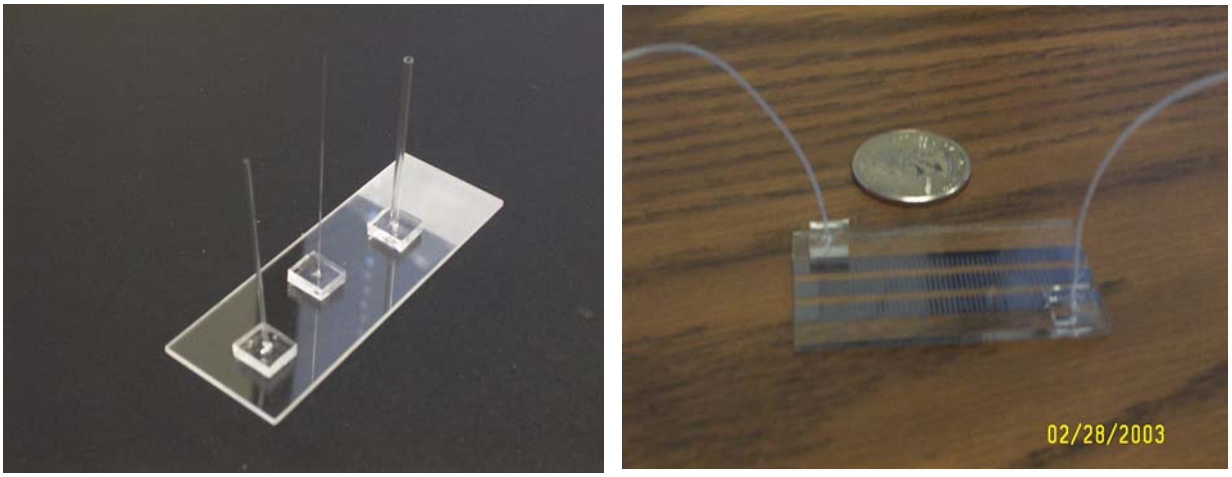

(a) (b)

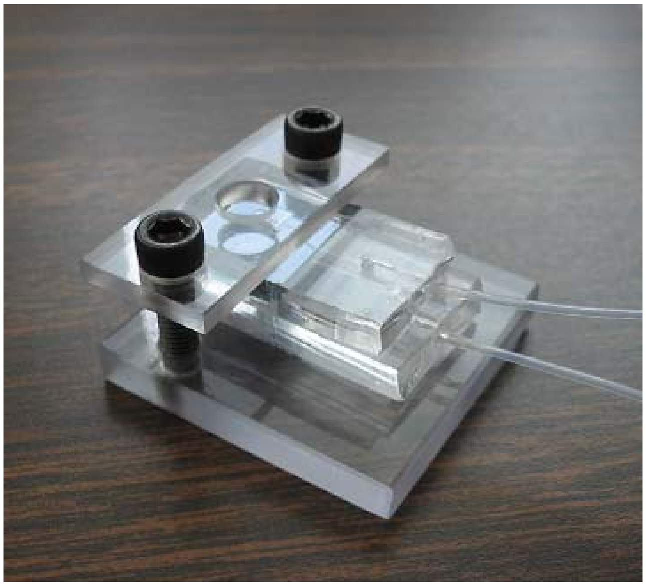

(c)

Figure 4.4: Through-hole type PDMS interconnect bonded to a glass substrate for glass capillary tube (a), for plastic capillary tubing (b), and "┌" type PDMS interconnect bonded to a PDMS substrate (c).

In some cases, using oxygen plasma to activate the surface as mentioned previously may not be compatible with the device fabrication process since some critical dimensions could be changed due to plasma etching. A possible solution to such a case is to use UV or thermally curable epoxy to bond PDMS interconnects onto the substrate as shown in Figure 4.5.

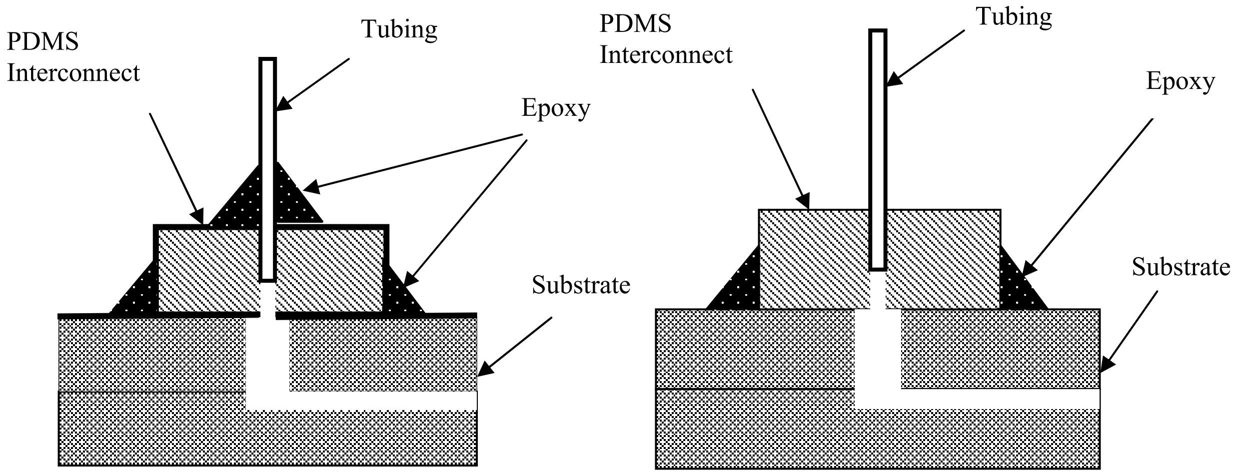

Figure 4.5: Schematic for (a) epoxy glued non-reusable PDMS interconnect and (b) reusable PDMS interconnect.

Following the previous processes, PDMS squares (4 mm × 4 mm) were punched and then cleaned to keep the bonding surfaces particle and dust free. The substrate and PDMS interconnects were baked for 30 minutes at 90 ^{o}C to dry out the bonding surfaces. After that, PDMS squares and the substrate were bonded together. But this bonding is reversible. In order to stand a high pressure during device operation, UV or thermally curable epoxy was used to reinforce the PDMS interconnect to the substrate as illustrated in Figure 4.5. In this work, UV curable DYMAX epoxy (DYMAX 1186-M series, DYMAX Corporation) was used to seal the interconnect. After 20-minute UV curing on the aligner, the epoxy glued PDMS interconnect to the substrate. Although this bonding is reversible, we found that there is no epoxy seeping to block the holes and channels during curing (Figure 4.6). For precise alignment of the interconnect, we used isopropyl alcohol to spray the bonding surfaces in order to avoid immediate bonding during alignment. Then the entire stack was put on a hot plate to dry out the isopropyl alcohol for reversible bonding.

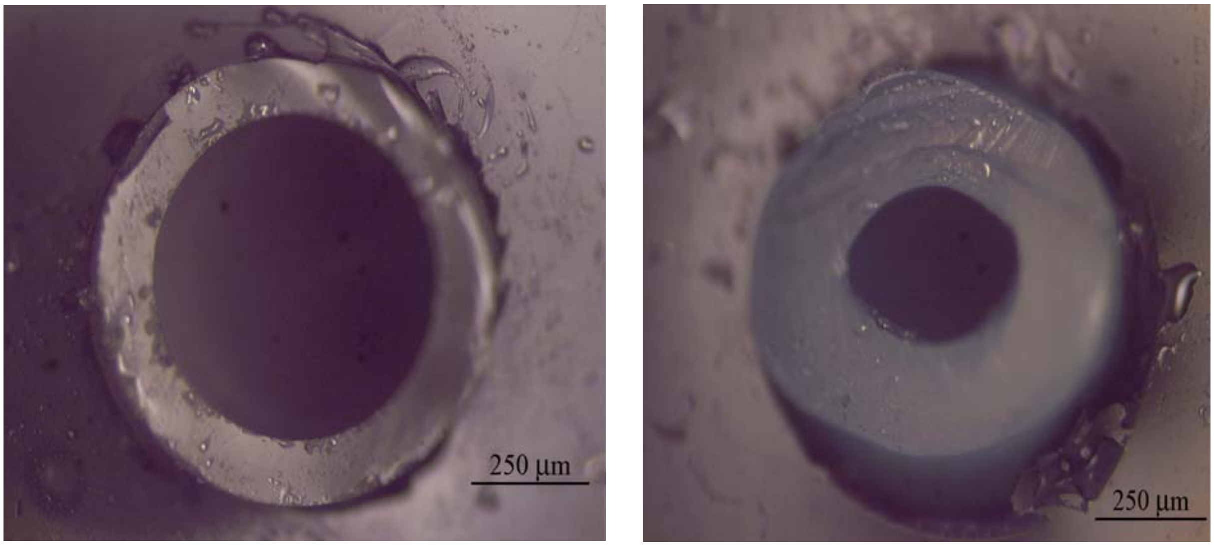

(a) (b)

Figure 4.6: Optical micrograph of PDMS interconnects using a (a) glass capillary tube (O.D. 0.84 mm), and (b) plastic capillary tubing (O.D. 1.02 mm), indicating no epoxy blockage in the tube.

4.4. PDMS Interconnect Characterization

In order to characterize the PDMS interconnect performances, three important measurements were conducted: leakage pressure measurement, leakage rate measurement, and pull-out force measurement.

4.4.1. Leakage Pressure Measurement

The leakage pressure characterizes the maximum working pressure that PDMS interconnect can stand. The measurement was conducted by connecting a syringe to PDMS interconnect as illustrated in Figure 4.7. A pressure gauge (Cole-Parmer 1202-5000, Cole-Parmer Instrument Company) was coupled with the syringe by a three-way pressure gauge tee (Upchurch U.433, Upchurch Scientifics). PDMS interconnect was bonded to different substrate materials by O_2 RIE bonding and UV epoxy bonding. A force was applied to push the syringe cylinder until leakage occurs. From the coupled pressure gauge, the leakage pressure was recorded and summarized in Table 4.1 for different substrate materials.

Table 4.1: Leakage pressure for different substrate and thin film materials (pressure unit: kPa)

	Oxygen RIE Bonding		**UV Curing Epoxy Bonding**	
	Sample#1	**Sample#2**	**Sample#1**	**Sample#2**
Silicon	435	422	435	483
Glass	503	456	184	138
PDMS	510	490	381	367
SiO_2 thin Film (100nm)	435	408	231	204
Si_xN_y thin Film (100nm)	374	292	88	68

From Table 4.1, it is seen that PDMS interconnect bonded with silicon can stand a pressure up to 435 kPa using O_2 RIE bonding. The leakage took place around punched holes. This implies that the friction force between the sidewall of PDMS hole and the capillary surface is critical for a high leakage pressure of PDMS interconnect. Therefore, the circularity of the hole punched is important for PDMS interconnects. For the interconnect with a non-circular hole, the experiment showed the leakage pressure could be less than 6.8 kPa (1 psi). For UV epoxy bonding, the measured leakage pressure ranges from 68 kPa (10 psi) for Si_xN_y thin film to 485 kPa (71 psi) for the silicon substrate. Most of the time, the leakage occurs at the bonding interface. This is because UV epoxy is very sensitive to surface cleanness. We believe ultrasonic cleaning itself can not guarantee adequate cleanness for UV epoxy bonding. Our experiments demonstrated that ultrasonic cleaning followed by O_2 RIE cleaning of the bonding surfaces for 15 seconds can stand a leakage pressure of about 683 kPa (100 psi) for UV epoxy bonded PDMS interconnect as shown in Figure 4.5 (a).

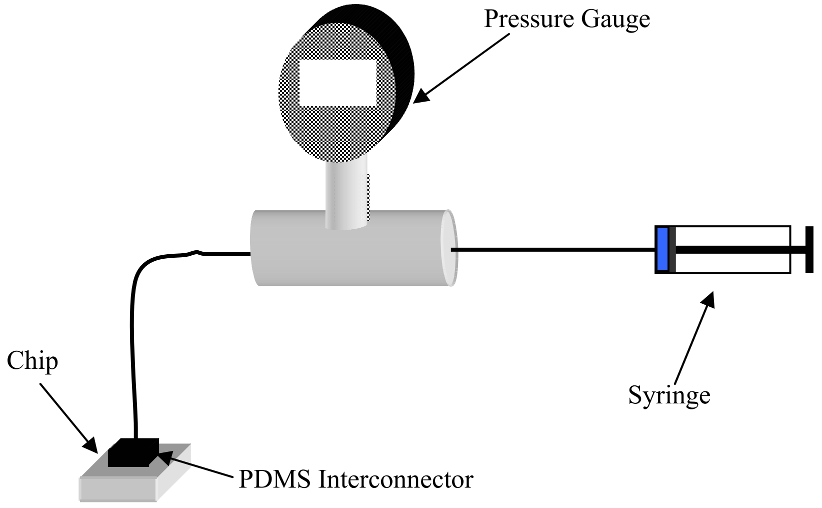

Figure 4.7: The experimental setup for leakage pressure measurement.

4.4.2. Leakage Rate Measurement

Leakage rate is another important measure for interconnect performances. Usually, the leakage rate was measured under a constant working pressure. Since a working pressure of 136 kPa (20 psi) is typical for microfluidic system applications [12], we used a weight of 1.25 kg to establish a pressure of 136 kPa (20 psi) in the gastight syringe with a diameter of about 10 mm. The experimental setup is shown in Figure 4.8. The 5 ml syringe was connected to the PDMS interconnect via a Teflon PTFE tube (O.D. 1.02 mm, I.D. 0.56 mm, Hamilton Company). The interconnect was bonded to a silicon wafer through O_2 RIE bonding and UV epoxy bonding. The maximum friction force between the syringe cylinder and the tube was measured as 2 N. The water volume in the syringe was recorded every 30-minute over 5 hours. Figure 4.9 shows the results of leakage rate measurement. It is found that water filled the tubing and interconnect for the first 30 minutes during which the volume of liquid inside the syringe decreased significantly. After this the fluid volume inside the syringe remains constant indicating the leakage is so minimal it is difficult to detect.

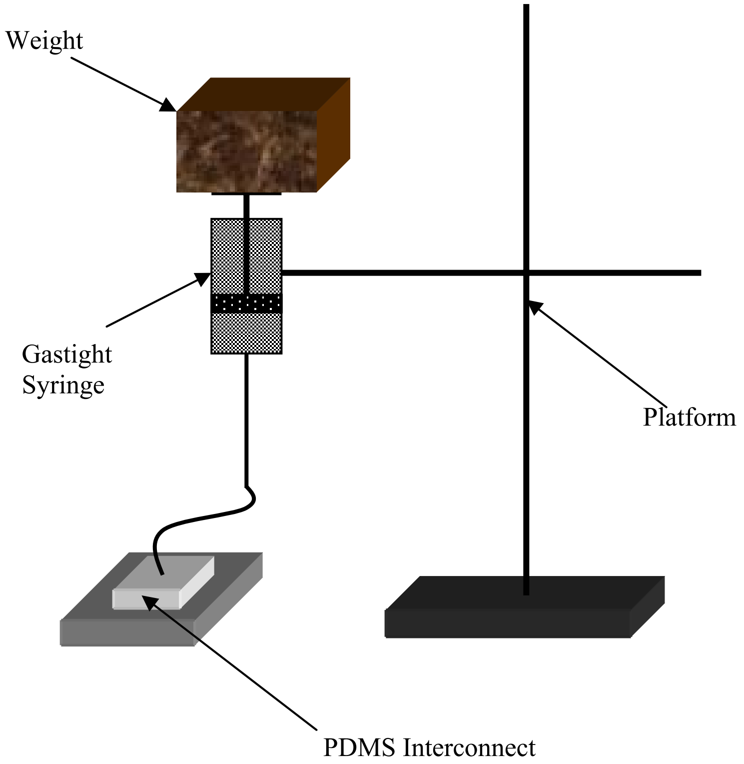

Figure 4.8: The experimental setup for leakage rate measurement.

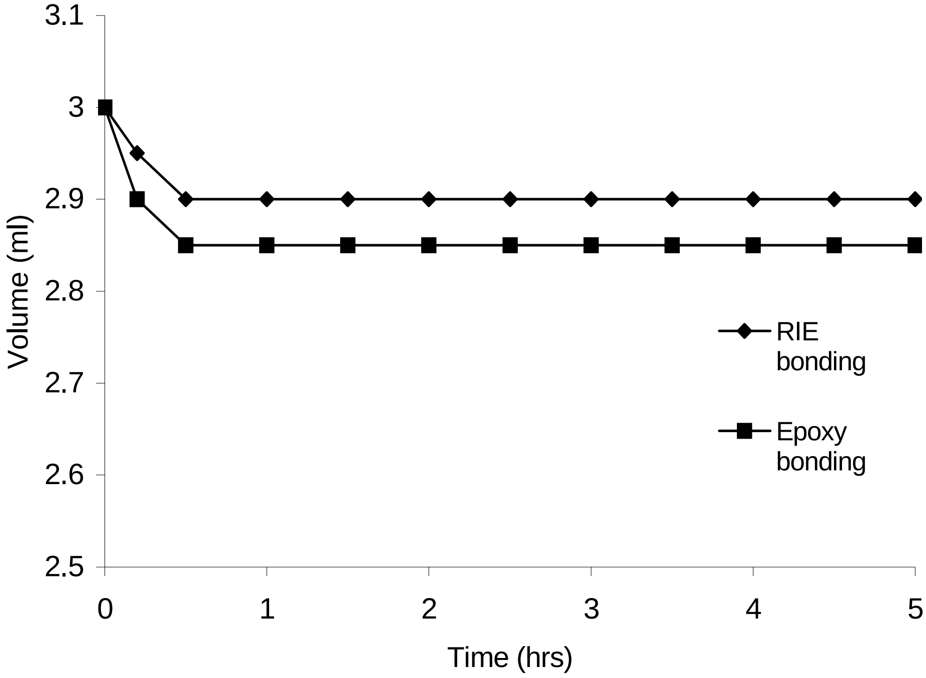

Figure 4.9: Results of leakage rate measurement for the PDMS interconnect bonded to a silicon substrate via O_2 RIE bonding and UV epoxy bonding.

4.4.3. Pull-Out Force Measurement

The required force to separate interconnect from the microsystem was characterized by a pull-out test. A Teflon PTFE plastic tubing (O.D. 1.02 mm, I.D. 0.60 mm, Hamilton, 9064) and a glass capillary (O.D. 0.84 mm, I.D. 0.60 mm, Vitrocom, CV6084) were chosen to characterize the pull-out force. The plastic tubing was directly plugged into interconnect and tightened on a force gauge tip. The pull-out force was recorded from a digital force gauge (CE, FG-20KG). We glued the glass capillary with Teflon plastic tubing (O.D. 1.47 mm, I.D. 0.86 mm, Hamilton) and then plugged the tube into PDMS interconnect. One of the major advantages of PDMS interconnects is that they are reusable. After several times of plugging and unplugging, the results for the pull-out force measurement of PDMS interconnects are similar. In Figure 4.10, for the plastic tubing, there is no significant change of the pull-out force even after reusing the plastic tubing ten times. But for the glass capillary tube, the pull-out force decreases from 750 mN to 250 mN for the 10th cycle. This indicates that the glass tube tends to damage the side wall of PDMS hole. When we used UV epoxy to seal the tubing and the sidewall of the hole for non-reusable interconnects, the pull-out force was found to be as big as 2 N.

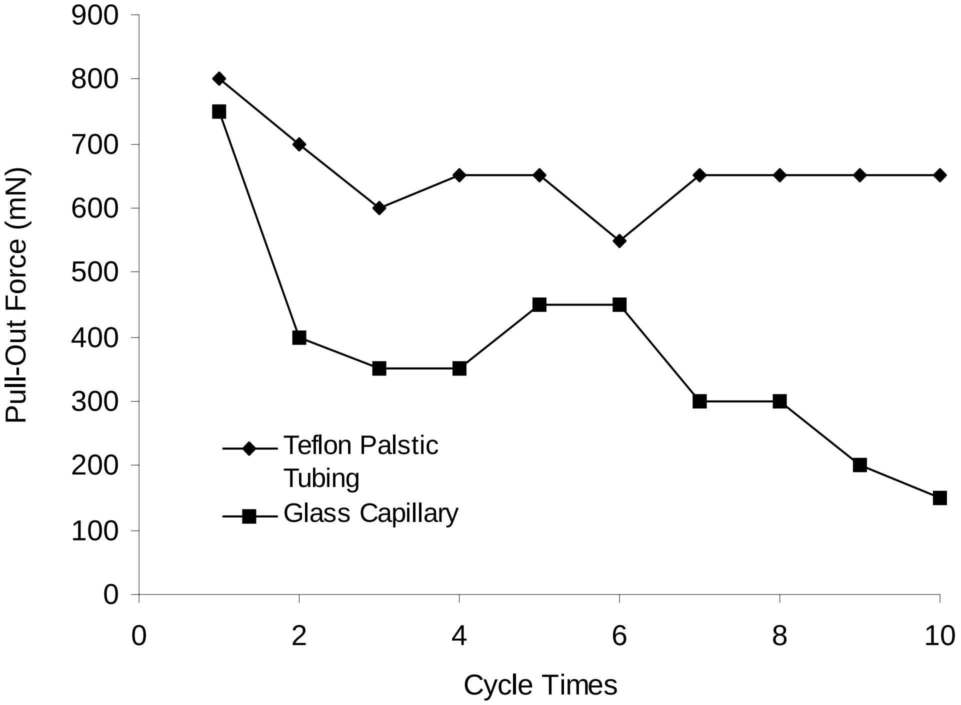

Figure 4.10: Results of pull-out force measurement for plastic tubing and glass capillary.

4.5. Conclusions

We have demonstrated that PDMS material can be used as interconnects for glass and plastic tubing in microfluidic applications. PDMS interconnect can be easily applied in different microfluidic systems made of glass, silicon, polymer and other MEMS materials such as gold, SiO_2 and Si_xN_y thin films at a low cost using either UV curable epoxy or RIE plasma activation. Leakage pressure, leakage rate, and pull-out force testing showed that PDMS interconnects have excellent performances. Key factors for strong bonding strength are the circularity of the hole punched in PDMS and cleanness of the surfaces to be bonded. Moreover, PDMS interconnects are re-usable and their fabrication is simple and cost-effective.

4.6. References

1. Gonzalez C., Collins S. D. and Smith R. L., 1998, *Sensors and Actuators B*, 49, 40-45.
2. Yao T.J., Lee S.W., Fang W.L. and Tai Y.C., 2000, *Proceedings of IEEE MEMS 2000 Conference*, 624-627.
3. Wijingaart W., Andersson H., Enoksson P., Noren K. and Stemme G., 2000, *Proceedings of IEEE MEMS 2000 Conference*, 674-679.
4. Armani D., Liu C. and Aluru N., 1999, *Proceedings of IEEE MEMS 1999 Conference*, 222-227.
5. Puntambekar A. and Ahn C. H., 2002, *Journal of Micromechanics and Microengineering*, 12, 35-40.

6. Gray B.L., Jaeggi D., Mourlas N.J., Van Drieenhuizen B.P., Williams K.R., Maluf N.I. and Kovacs G.T.A., 1999, *Sensors and Actuators A*, 77, 57-65.
7. Tsai J.H and Lin L.W., 2002, *Journal of Micromechanics and Microengineering,* 11, 577-581.
8. Pattekar A.V. and Kothare M.V., 2003, *Journal of Micromechanics and Microengineering*, 13, 337-345.
9. Xia Y.N., and Whitesides G.M., 1998, *Annu. Rev. Mater. Sci.*, 28, 154-184.
10. Jo B.H., Lerberghe L.M., Motsegood K.M. and Beebe D.J., 2000, *Journal of Microelectromechanics Systems*, 9, no.1, 76-81.
11. Unger M.A., Chou H.P., Thorsen T., Scherer A. and Quake S. R., 2000, *Science*, 288, 113-116.
12. Yang X., Grosjean C. and Tai Y.C., 1999, *Journal of Microelectromechanical Systems*, 8, 393 - 402.

Chapter 5: Disposable Polydimethylsiloxane/Silicon Hybrid Chips for Protein Detection with Microchip-Based Assays

5.1. Abstract

This chapter presents two disposable analysis chips - a single chamber type and a four-chamber type - made from poly (dimethylsiloxane) (PDMS) and silicon for protein detection. The chips consist an inner silicon layer with an etched array of micro-cavities hosting agarose beads, sandwiched between two PDMS layers. The biological sample was introduced into an inlet at the top PDMS layer where it flows to the bead chamber. The sample passed through the beads where it exited from an outlet at the bottom PDMS layer. Signals generated on the beads were captured with a CCD camera, digitally processed, and analyzed. An established bead-based fluorescent assays for C-reactive protein (CRP) was used to characterize the single chamber and the four-chamber chips. The detection limit of the single chamber PDMS chip was found less than 0.1ng/mL. Using the back pressure compensation method, the signal from the four chambers of the four-chamber chip was found close. Moreover, the four-chamber PDMS chip increased the capacity of the assay.

5.2. Introduction

A polymer based miniaturized system provides a powerful platform for biological assays due to its many advantages over conventional bench-top systems including low cost, smaller reagent, less power, higher throughout and portability [1,2,3]. The development of miniaturized device must take into account the type of material used to fabricate the device. The material should be compatible with sensitive method of detection, enable easy integration of other functional components. If the devices are aimed for the mass production, the material should be inexpensive so the device can be single-use. Due to these requirements, silicon and glass are not as favorable as polymers substrates like polyimide, poly (dimethylsiloxane) (PDMS), poly (methyl methacrylate) (PMMA) and polycarbonate (PC).

There have been many different polymer based assay chips fabricated from polyimide [4], PMMA [5-9], PDMS [10-13] using micromolding, and polycarbonate (PC)[14,15]using injection molding. Some polymer based chips have been built using the combination of materials, such as PDMS/silicon [16], PMMA/PDMS [17, 18], and PDMS/glass [19, 20]. Moreover, of these widely used materials, PDMS has been proven for use in miniaturized microfluidic bioanalysis systems due to biocompatibility, cost-effectiveness and disposability, transparent nature to UV/visible light, and mature fabrication techniques. Additionally, PDMS is easily sealed with different substrates [21]. In parallel to the rise of interest of polymer material for the assay chip, the assay format was also extensively studied. The fluorescent bead-based assay received increasing attention [5, 6, 9, 22, and 23]. The microbeads as platform may yield better results for surface binding-based assay and analysis due to the larger surface-to-volume ratio compared with surface immobilized assay [24].

We have developed two types of disposable analysis chips - a single-chamber and a four-chamber - for protein detection. These chips were made from PDMS and silicon. Using the bead based C-reactive protein (CRP) assays, the performances of these chips were evaluated. The single-chamber chip is for single analyte assay, whereas the four-chamber chip increased the capacity of the assay and has multiplex potential.

5.3. PDMS/Silicon Hybrid Chip Design and Fabrication

5.3.1. Microchip Based Bead Assays

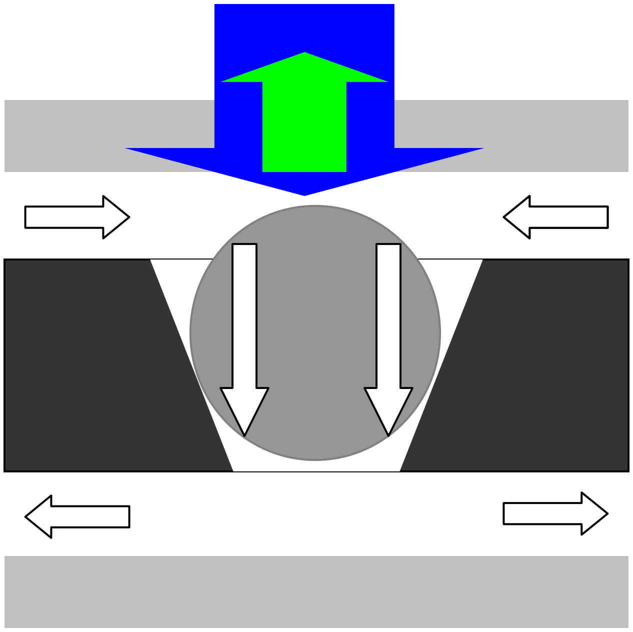

Figure 5.1: Schematics of microchip based bead assays

The microchip based bead assay has been described in previous papers [5, 6, and 9]. A pyramid microcavities array was anisotropically etched in silicon wafer. Agarose beads of approximately 300 μm in diameter were host in the microcavities, which served as microreactors and microanalysis chambers (Figure 5.1). Using the top-to-bottom flow direction, the beads within microcavities were exposed to analytes as the solution was pumped into the upper reservoir of the flow cell, forced down through the wells to the bottom reservoir and out through the drain. Due to the three-dimensional nature of microcavities, the mixing would form when analytes flew through microbeads. The mixing can enhance antigen and antibody reaction. Also, the space between the upper layer and the silicon chip was approximately 50 μm so that the analyte can easily fill with the entire chamber and make analytes flow evenly through each cavity.

5.3.2. PDMS/Silicon Hybrid Chips Design

The hybrid chips consist of an inner silicon layer with an etched array of micro-cavities hosting agarose beads (Figure 5.2), sandwiched between a top and a bottom fluidic network PDMS layers fabricated using soft lithography techniques. The assay uses the "sandwich" format (Figure 5.3). The transparent agarose beads located in microcavities were coated with antibodies which captured the specific reagent. The reagent, in turn, captured the detecting antibodies conjugated with fluorophore. The single chamber chip was designed for single analyte assay (Figure 5.4). From the previous experiments, we found, for different flow experiments, the emission of light source can be fluctuated to affect the assay performances. Also, some cross reactivity between the different reagents was found during the multiplex assay. In order to overcome these problems, PDMS chip with four detection chambers was proposed allowing for four simultaneous assays (Figure 5.5).

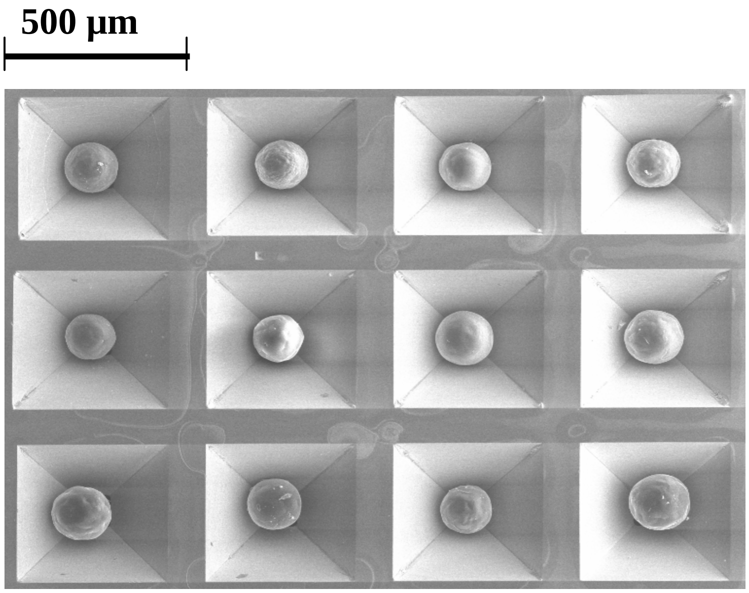

Figure 5.2: Scan electron microscope picture of the silicon chip with beads (courtesy of Prof. McDevitt and Prof. Neikirk at UT Austin)

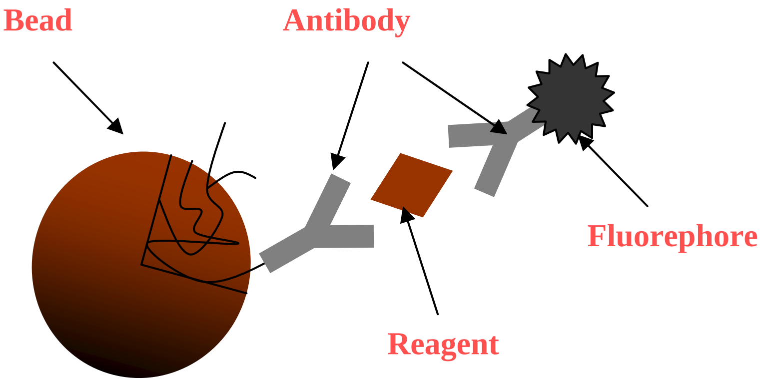

Figure 5.3: The “sandwich” format immunoassay.

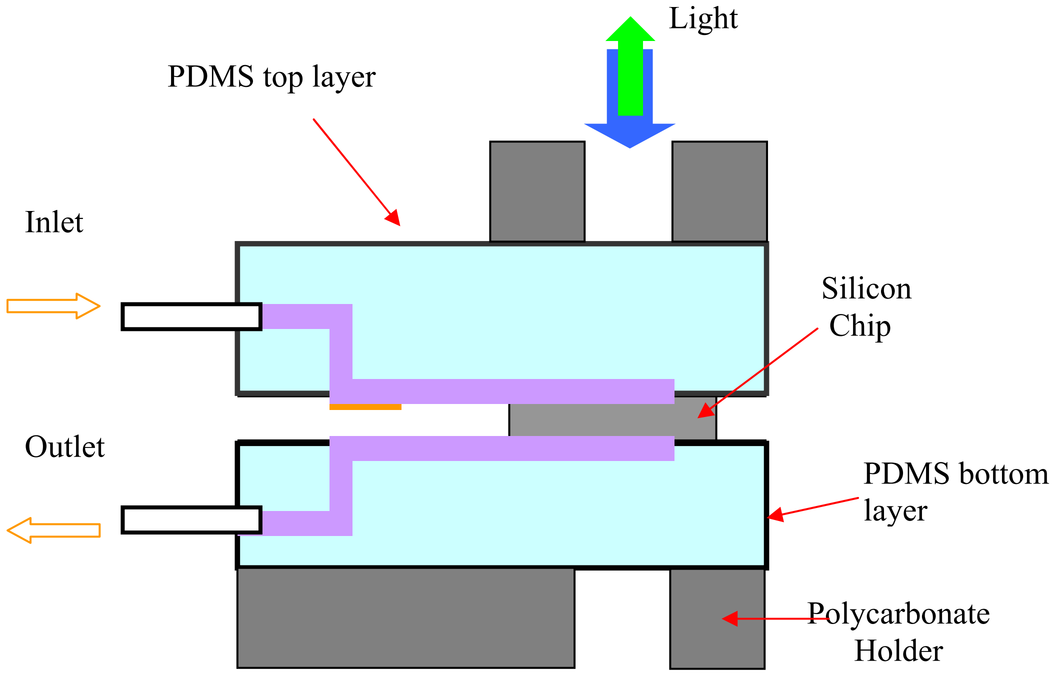

Figure 5.4: Schematics of the single chamber PDMS/Silicon hybrid chip.

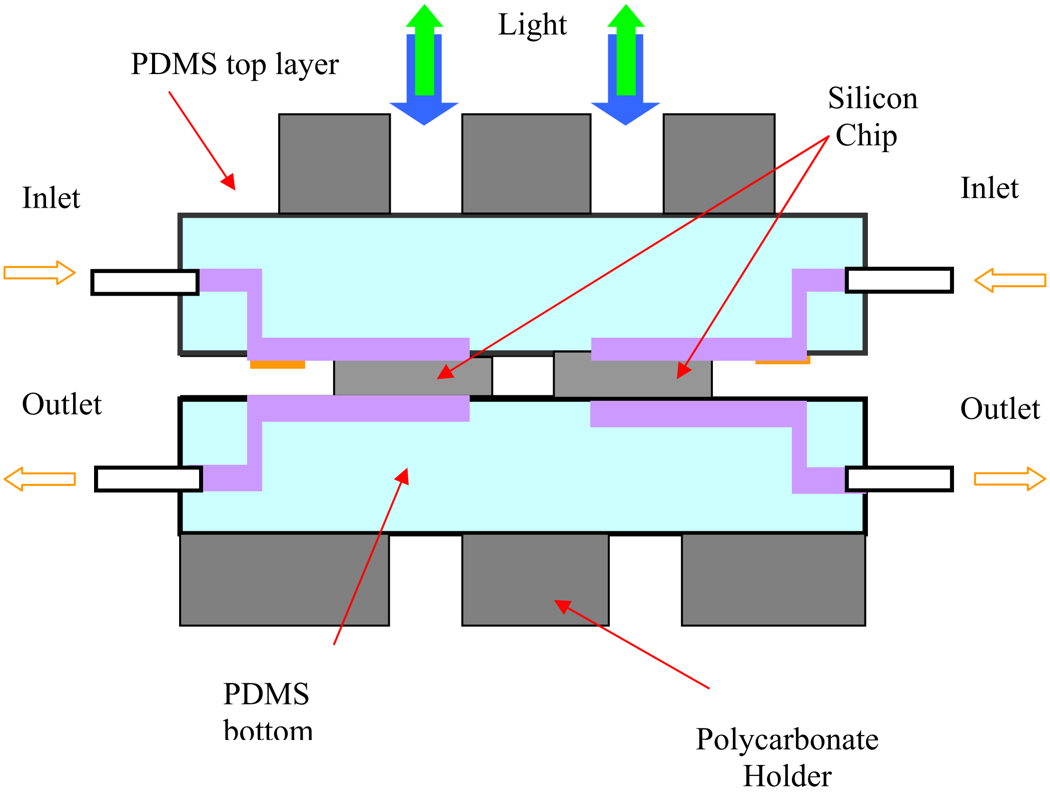

Figure 5.5: Schematics of the four-chamber PDMS/Silicon hybrid chip.

In order to seal the silicon chip and handle the relatively high flow rates required for the assay (0.07ml/min to 2ml/min), one must consider the pressure issue for the chip design. When the sample flows through the chamber, the pressure would be built up inside the chamber. The built-up chamber pressure, together with the applied holding pressure, would deform the chamber membrane. If the chamber space, distance between the silicon chip and the upper PDMS membrane, is more than 200 μm, the beads would erratically jump out of microcavities due to the flow pressure. Therefore, it is necessary that the clamping pressure be sufficient to keep the silicon chip and PDMS layers sandwiched together and to maintain the chamber spacing below 200 μm. ANSYS, finite element analysis software, was used to determine the dimensions and design parameters of chips by considering the factors like the chamber pressure, the holding pressure, and the chamber/channel deformation. The Young's Modulus and the Poisson ratio of the PDMS membrane were assumed as 3 MPa and 0.49 respectively [25]. The total dimension of microcavity array is about 3 mm × 2.7 mm, so the width of the PDMS chamber is chosen as 5 mm × 5 mm to cover the entire microcavity array.

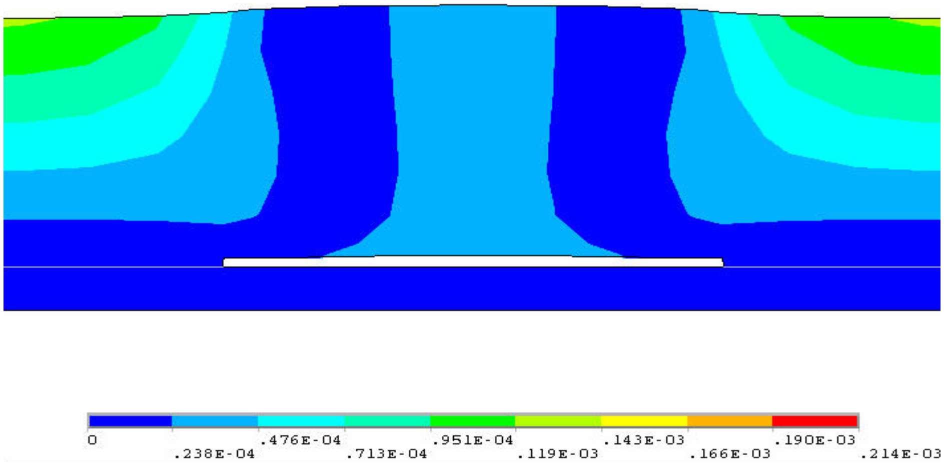

(unit: m)

(a)

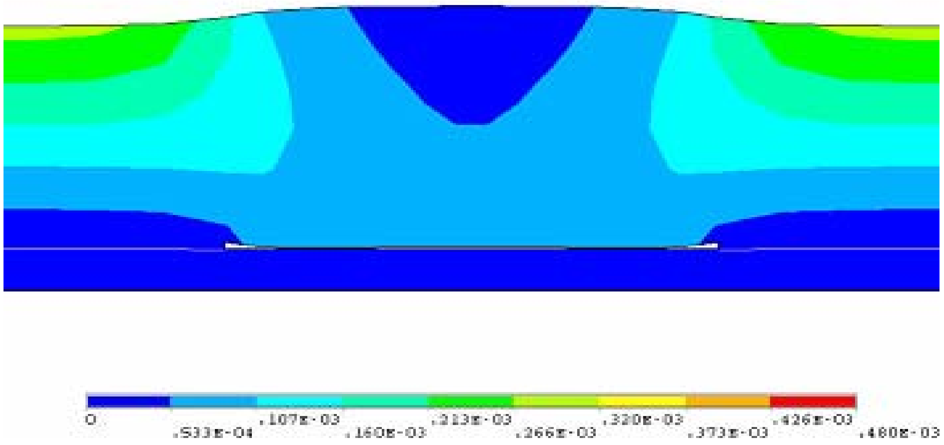

(unit: m)

(b)

Figure 5.6: The deformation of PDMS chamber and channel at a chamber pressure of 34 kPa (5 psi) and a holding pressure of (a) 150 kPa, and (b) 350 kPa.

Since the maximum chamber pressure was found to be less than 102 kPa (15 psi) from the previous experiment, we used three chamber pressures of 34 kPa (5 psi), 68 kPa (10psi) and 102 kPa (15 psi), respectively in the simulation. With the increase of the holding pressure, the chamber space was decreased (Figure 5.6a and b) whereas the deformation of the channel inside PDMS layer was increased (Figure 5.7). From the simulation results and fabrication point of view, the height of the chamber was chosen as 100 μm. The height and width of the channel are 50 μm and 500 μm, respectively.

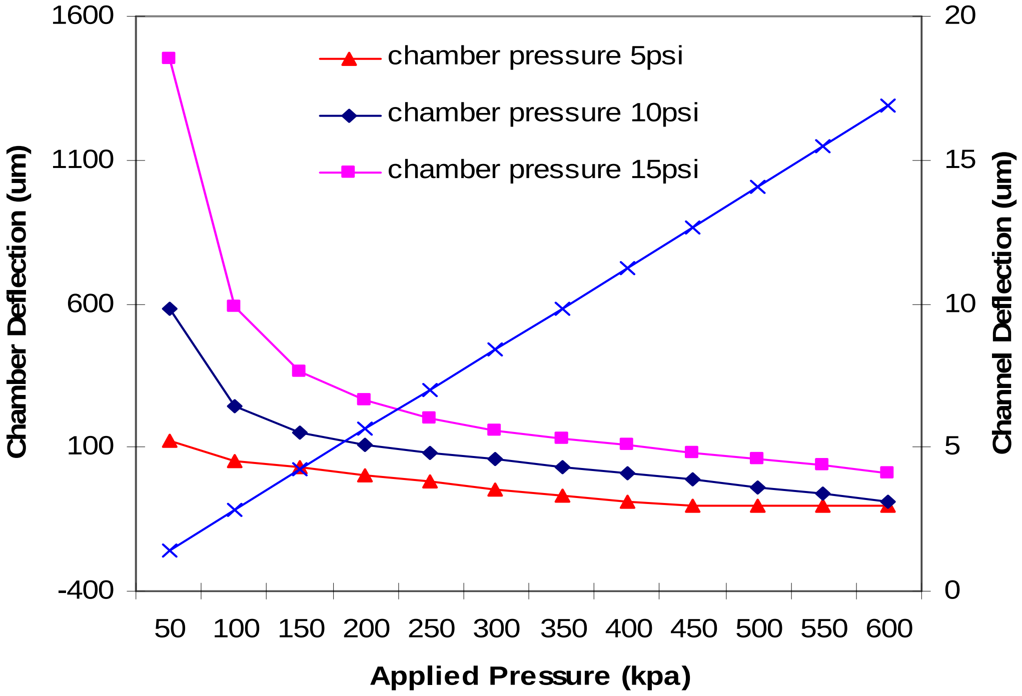

Figure 5.7: The deformation of PDMS chamber / channel at different holding pressures and chamber pressures.

5.3.3. PDMS/Silicon Hybrid Chip Fabrication

The first step in developing PDMS chip is to fabricate a silicon mold. Transparencies printed using 2000dpi laser printers were used as the photomasks for creation of the molds. 4" silicon wafer (Nova Electronic Materials, Inc., TX, USA) was cleaned using a piranha solution (30% H_2O_2: 96% H_2SO_4 = 825ml: 1650ml). After blowing-dry using nitrogen gas, the silicon wafer was put on a hot plate (120°C) for 5 minutes to remove water. Hexamethyldisilizane (HDMS) was then spun on the silicon wafer to enhance adhesion. Negative photoresist SU-8 (MicroChem, Newton, MA, USA) was coated on the silicon wafer (3000 rpm and 30 seconds), resulting in a thickness of about 50 μm. The coated silicon wafer was then put into a 90 ^{o}C prebake oven for one hour. The silicon wafer was relaxed for 10 minutes before putting into a wafer aligner. The wafer was then exposed for 2.5 minutes, relaxed for another 10 minutes and then put into the oven at 90^{o}C for one hour post-exposure baking. After the post-exposure baking, the silicon wafer was developed (MicroChem, Newton, MA, USA) for 6 minutes and rinsed using isopropyl alcohol (IPA). Finally, a 10-minutes postbaking was carried out to enhance SU-8 photoresist adhesion.

To prepare PDMS layers, a curing agent and PDMS prepolymer (SYLGARD 184 Silicone Elastomer Kit, Dow Corning, Midland, MI) in a 1:10 weight ratio were mixed. Then the prepolymer mixture was degassed in a 20-25 mmHg vacuum chamber for one hour to remove air bubbles in the mixture and ensure complete mixing of the two components. A special two-step curing method was developed to fabricate channels inside PDMS bulk material. Before the prepolymer was poured on the silicon mold, a thin carbon layer was deposited on the mold using reactive ion etching (RIE) to allow easier removal of PDMS layers after curing. The parameters for RIE deposition are 100 W, 100 sccn CHF_3 and 1.5 minutes [26]. In order to make certain thickness PDMS layers, a plastic ring of 100mm diameter and 5 mm thickness was covered on the silicon mold to hold PDMS prepolymer. The prepolymer mixture of about 10 ml was poured into this plastic ring. Due to the surface tension force, the prepolymer would cover the entire silicon wafer uniformly. The thickness of PDMS inside the ring was approximately1-2 mm. After 5 minutes curing at 100 ^{o}C on a hot plate, metal pins of 800 μm in diameter were positioned on the first PDMS layer and then another 10-20 ml prepolymer mixture was poured to fill the whole ring. The extra prepolymer can be scraped from the plastic ring using a plastic blade. PDMS was then cured for 1 hour at 100 ^{o}C on the hot plate. Then, these two PDMS layers were cured into one PDMS layer with a thickness of approximately 5 mm. The PDMS layer was finally cut into 20 mm by 40 mm and took out of the metal pins inside the PDMS layer. Holes of 1.5 mm in diameter were punched using 1.5 mm glass capillary to connect the channels inside the PDMS layers with the open channels on the surface of PDMS layers.

To seal the open channels, an additional PDMS layer of 50 μm thick was prepared as follows. A 4"silicon wafer was cleaned using a piranha solution. Using the aforementioned method, the silicon wafer was first covered by a thin carbon layer, followed by spin-coating of a prepolymer layer (20 ml) at 2000 rpm speed for 20 seconds. The coated silicon wafer was cured for half hour at 100 ^{o}C on a hot plate. The final thin PDMS layer thickness was about 50 μm. Before sealing, the 5 mm thick PDMS layer was cleaned using IPA followed by deionized water (DI) water for 5 min ultrasonic cleaning. After cleaning, PDMS layers were put in a 90 ^{o}C oven for 15 minutes to remove water molecule. Then, the sealing PDMS layer and the thick PDMS layer with microchannels were put into a RIE chamber to actuate the bonding surface using oxygen plasma. The parameters for oxygen plasma treatment were 75 W, 70 mtorr and 15 seconds. After surface actuation, the PDMS layers were put together immediately and heated at 100 ^{o}C for half hour to achieve permanent bonding. The bonded PDMS plate was then released from the silicon wafer. The detection chamber windows were opened using a razor blade. Previous experiments shown the membrane at the punched hole was easily burst out at higher flow rates. A piece of 100 μm thickness glass sheet was bonded to strength PDMS seal over the punched holes using the oxygen plasma bonding. The maximum strength of glass and PDMS bonding could reach 476 KPa (70 psi) [21]. Figure 5.8 is general fabrication processes and Figure 5.9a is the fabricated single chamber PDMS/Silicon chip and Figure 5.9b is the fabricated four-chamber PDMS/Silicon chip.

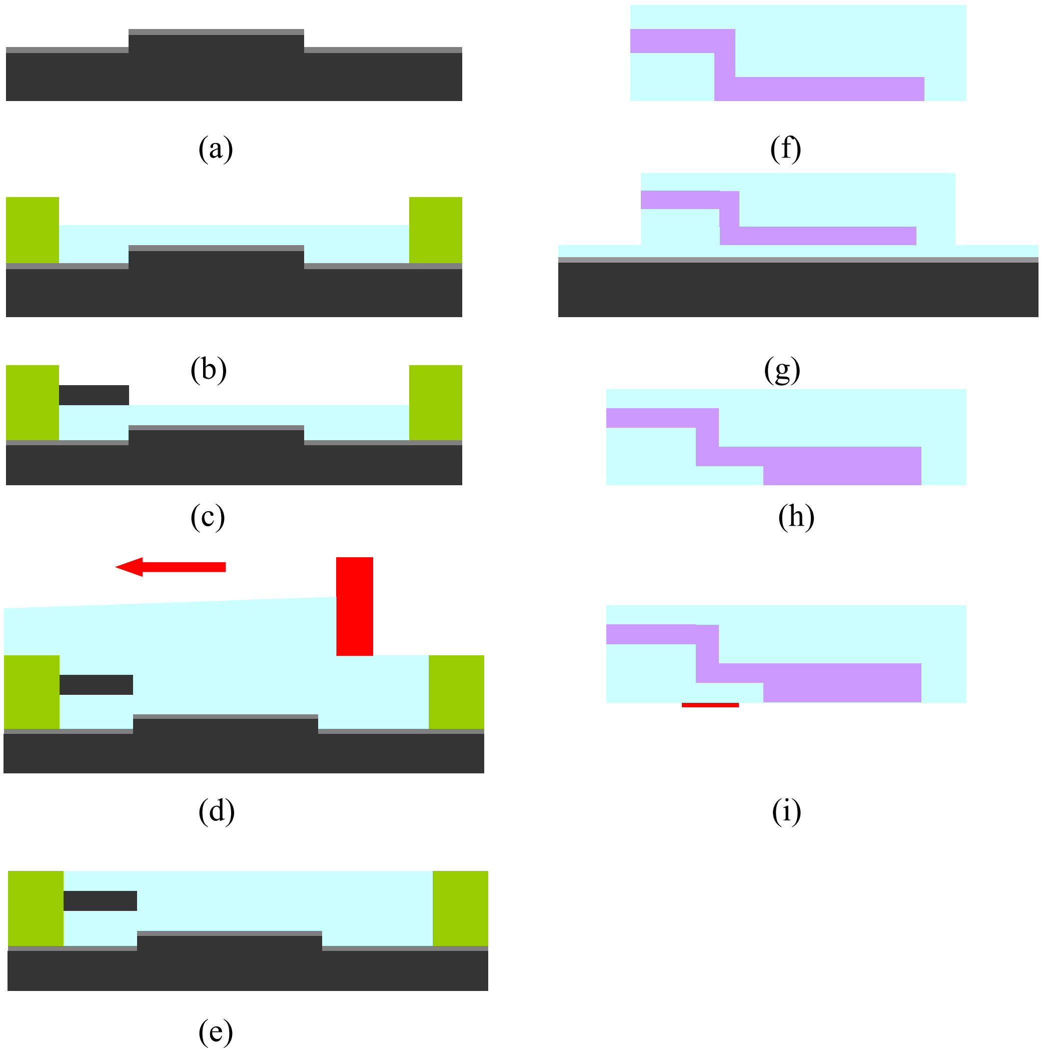

Figure 5.8: The fabrication process flow for the PDMS fluid network layer: (a) carbon thin film deposition on the silicon mold, (b) plastic ring position and the first PDMS prepolymer layer preparation, (c) pin positioning, (d) the second PDMS prepolymer layer injection, followed by removal of extra prepolymer, (e) 1 hr curing at 80°C, (f) PDMS layer removal and hole punching, (g) 50 µm thick PDMS layer spin coating, curing and bonding with the thick PDMS layer, (h) PDMS chamber opening, (i) 100 µm thick glass sheet bonding.

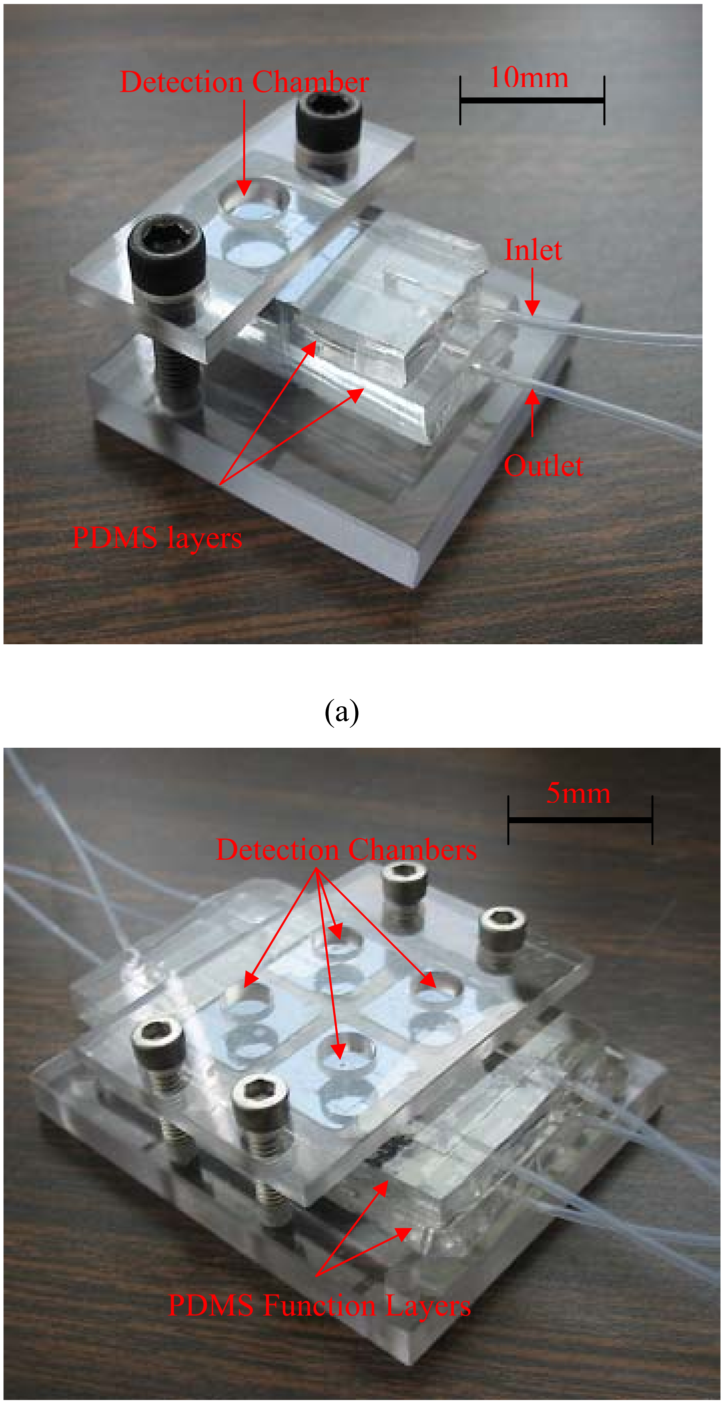

(a)

(b)

Figure 5.9: An optical picture of a (a) single chamber PDMS chip (b) four-chamber PDMS chip

5.4. Experiments

5.4.1. Experiment Materials and Instrumentation Setup

Agarose microbeads were obtained from XC Corporation (Lowell, MA). The CRP-specific antibodies were purchased from Accurate Chemical, Scientific Corporation (Westbury, NY) and Biogenesis (Kingston, NH). Alexafluor-488 was conjugated to the detecting antibody using a commercially available kit from Molecular Probes (Eugene, Oregon). The CRP standards were obtained from Cortex Biochemical (San Leandro, CA). Anti H. pylori antibody was obtained from Accurate Chemical and Scientific Corporation. The CRP-specific and control (rabbit anti H. pylori) antibodies were then coupled to the beads by reductive amination, as described Figure 5.10. Here, aldehyde groups of "glyoxal" agarose beads react with ligands (such as antibodies) to form reversible Schiff Base complexes that can be selectively reduced and stabilized as covalent linkages with sodium cyanoborohydride.

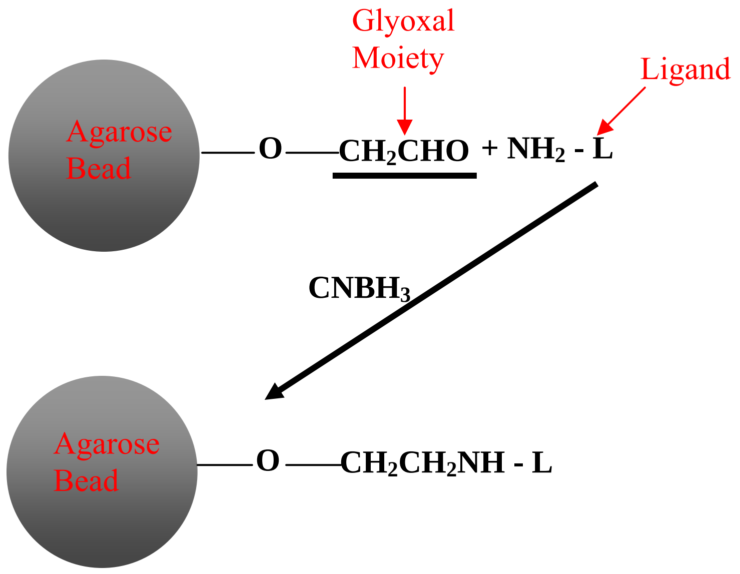

Figure 5.10: Coupling of antibody with glyoxal actuated agarose beads

The assay setup was similar to those described in previous papers [5, 6, and 9]. The individual beads were placed into silicon microcavities patterned in a 3 × 4 square array. The silicon chip was packaged with two PDMS layers. The polycarbonate holders were used to hold the three components together. This fluidics system was coupled to a PDMS chip positioned on the motorized stage of a modified compound BX2 Olympus microscope. The microscope was equipped with various objectives, optical filters, and a charged-coupled device (CCD) camera which operation can be automated. A mercury lamp was used as the light source. Fluorescence images were obtained with a FITC filter cube (fluoroisothiocyanate, 480 nm excitation, 505 long pass beam splitter dichroic mirror, and 535 ± 25 nm emission), and captured by a DVC 1312C (Digital Video Company, Austin, TX) charge-coupled device (CCD) mounted on the microscope and interfaced to Image Pro Plus 4.0 software (Media Cybernetics). Areas of interest in the images of the array were selected in an automated fashion and used to extract light intensities. Figure 5.11 is schematics of assay experiment setup and Figure 5. 12 is optical picture of experiment of setup.

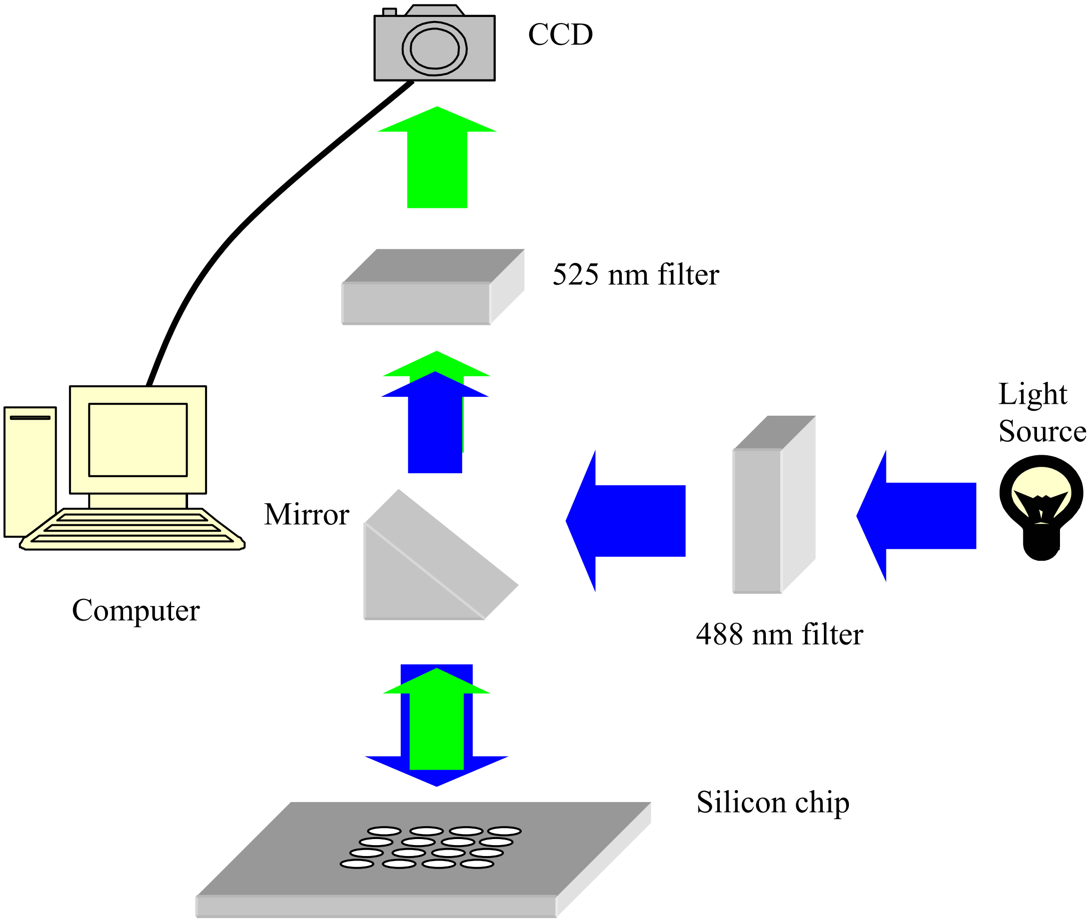

Figure 5.11: A schematic diagram of fluorescent measurement setup

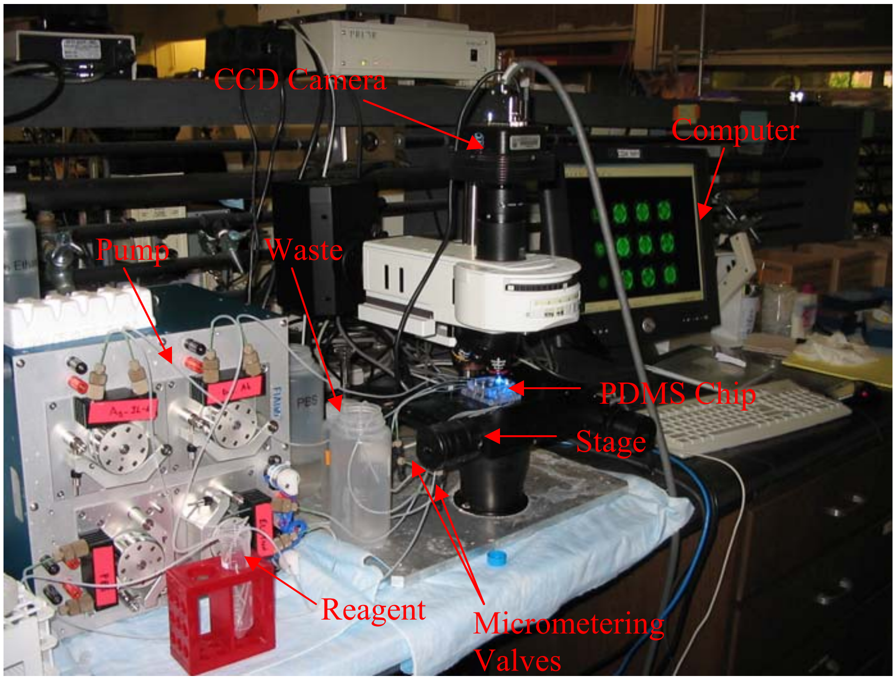

Figure 5.12: An optical picture of the experiment setup for PDMS chip characterization

5.4.2. Optimization of CRP Assay Protocol

PDMS was chosen as the device material for the assays for the following reasons: (1) it is an elastomer and can tightly seal different substrates, (2) it is hydrophobic surface property and prevents the protein absorption from solution, (3) it gives a low background fluorescence signal during the detection of fluorescent labeled protein, (4) it is transparent from UV to infrared wavelengths [16]. But PDMS is a soft material that easily deforms under an external force. From the finite element analysis and the pervious experiments, the leakage occurred when a higher flow rate (>0.4 ml/min) was used. The 0.1 ml/min flow rate was found to be optimal for PDMS chip assay. But, associated with the relative low assay flow rate, the bubble inside the chamber was difficult to remove. The lingering bubble can affect the generated signal for protein detection (Figure 5.13).

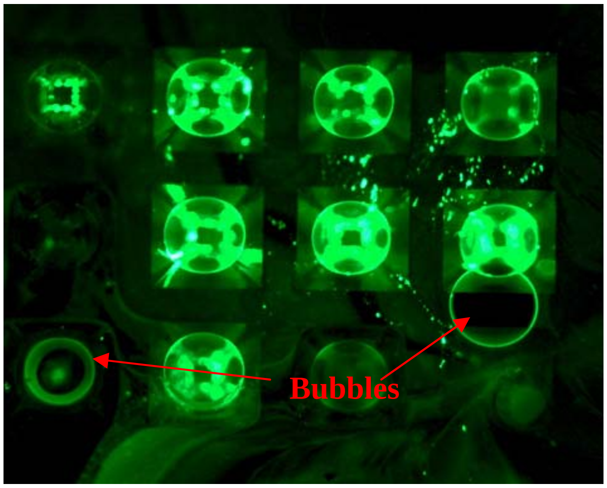

(a)

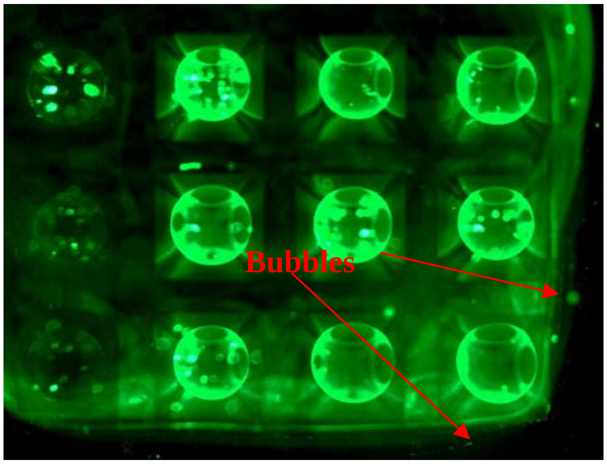

(b)

Figure 5.13: The bubble problem of the PDMS chip: (a) bubble sticking to the beads, (b) bubble shielding the beads.

In order to eliminate the bubble inside the chamber, two methods were used for the assays. The first method was to use continuous flow format instead of several priming between each step. The priming was found to introduce gas bubble during the assays. Without priming, the assay took longer because the reagent needs more time to flow through the inlet tubing to the flow cell. The second method was to connect a micro-metering valve with the drain tubing to regulate the backpressure that was found to effectively remove bubbles inside the flow cell chamber. By applying these changes, the optimal CRP assay protocol was as follows: prior to each assay, the inner wall of tubing used to introduce the reagent to the flow cell was primed. As illustrated in Figure 5.14, the CRP reagent was delivered into the flow cell at a flow rate of 0.1ml/min for 30 minutes. Then, Phosphate Buffed Saline (PBS) solution was delivered to wash the flow cell and tubing at 0.1 ml/min for 10 minutes. Following PBS washing, the detecting antibodies conjugated with Alexa 488 fluorophore were delivered to the flow cell at 0.1 ml/min for 30 minutes incubation. Finally, the PBS solution was delivered again at 0.1 ml/min for 10 minutes to generate the signal.

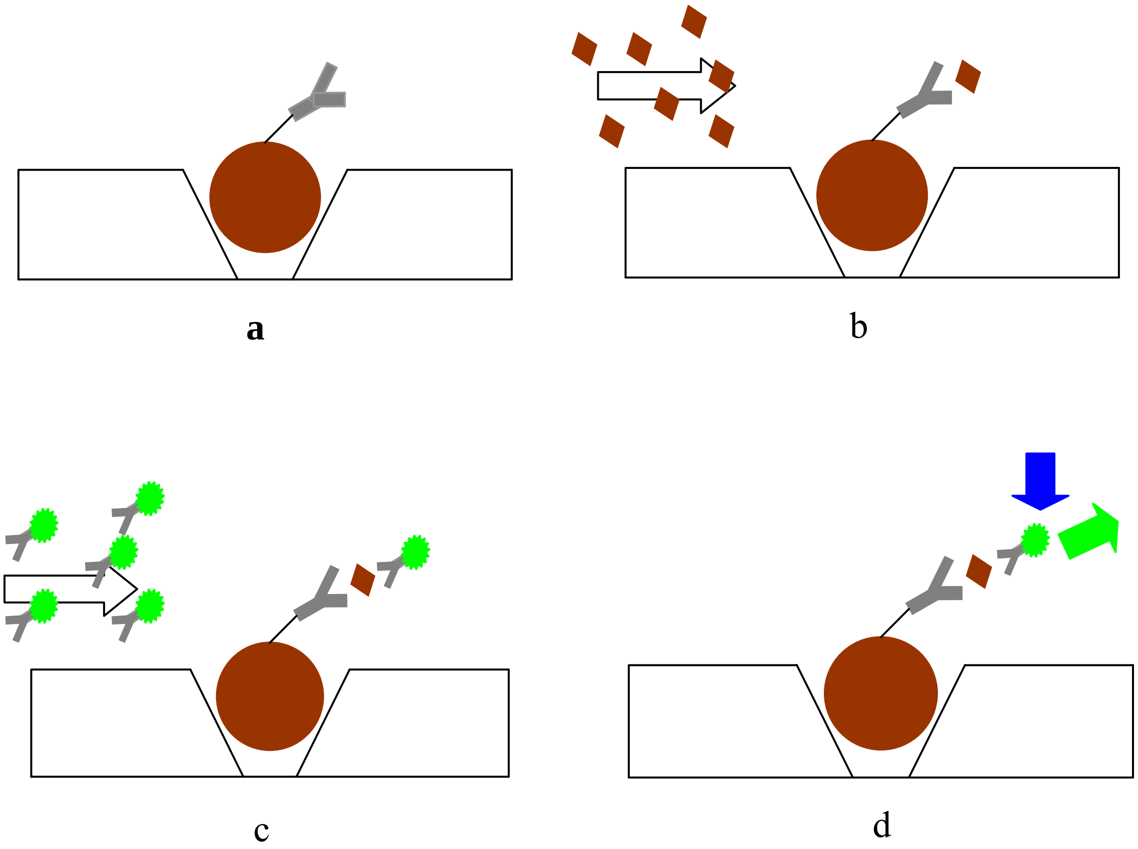

Figure 5.14: CRP sandwich immunoassay: (a) antibody coating on the beads, (b) capture of the antigen, (c) injection of the detecting antibody, (d) signal generation.

5.4.3. Single Chamber PDMS/Silicon Hybrid Chip CRP Assay Characterization

The CRP dose response experiment was used to characterize the performance of the single chamber PDMS/Silicon Hybrid chip. The transparent agarose beads located in microcavities were coated with anti-CRP antibodies which captured the CRP reagent. The reagent, in turn, captured the detecting antibodies conjugated with fluorophore. The fluorescent can be detected by the actuation of the conjugated fluorophore.

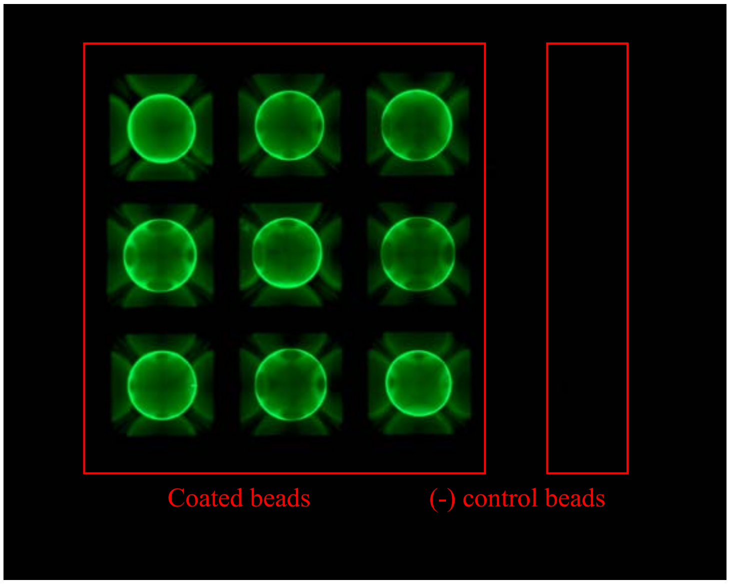

Figure 5. 15: Optical micrograph of beads for CRP concentration of 1000 ng/mL

Three of four columns in 3 × 4 array contained beads coated with anti-CRP antibodies whereas the fourth column was the negative control microbeads. After assay, the three columns with coated anti-CRP beads can be detected using a fluorescence microscope. However, the negative control beads can not be detected by fluorescence, so the protein non-specific bonding during the assay did not occur (Figure 5.15). In order to limit the non-specificilities from the fluorescence background, the silicon chip was ultrasonically cleaned using ethanol and followed by DI water cleaning for 5 minutes.

The ethanol temporarily makes PDMS surface hydrophilic to help solution fill the entire chamber.

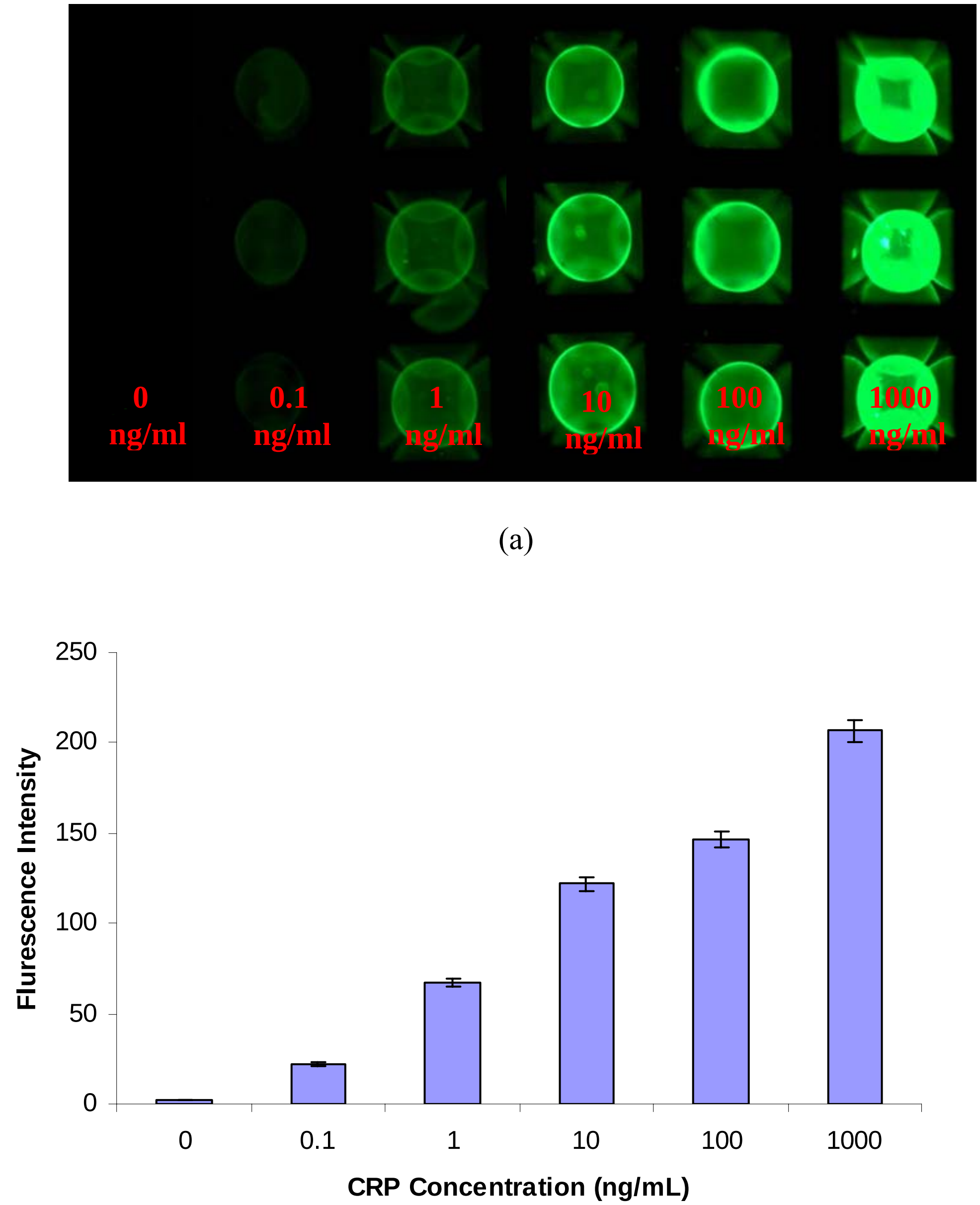

(a)

(b)

Figure 5.16: (a) Optical micrographs of anit-CRP coated beads at different CRP antigen concentrations (b) The measured intensity at the different CRP antigen concentrations

The same protocol was used to measure the CRP dose response to different concentration of CRP using the same single chamber PDMS flow cell (Figure 5.16a and b). The CRP concentration ranged from 0.1ng/ml to 1000ng/ml. The detection limit was less than 0.1ng/ml, which was lower than previously reported CRP assay systems [6].

5.4.4. Four-Chamber PDMS/Silicon Hybrid Chip CRP Assay Characterization

In previous experiments, the excitation light source was found to fluctuate for different assays and reagent cross-reactivity occurred during the multianalyte assay. The four-chamber PDMS/Silicon hybrid chip was developed to limit these problems and increase the capacity of assay. However, a critical issue associated with the multiple chamber design is to ensure each chamber functions equally for signal generation since the fluorescence signal can be strongly affected by the flow dynamics inside each chamber. There were many factors that can affect the flow dynamics, such as the chamber dimensions, the relative position of the microcavity inside the chamber, the deformation of PDMS layers, the uneven applied pressure, the tubing, and even the persimatic pump. The dimension of each chamber can be different due to the intrinsic resolution of the soft lithographic process. The relative position of the microcavity inside each chamber can affect the pressure drop that drives the analyte flow through the beads. The deformation of PDMS layers due to the holding pressure and physical change of connecting tubing can alter flow resistant inside the channel and the chambers. The peristaltic pump must push the solution at an equal rate. But it is difficult to maintain the exact same flow rate from chamber to chamber. Due to these physical reasons, it is hard to maintain identical flow dynamics inside each chamber. To limit these problems and to remove the bubbles, a back pressure compensation method was proposed. In-line micro-metering valves (UpChurch P-445) were connected to the outlet of each flow cell to regulate the back pressure. The flow dynamics was mainly controlled by the back pressure inside the bottom PDMS chamber. Following the aforementioned protocol, the response for 1000ng/ml CRP concentration was measured using the four-chamber PDMS flow cell. The result is shown in Figure 5.17 for chambers #1, #2, #3, and #4. The signal variation among chambers is less than 10% (Figure 5.18).

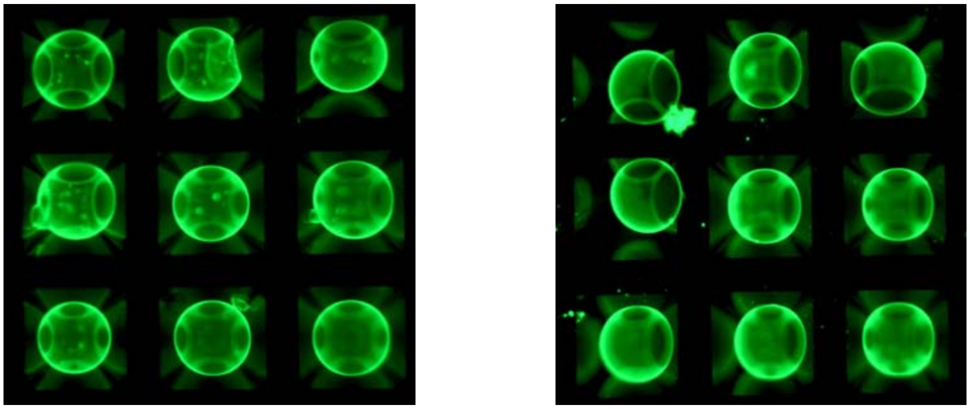

(a)

(b)

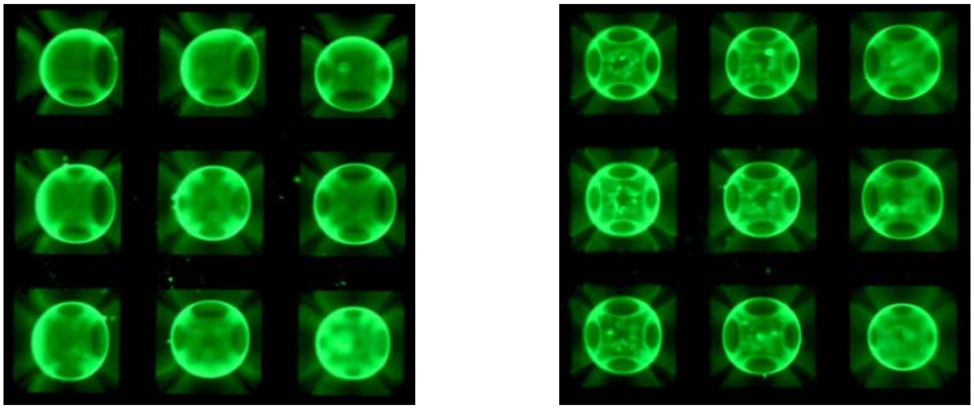

(c) (d)

Figure 5.17: Response of four chambers at 1000ng/mL using the back pressure adjustment, (a) chamber #1, (b) chamber #2, (c) chamber #3, (d) chamber #4.

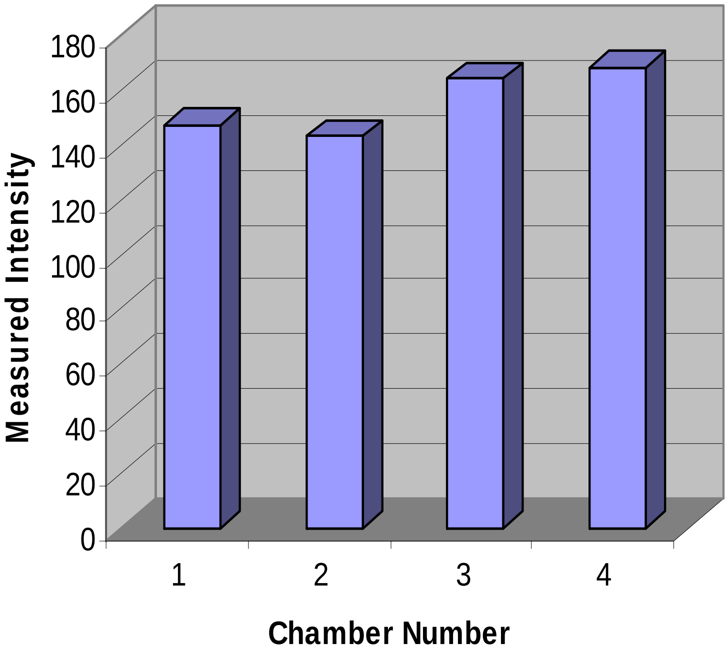

Figure 5.18: Measured intensity of CRP response for each chamber for the four-chamber chip at 1000ng/mL.

5.5. Disposability of PDMS/Silicon Hybrid Chips

One of major advantages of these PDMS/Silicon hybrid chips is their disposability. Using micromolding techniques, PDMS chips can be easily and massively fabricated. The major cost of these chips comes from the micromachined silicon chip. Moreover, these chips can be easily separated into three components: PDMS top layer, the silicon chip, and PDMS bottom layer after the assays. The silicon chip can be reused after ultrasonic cleaning. The top and bottom PDMS layers could be disposed due to their low cost. Then, the potential contamination can be avoided for different assays.

5.6. Conclusions

A single chamber chip and a four-chamber chip for protein detection were presented in this paper. Using the soft lithography techniques, a fluidic network was fabricated onto a top and bottom PDMS layers. An inner silicon chip with an etched array of micro-cavities hosting agarose beads was sandwiched between the top and bottom layers of PDMS. Since PDMS is a soft material, the maximum assay flow rate was found to be 0.4 ml/min. Finite element method was employed to analyze the deformation of the PDMS chamber and PDMS channel upon a holding pressure. The C-reactive protein (CRP) assay was used to characterize the single chamber and four-chamber chips. For the single chamber assay, the CRP detection limit could reach as small as 0.1ng/ml. The four-chamber PDMS chip was developed to solve problems of light emission fluctuation and the cross-reactivity. Using the back pressure compensation method, the performance of four-chamber has been improved significantly. The signal variation among chambers was less than 10%.

5.7. Reference

1. Whitesides G.M., Ostuni E., Takayama S., Jiang X., and Ingber D., *Annu. Rev. Biomed. Eng*, 2001, 3, 335-73
2. Beebe D., Mensing G. A. and Walker G. M., *Annu. Rev. Biomed. Eng*, 2002, 4, 261-86
3. Sia S. K. and Whitesides G. M., *Electrophoresis*, 2003, 24, 3563-3576
4. Metz S., Holzer R. and Renaud P., *Lab on a chip*, 2001, 1, 29-34
5. Christodoulides N., Tran M., Floriano P. N., Rodrigues M., Goodey A., Ali M., Neikirk D., and McDevitt J. T., *Analytical Chemistry*, 2002, 74,3030-3036
6. Goodey A., Lavigne J. J., Savoy S. M., Rodriguez M. D., Curey T., Tsao A., Simmons G., Wright J., Yoo S., Sohn Y, E. Anslyn V., J. Shear B., Neikirk D. P. and McDevitt J. T., *J. Am. Chem. Soc*., 2001, 123, 2559-2570
7. Qi S., Liu X., Ford S., Barrow J., Thomas G., Kelly K., McCandless A., Lian K., Goettert J. and Soper S. A., *Lab on a Chip*, 2002, 2, 88-95
8. Wang Y., Vaidya B., Farquar H. D., Stryjewski W., Hammer R. P., McCarley R. L., Soper S. A., Cheng Y. W. and Barany F., *Analytical Chemistry*, 2003, 75, 1130-1140
9. Ali M., Kirby R., Goodey A. P., Rodriguez M. D., Ellington A. D., Neikirk D. P. and McDevitt J. T., *Analytical Chemistry*, 2003, 75, 4732-4739

10. Bernard A., Michel B. and Delamarche E., *Analytical Chemistry*, 2001, 73,8-12

11. Marquette C. A. and Blum L. J., *Analytica Chimica Acta*, 2004, 506, 127-132

12. Culla M., Stokes D. L., Griffin G. D. and Dinh T. V., *Biosensors and Bioelectronics*, 2004, 19, 1007-1012

13. Hosokawa K., Sato K., Ichikawa N. and Maeda M., *Lab on a chip*, 2004, 4, 181-185

14. Noerholm M., Bruus H., Jakobsen M. H., Telleman P., and Ramsing N. B., *Lab on a chip,* 2004, 4, 28-37

15. Yang J., Liu Y., Rauch C. B., Stevens R. L., Liu R. H., Lenigk R. and Grodzinski P., *Lab on a chip*, 2002, 2, 179-187

16. Wolf M., Juncker D., Michel B., Hunziker P. and Delamarche E., *Biosensors and Bioelectronics*, 2004, 19, 1193-1202

17. Ko J. S., Yoon H. C., Yang H., Pyo H., Chung K. H., Kim S. J. and Kim Y. T., *Lab on a chip*, 2003, 3, 106-113

18. Keramas G., Perozziello G., Geschke O. and Christensen C. B. V., *Lab on a chip,* 2004, 4, 152-158

19. Yamamoto T., Nojima T. and Fujii T., *Lab on a chip*, 2002, 2, 197-202

20. Xu Z. R. and Fang Z. L., *Analytica Chimica Acta,* 2004, 507, 129-135

21. Li S. F. and Chen S. C., *IEEE Transactions on Advanced Packaging*, 2003, 26, 242-247.

22. Sato K., Tokeshi M., Kimura H., Odake T., Kimura H., Ooi T., Nakao M, and Kitamori T., *Analytical Chemistry*, 2000,72,1144-1147

23. Sato K., Tokeshi M., Kimura H. and Kitamori T., *Analytical Chemistry*, 2001, 73, 1213-1218

24. Verpoorte E., *Lab on a chip*, 2003, 3, 60N-68N

25. Chronis N., Liu G., Jeong K. and Lee L. P., *Optics Express*, 2003, 11, 2370-2378

26. Hosokawa K. and Maeda R., *Journal of Micromechanics and Microengineering*, 2000, 10, 415-420

Chapter 6: Summary and Conclusions

6.1. Current research summary

In this dissertation, several important microfluidic devices have been developed for biomedical and life sciences applications. Fundamental mechanical engineering issues such as thermal/fluid transport, materials and mechanics, and micromanufacturing have been investigated.

In Chapter 2, an analytical model for the analysis of a PZT actuator was developed based on an assumption of linear strain distribution along the PZT disk, the bonding layer, and the passive plate. Results from both FEM simulation and experiment data verified that this analytical model is valid. One important aspect of this analytical model is that it can predict the performance of the PZT actuator system with different design parameters and operation conditions, and therefore allow one to optimize the design. Finally, a system level analytical model for the PZT-actuated valveless micropump was developed to study its performance.

In Chapter 3, a novel continuous-flow PCR micro-chip for the rapid analysis of DNA was developed. Fabricated out of glass, this PCR microchip has variable channel widths, targeting regional velocity control to limit the transition time between temperature zones. Heat transfer analysis using a semi-analytical model and the finite element method was carried out for optimal thermal design. The μ-PIV measurement of the flow velocity confirmed that there is no flow separation and bubble formation inside the variable microchannel. The PCR chip has been tested as successful in amplifying 90 bp DNA sample.

Chapter 4 demonstrated that PDMS material can be used as interconnects for glass and plastic tubing in microfluidic applications. PDMS interconnect can be easily applied in different microfluidic systems made of glass, silicon, polymer and other MEMS materials such as SiO_2 and Si_xN_y thin films at a low cost using either UV curable epoxy or O_2 plasma activation. Leakage pressure, leakage rate, and pull-out force testing showed that PDMS interconnects have excellent performances. Key factors for strong bonding strength are the circularity of the hole punched in the PDMS and cleanness of the surfaces to be bonded. Moreover, PDMS interconnects are reusable and their fabrication is simple and cost-effective.

In Chapter 5, a single chamber chip and a four-chamber chip were developed for protein detection. Using soft lithography techniques, a fluidic network was fabricated into a top and a bottom PDMS layers. An inner silicon chip with an etched array of micro-cavities hosting agarose beads was sandwiched between the top and bottom layers of PDMS. Since PDMS is a soft material, the maximum assay flow rate was found to be 0.4 ml/min. Finite element method was employed to analyze the deformation of the PDMS chamber upon a holding pressure. The C-reactive protein (CRP) assay was used to characterize the single chamber and four-chamber chips. For the single chamber assay, the CRP detection limit could reach as low as 0.1ng/ml. The four-chamber PDMS chip was developed to solve problems of light source fluctuation and cross-reaction and to increase assay capacity. Using the back pressure compensation method, the performance of the four-chamber chip has been improved significantly. The signal variation among chambers was less than 10%.

6.2. Future research

I will continue my research in developing novel micro/nano-scale devices and systems for biological applications, in particular for single cell or molecular analysis. From mechanical engineering point of view, many opportunities lie in modeling and simulation of micro and nanoscale bio-fluid flow and bio-heat transfer. From these fundamental studies, novel micro/nano-fluidic devices could be developed upon the advancements in micro/nanofabrication techniques. An important aspect of future research could be the system-level integration for lab-on-a-chip. For example, one could integrate a flow-through PCR with a taste chip for continuous monitoring of biological environment.

Appendix A

Theoretical modeling of heat transfer inside a PCR device

First we denote w_p $(p = 1 \sim m)$, b_q, h_q $(q = 1 \sim 2)$ as width of the pth heater, qth layer thickness and interface position, respectively. The multilayer structure is shown in Fig. 1.

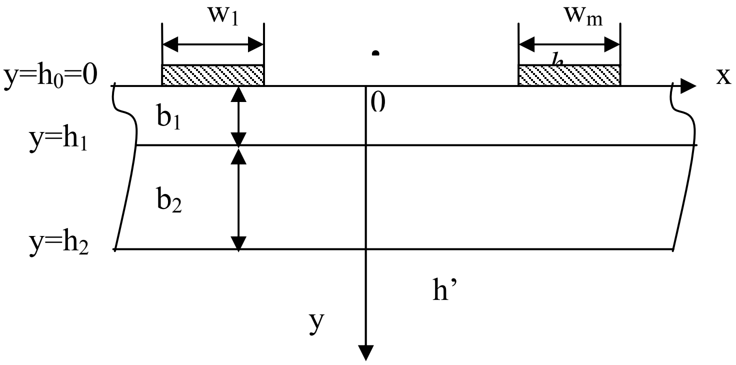

Figure A1. A schematic diagram of PCR chip for thermal modeling

To simplify, here we introduce a relative y-direction coordinate $y_q = y - h_{q-1}$ $(q = 1 \sim 2)$, i.e., the relative position within a corresponding layer. The steady-state heat conduction equation is

$$\frac{\partial^2 T_q}{\partial x^2} + \frac{\partial^2 T_q}{\partial {y_q}^2} = 0 \ (q = 1, 2) \tag{1}$$

in which subscript q corresponds to the qth layer starting from the top.

On the surface (y = 0) we have

$$-k_1 \frac{\partial T_1}{\partial y}\Big|_{y=0} = -h_t (T_1 - T_\infty) + \frac{Q_p}{w_p}$$ for the pth heater,

$$-k_1 \frac{\partial T_1}{\partial y}|_{y=0} = -h_t(T_1 - T_\infty) \text{ for other regions.} \qquad (2)$$

If we define a heat flux function $f(x) = \begin{cases} \frac{Q_p}{w_p} \text{ (for the pth heater)} \\ 0 \text{ (for other regions)} \end{cases}$, Equation 2 can be rewritten as

$$-k_1 \frac{\partial T_1}{\partial y}|_{y=0} = -h_t(T_1 - T_\infty) + f(x) \qquad (3)$$

where Q is the input power per unit length, w is the width of the strip heater, h_t is the convective heat transfer coefficient (we ignore the variation of h_t on the surface due to its small area.

Assumed no contact thermal resistance at the interface, the heat flux and the temperature at the interface are continuous. Then Eq. (4) turns into

$$k_1 \frac{\partial T_1}{\partial y}|_{y=h_1} = k_2 \frac{\partial T_2}{\partial y}|_{y=h_1}, T_1|_{y=h_1} = T_2|_{y=h_2} \qquad (q = 1, 2) \qquad (4)$$

At the bottom of the PCR microchip, we have

$$-k_2 \frac{\partial T_2}{\partial y}|_{y=h_2} = h_t'(T_2 - T_\infty) \qquad (5)$$

Denote Fourier transform with respect to x as $E_q(\lambda, y_q) = \int_{-\infty}^{+\infty} [T_q(x,y) - T_\infty] e^{-i\lambda x} dx$, $F(\lambda) = \int_{-\infty}^{+\infty} f(x) e^{-i\lambda x} dx$, where $x_{p,2}$ and $x_{p,1}$ are the left and right boundaries of the *pth* heater. The above equations change into

$$-\lambda^2 E_q + \frac{\partial^2 E_q}{\partial y_q^{\,2}} = 0 \qquad (6)$$

$$-k_1 \frac{\partial E_1}{\partial y}|_{y=0} = F(\lambda) - h_t E_1 \tag{7}$$

$$k_1 \frac{\partial E_1}{\partial y}|_{y=h_1} = k_2 \frac{\partial E_2}{\partial y}|_{y=h_2} \tag{8}$$

$$-k_2 \frac{\partial E_2}{\partial y}|_{y=h_2} = h_t' E_2 \tag{9}$$

A general solution of Eq. (6) is

$$E_q(\lambda, y_1) = A_q \sinh(\lambda y_q) + B_q \cosh(\lambda y_q) \tag{10}$$

From (9) we get.

$$-k_2\lambda[A_2 \cosh(\lambda b_2) + B_2 \sinh(\lambda b_2)] = h_t'[A_2 \sinh(\lambda b_2) + B_2 \cosh(\lambda b_2)]$$

or

$$\frac{B_2}{A_2} = -\frac{h_t' \sinh(\lambda b_2) + k_2\lambda \cosh(\lambda b_2)}{h_t' \cosh(\lambda b_2) + k_2\lambda \sinh(\lambda b_2)} = -\frac{h_t' \tanh(\lambda b_2) + k_2\lambda}{h_t' + k_2\lambda \tanh(\lambda b_2)} \tag{11}$$

Substituting $E_1(\lambda, y_1) = A_1 \sinh \lambda y_1 + B_1 \cosh \lambda y_1$ into Eq. (7) yields

$$-k_1\lambda A_1 = -h_t B_1 + F(\lambda) \tag{12}$$

Define a function $\zeta_q(\lambda) = \frac{B_q}{A_q}$. We have $\zeta_2(\lambda) = \frac{B_2}{A_2} = -\frac{h_t' \tanh(\lambda b_2) + k_2\lambda}{h_t' + k_2\lambda \tanh(\lambda b_2)}$

Eq. (8) leads to

$$\zeta_1(\lambda) = \frac{B_1}{A_1} = \frac{1 - \frac{k_2}{k_1}\frac{\tanh(\lambda b_1)}{\zeta_2}}{\frac{1}{\zeta_2}\frac{k_2}{k_1} - \tanh(\lambda b_1)} \tag{13}$$

It should be pointed out that $\zeta_q(\lambda)$ is always an odd function of λ. Notice in Eq. (12)

$$-k_1\lambda A_1 = -h_t A_1 \zeta_1 + F(\lambda) \tag{14}$$

$$A_1 = \frac{F(\lambda)}{-k_1\lambda + h_t\zeta_1} \tag{15}$$

$$B_1 = \zeta_1 A_1 = \frac{F(\lambda)}{-k_1\lambda + h_t\zeta_1}\zeta_1 \tag{16}$$

Thus

$$\begin{aligned} E_1(\lambda, y_1) &= A_1 \sinh(\lambda y_1) + B_1 \cosh(\lambda y_1) \\ &= \frac{F(\lambda)}{h_t\zeta_1 - k_1\lambda}[\sinh(\lambda y_1) + \zeta_1 \cosh(\lambda y_1)] \end{aligned} \tag{17}$$

We finally find

$$T_1(x, y_1) - T_\infty = \frac{1}{2\pi}\int_{-\infty}^{+\infty} \frac{F(\lambda)}{h_t\zeta_1 - k_1\lambda}[\sinh(\lambda y_1) + \zeta_1 \cosh(\lambda y_1)]e^{i\lambda x} d\lambda \tag{18}$$

Noticing in Eq. (19) $\frac{\sinh(\lambda y_1) + \zeta_1 \cosh(\lambda y_1)}{h_t\zeta_1 - k_1\lambda}$ is an even function of λ (note ζ_1 is odd function of λ, see Eq. 13), we can simplify Eq. (18) as

$$T_1(x, y_1) - T_\infty = \frac{1}{\pi}\int_0^{+\infty} \frac{\sinh(\lambda y_1) + \zeta_1 \cosh(\lambda y_1)}{h_t\zeta_1 - k_1\lambda} \mathrm{Re}[F(\lambda)e^{i\lambda x}] d\lambda \tag{19}$$

in which $F(\lambda) = \sum_{p=1}^{m} \frac{Q_p}{w_p} \frac{\exp(-i\lambda x_{p,2}) - \exp(-i\lambda x_{p,1})}{-i\lambda}$ for heaters with constant heat flux and $\lim_{\lambda \to 0} F(\lambda) = \sum_{p=1}^{m} Q_p$

Here the channel is regarded as the top of the second layer, Eq. (8) gives

$$B_2 - \frac{F(\lambda)}{h_t\zeta_1 - k_1\lambda}[\sinh(\lambda b_1) + \zeta_1 \cosh(\lambda b_1)] = 0 \tag{20}$$

Rearranging Eq. (20) generates

$$E_2(\lambda, y_2 = 0) = B_2 = \frac{F(\lambda)}{h_t\zeta_1 - k_1\lambda}[\zeta_1 \cosh(\lambda b_1) + \sinh(\lambda b_1)] \tag{21}$$

Thus

$$
\begin{aligned}
&T_2(x, y_2 = 0) - T_\infty \\
&= \frac{1}{2\pi}\int_{-\infty}^{+\infty} \frac{F(\lambda)}{h_t\,\zeta_1 - k_1\lambda}[\sinh(\lambda b_1) + \zeta_1 \cosh(\lambda b_1)]e^{i\lambda x}d\lambda \\
&= \frac{1}{\pi}\int_{0}^{+\infty} \frac{1}{h_t\zeta_1 - k_1\lambda}[\sinh(\lambda b_1) + \zeta_1 \cosh(\lambda b_1)]\operatorname{Re}[F(\lambda)e^{i\lambda x}]d\lambda
\end{aligned}
\qquad (22)
$$

Appendix B

Nomenclature

Chapter 2

t	time
h	location of the neutral surface
h_p	thickness of passive plate
h_b	thickness of the bonding layer
h_{pzt}	thickness of the PZT disk
h'	thickness difference of the passive plate and the neutral surface
h''	thickness of PZT disk and the bonding layer
E	Young’s Modulus
E'	Young’s Modulus of PZT disk and bonding layer two-layer structure
E_c	Young’s Modulus of three-layer structure
E_b	Young’s Modulus of the bonding layer
E_b'	Young’s Modulus of other bonding layers
E_{pzt}	Young’s Modulus of PZT disk
E_p	Young’s Modulus of the passive plate
$E_{p'}$	Young’s Modulus of other passive plates
γ	Poisson ratio
γ_p	Poisson ratio of the passive plate

γ_b	Poisson ratio of the bonding layer
γ_{pzt}	Poisson ratio of the PZT disk
γ_c	Poisson ratio of the three-layer structure
σ	stress
σ_p	stress in the passive plate
σ_b	stress in the bonding layer
σ_{pzt}	stress in the PZT disk
σ_i	stress in the interface layer
ε	strain
ε_p	strain in the passive plate
ε_b	strain in the bonding layer
ε_{pzt}	strain in the PZT disk
z	coordinate in the vertical direction
K	boundary parameter
d_{31}	electrical-mechanical coupling coefficient in the z direction
U	working voltage
α	mechanical properties ratio of the bonding layer and the passive plate
β	mechanical properties ratio of the PZT disk and the passive plate
η	mechanical parameter of the PZT disk
C_1	thickness ratio of the PZT disk
C_2	thickness ratio of the bonding layer

C_1'	thickness ratio of the passive plate
C_2'	thickness ratio of the PZT disk-bonding layer two-layer structure
M_1	moment produced by the PZT disk
M_2	moment produced by the fix boundary
M_{11}	moment produced by moment balance of the fix boundary
a	radius of the passive plate
b	radius of the PZT disk
r	radius of the membrane displacement
W_1	displacement of the passive plate
W_2	displacement of the PZT disk
D_c	flexural modulus for the three-layer structure
D_p	flexural modulus for the passive plate
e	piezoelectricity
ε'	permittivity
S'	compliance
$U_{0\text{-}p}$	zero-pink working voltage
$h_{b\text{-}p}$	thickness ratio of the bonding layer and the passive plate
$h_{pzt\text{-}p}$	thickness ratio of the PZT disk and the passive plate
$R_{pzt\text{-}p}$	radius ratio of the PZT disk and the passive plate
ΔP	pressure loss
K_1	pressure loss coefficient
ρ	density

u	velocity
ζ	pressure loss coefficient
$\zeta_{negative}$	pressure loss coefficient in the negative direction
$\zeta_{positive}$	pressure loss coefficient in the positive direction
A	area
A_{neck}	nozzle /diffuser neck area
$A_{upstream}$	nozzle/diffuser up stream area
A_{in}	inlet section area
A_{out}	outlet section area
Cp	pressure recovery coefficient
n	normal unit vector
V	volume
V_{gas}	gas volume
V_{liquid}	liquid volume
$V_{chamber}$	chamber volume
P	pressure
P_0	atmosphere pressure
P_{out}	outlet pressure
P_{in}	inlet pressure
ϕ	volume flow rate
ϕ_{in}	inlet volume flow rate
ϕ_{out}	outlet volume flow rate

g	acceleration of gravity
z_{in}	inlet potential
z_{out}	outlet potential
ξ	flow resistance
Ψ	kinetic energy coefficient
Ψ_{in}	inlet kinetic energy coefficient
Ψ_{out}	outlet kinetic energy coefficient
$\overline{U}$	average velocity

Chapter 3

c	space between 95°C heater and 75°C
d	space between 75°C heater and 95°C
b_q	thickness of the *q*th layer
b_1	thickness of the first layer
b_2	thickness of the second layer
p	number of heaters
T	temperature
T_q	temperature in the *q*th layer
T_1	temperature in the first layer
T_2	temperature in the second layer
T_∞	atmosphere temperature
x	coordinate

y	coordinate
y_q	relative coordinate
k	thermal conductivity
k_1	thermal conductivity of the first layer
k_2	thermal conductivity of the second layer
Q	heat flux
$Q_{p,m}$	heat flux of the element heater
w	width of the heater
h_t	heat transfer coefficient at the top surface
h_t'	heat transfer coefficient at the bottom surface
$f(x)$	heat flux function
$F(x)$	Fourier transform of heat flux function
h_{eff}	equivalent heat transfer coefficient
λ	Fourier transform variable
i	imaginary variable
m	number of element heaters divided by each heater
ζ_1	parameter ratio

Bibliography

Chapter 1

1. Manz A., Graber N. and Widmer H.M., 1990, *Sensors and Actuators B*, 1, 244-248
2. Ko J. S., et al, 2003, *Lab On a Chip*, 3, 106-113
3. Gau J., Lan E. H., Dunn R., Ho C. M., Woo J. C., *Biosensors and Bioelectronics*, 16, 745-755
4. Wang J., 2004, *Analytica Chimica Acta*, 506, 3-10
5. Yao G. and Tan W. H., 2004, *Analytical Biochemistry*, in press
6. Call D. R., Borucki M. K. and Loge F. J., 2003, *Journal of Microbiological Methods*, 53, 235-243
7. Wiese R., Belosludetsev Y., Powdrill T., Thompson P. and Hogan M., 2001, *Clinical Chemistry*, 47, 1451-1457
8. Tan W. and Desai T. A., 2003, *Biomedical Microdevices*, 5, 235-244
9. Leclerc E., Sakai T. and Fujii T., 2003, *Biomedical Microdevices*, 5, 109-114
10. Makamba H., Kim J. H., Lim K., Park N. and Hahn J. H., 2003, *Electrophoresis*, 24, 3607-3619.
11. Polla D. L., Erdman A. G., Robbins W. P., Markus D. T., Diaz J., Rizq R., Y., Nam H. Brickner T., 2000, *Annu. Rev. Biomed. Eng*, 551-576
12. Razzacki S. Z., Thwar P. K., Yang M., Ugaz V. M. and Burns M. A., 2004, *Advanced Drug Delivery Reviews*, 56, 185-198

13. Shawgo R. S., Grayson A. C. R., Li Y. W. and Cima M. J., 2002, *Current Opinion in Solid State and Materials Science,* 6, 329-334
14. Ng M. K., Gitlin I., Strook A. D. and Whitesides G. M., 2002, *Electrophoresis*, 23, 3461-3473
15. Sia S. K. and Whitesides G. M., *Electrophoresis*, 2003, 24, 3563-3576
16. Unger M. A., Chou H. P., Thorsen T., Scherer A. and Quake S. R., 2000, *Science*, 113-116.
17. Whitesides G.M., Ostuni E., Takayama S., Jiang X., and Ingber D., *Annu. Rev. Biomed. Eng*, 2001, 3, 335-73
18. Damean N., Regtien P. P. L. and Elwenspoek M., 2003, *Sensors and Actuators A*, 105, 137-149.
19. Erickson D., Li D.Q. and Krull U. J., 2003, *Analytical Biochemistry*, 317, 186-200
20. Xia Y. N. and Whitesides G. M., 1998, *Annu. Rev. Mater. Sci.* 28, 153-184

Chapter 2

1. Chee C.Y.K., Tong L., Steven G.P., 1998, *Journal of Intelligent Material Systems and Structure,* 9, 3-19.
2. Crawley E.F., Anderson E.H., 1990, *Journal of Intelligent Material Systems and Structure*, 1, 4-25.
3. Kim S. J., Jones J.D., 1991, *AIAA. J,* 29, 2047-53.
4. Ray M.C., Bhattacharya R., Samanta B., 1993, *AIAA J.*, 31, 1684-91.
5. Chaudhry Z., Rogers C. A., 1994, *AIAA J.,* 32, 1289-94.

6. Yanagisawa T., Nakagawa Y., 1993, *Trans. Inst. Electron. Informat. Commum. Eng. A,* 76, 1261-9.
7. Dobrucki A. B., Pruchnicki P., 1997, *Sensors and Actuators A,* 58, 203-12.
8. Tzou H.S., 1994, Kluwer Publishing Company.
9. Larson P.H., 1994, PhD Thesis, University of Delaware.
10. Stemme E., Stemme G., 1993, *Sensors and Actuators A,* 39, 159-167.
11. DeVoe D. L., Pisano A. P., 1997, *Journal of Microelectromehcanical Systems*,6, 266-270.
12. DeVoe D. L., Pisano A. P., 2001, *Journal of Microelectromehcanical Systems*, 10, 180-186.
13. Yoon H. S., Washington G., 1998, *Smart Materials and Structures*, 7, 537-542.
14. Morris C. J., Forster F. K., 2000, *Journal of Micromechanics & Microengineering,* 10, 459-465.
15. Cao L., Mantell S., Polla D., 2001, *Sensors and Actuators A*, 94, 1-9.
16. Li S. F., Liu Y., Chen S. C., 2001*, Proceedings of SPIE*, 4560, 67-74.
17. Gerlach T., Wurmus H., 1995, *Sensors and Actuators A*, 50, 135-140.
18. Olsson A., Stemme G., Stemme E., 1995*, Sensors and Actuators A,* 46-47, 549-556.
19. Forster E. K., Bardell R. L, Abramowitz M. A., Sharma N. R., Blanchard A., 1995, *Proceedings of IMECE*, ASME.
20. Christensen R. M., 1979, John Wiley & Sons, Inc.
21. Timoshenko S., Woinowsky-Krieger S., 1995, Second Edition McGraw-Hill.

22. Stemme E., Stemme G., 1993, *Sensors and Actuators A*, 39, 159-167
23. Zengerle R. and Richter M., 1994, *Journal of Micromechanics and Microengineering,* 4, 192-204.
24. Olsson A., Stemme G. and Stemme E., 1999, *Journal of Micromechanics and Microengineering,* 9, 34-44.
25. Gerlach T., 1997, *Transducer'97*, Chicago, 1035-1038.
26. Olsson A., Stemme G. and Stemme E., 2000, *Sensors and Actuators A,* 84, 65-175.
27. Gerlach T., Wurmus H., 1995, *Sensors and Actuators A,* 50, 135-140.
28. Olsson A., Stemme G. and Stemme E., 1997, *Transducer'97* Chicago, 1039-1042.
29. Nguyen N. T. and White R. M., 1999, *Sensors and Actuators A,* 77, 229-236.
30. Gong Q. L., Zhou Z.Y., Yang Y. H. and Wang X. H., 2000, *Sensors and Actuators A,* 83, 200-207
31. Pan L. S., Ng T. Y, Liu G. R., Lam K. Y. and Jiang T. Y., 2001, *Sensors and Actuators A,* 3052, 1-9
32. Morris C. J. and Forster F. K., 2000, *Journal of Micromechanics and Microengineering,* 10, 459-465
33. Bardell R. L., Sharma N. R., Forster F. K., Afroowitz M. A. and Penney R. J., 1997, *Proceedings of MEMS ASME*, 47-53
34. Olsson A., Enoksson P., Stemme G. and Stemme E., 1997, *Journal of Microelectromechanical systems,* 6

Chapter 3

1. Mullis K. B., Ferre F., Gibbs R. A., 1994, *The Polymerase Chain Reaction*, Birkauser, Boston
2. Wittwer C. T., Ririe K. M., Andrew R. V., David D. A., Gundry R. A., and Balis U. J., 1997, Biotechniques, 22, 176-181
3. http://www.idahotec.com/
4. Lin Y. C., Huang M. Y., Young K. C., Chang T. T., and Wu C.Y., 2000, *Sensors and Actuators B*, 71, 2-8
5. Hong J. W., Fujii T., Seki M., Yamamoto T., and Endo I., 2001, *Electrophoresis*, 22, 328-333
6. Lagally E. T., Emrich C. A., and Mathies R. A., 2001, *Lab on a chip*, 1, 102-107
7. Shin Y. S., Cho K. C., Lim S. H., Chung S., Park S. J., Chung C., Han D. C., and Chang J. K., 2003, *Journal of Micromechanics and Microengineering*, 13, 768-774
8. Sun K., Yamaguchi A., Ishida Y., Matsuo S. and Misawa H., 2002, *Sensors and Actuators B,* 1-7
9. Schneegab I., and Kohler J. M., 2001, *Reviews in Molecular Biotechnology*, 82, 101-121
10. Schneegab I., Brautigam R., and Kohler J. M., 2001, *Lab on a chip*, 1, 42-49

11. Chou C. F., Changrani R., Roberts P., Sadler D., Burdon J., Zenhausern F., Lin S., Mulholland A., Swami N., and Terbrueggen R., *Microelectronic Engineering*, 2002, 61-62, 921-925
12. Liu J., Enzelberger M., and Quake S., 2002, *Electrophoresis*, 1531-1536
13. Kopp M. U., Mello A. J. de, and Manz A.,, 1998, Science, 280, 1046-1048
14. Obeid P. J., Chirstopoulos T. K., Cratree H. J., and Backhouse C. J., 2003, *Analytical Chemistry*, 75,288-295
15. Yong D. S., Lee Y. S., Cho H. J., Sung S. W., Oh K. W., Cha J. H., and Lim G. B., 2002, *Journal of Micromechanics and Microengineering*, 12, 813-823
16. Obeid P. J., Chirstopoulos T. K., 2003, Analytica Chimica Acta, Vol.494 pp.1-9
17. Simpson P.C., Wooley A. T., Mathies R. A., 1998, *Biomedical Microdevices*, Vol.1, pp.7-26
18. Hao Q., 2004, *Journal of Micromechanics and Microengineering,* Vol. 14, pp.914-926
19. Li H., et al, 2004, *Journal of Microelectromechanical Systems*, in press
20. Meihart, C. D. Wereley S. T., and Santiago J. G., 1999, *Experiments in Fluids*, 27, 414-419
21. Panton R., 2003, *Incompressible Flow*, John Willey & Sons, Inc

Chapter 4

1. Gonzalez C., Collins S. D. and Smith R. L., 1998, *Sensors and Actuators B*, 49, 40-45.

2. Yao T.J., Lee S.W., Fang W.L. and Tai Y.C., 2000, *Proceedings of IEEE MEMS 2000 Conference*, 624-627.
3. Wijingaart W., Andersson H., Enoksson P., Noren K. and Stemme G., 2000, *Proceedings of IEEE MEMS 2000 Conference*, 674-679.
4. Armani D., Liu C. and Aluru N., 1999, *Proceedings of IEEE MEMS 1999 Conference*, 222-227.
5. Puntambekar A. and Ahn C. H., 2002, *Journal of Micromechanics and Microengineering*, 12, 35-40.
6. Gray B.L., Jaeggi D., Mourlas N.J., Van Drieenhuizen B.P., Williams K.R., Maluf N.I. and Kovacs G.T.A., 1999, *Sensors and Actuators A*, 77, 57-65.
7. Tsai J.H and Lin L.W., 2002, *Journal of Micromechanics and Microengineering,* 11, 577-581.
8. Pattekar A.V. and Kothare M.V., 2003, *Journal of Micromechanics and Microengineering*, 13, 337-345.
9. Xia Y.N., and Whitesides G.M., 1998, *Annu. Rev. Mater. Sci.*, 28, 154-184.
10. Jo B.H., Lerberghe L.M., Motsegood K.M. and Beebe D.J., 2000, *Journal of Microelectromechanics Systems*, 9, no.1, 76-81.
11. Unger M.A., Chou H.P., Thorsen T., Scherer A. and Quake S. R., 2000, *Science*, 288, 113-116.
12. Yang X., Grosjean C. and Tai Y.C., 1999, *Journal of Microelectromechanical Systems*, 8, 393 - 402.

Chapter 5

1. Whitesides G.M., Ostuni E., Takayama S., Jiang X., and Ingber D., *Annu. Rev. Biomed. Eng*, 2001, 3, 335-73
2. Beebe D., Mensing G. A. and Walker G. M., *Annu. Rev. Biomed. Eng*, 2002, 4, 261-86
3. Sia S. K. and Whitesides G. M., *Electrophoresis*, 2003, 24, 3563-3576
4. Metz S., Holzer R. and Renaud P., *Lab on a chip*, 2001, 1, 29-34
5. Christodoulides N., Tran M., Floriano P. N., Rodrigues M., Goodey A., Ali M., Neikirk D., and McDevitt J. T., *Analytical Chemistry*, 2002, 74,3030-3036
6. Goodey A., Lavigne J. J., Savoy S. M., Rodriguez M. D., Curey T., Tsao A., Simmons G., Wright J., Yoo S., Sohn Y, E. Anslyn V., J. Shear B., Neikirk D. P. and McDevitt J. T., *J. Am. Chem. Soc.*, 2001, 123, 2559-2570
7. Qi S., Liu X., Ford S., Barrow J., Thomas G., Kelly K., McCandless A., Lian K., Goettert J. and Soper S. A., *Lab on a Chip*, 2002, 2, 88-95
8. Wang Y., Vaidya B., Farquar H. D., Stryjewski W., Hammer R. P., McCarley R. L., Soper S. A., Cheng Y. W. and Barany F., *Analytical Chemistry*, 2003, 75, 1130-1140
9. Ali M., Kirby R., Goodey A. P., Rodriguez M. D., Ellington A. D., Neikirk D. P. and McDevitt J. T., *Analytical Chemistry*, 2003, 75, 4732-4739
10. Bernard A., Michel B. and Delamarche E., *Analytical Chemistry*, 2001, 73,8-12
11. Marquette C. A. and Blum L. J., *Analytica Chimica Acta*, 2004, 506, 127-132

12. Culla M., Stokes D. L., Griffin G. D. and Dinh T. V., *Biosensors and Bioelectronics*, 2004, 19, 1007-1012
13. Hosokawa K., Sato K., Ichikawa N. and Maeda M., *Lab on a chip*, 2004, 4, 181-185
14. Noerholm M., Bruus H., Jakobsen M. H., Telleman P., and Ramsing N. B., *Lab on a chip,* 2004, 4, 28-37
15. Yang J., Liu Y., Rauch C. B., Stevens R. L., Liu R. H., Lenigk R. and Grodzinski P., *Lab on a chip*, 2002, 2, 179-187
16. Wolf M., Juncker D., Michel B., Hunziker P. and Delamarche E., *Biosensors and Bioelectronics*, 2004, 19, 1193-1202
17. Ko J. S., Yoon H. C., Yang H., Pyo H., Chung K. H., Kim S. J. and Kim Y. T., *Lab on a chip*, 2003, 3, 106-113
18. Keramas G., Perozziello G., Geschke O. and Christensen C. B. V., *Lab on a chip,* 2004, 4, 152-158
19. Yamamoto T., Nojima T. and Fujii T., *Lab on a chip*, 2002, 2, 197-202
20. Xu Z. R. and Fang Z. L., *Analytica Chimica Acta,* 2004, 507, 129-135
21. Li S. F. and Chen S. C., *IEEE Transactions on Advanced Packaging*, 2003, 26, 242-247.
22. Sato K., Tokeshi M., Kimura H., Odake T., Kimura H., Ooi T., Nakao M, and Kitamori T., *Analytical Chemistry*, 2000,72,1144-1147
23. Sato K., Tokeshi M., Kimura H. and Kitamori T., *Analytical Chemistry*, 2001, 73, 1213-1218

24. Verpoorte E., *Lab on a chip*, 2003, 3, 60N-68N
25. Chronis N., Liu G., Jeong K. and Lee L. P., *Optics Express*, 2003, 11, 2370-2378
26. Hosokawa K. and Maeda R., *Journal of Micromechanics and Microengineering*, 2000, 10, 415-420

VITA

Shifeng Li was born on February 5th, 1972 in HuBei, China, the first son of Houming Li and Gelian Cheng. He attended Shanghai Jiaotong Univeristy and earned B.E. and M.E. degree in Mechanical Engineering in 1994 and 1999 respectively.

Since 2000, Shifeng Li has pursued a PhD. Degree in Dr. Shaochen Chen group in Mechanical Engineering at UT. His research has focus on microfluidic devices for biological applications.

Permanent address: Room 201 Building 3 Meiling
AnLu City, HuBei, China, 456700

This dissertation was typed by the author